# Plasmonic waveguides self-assembled on DNA origami templates: from synthesis to near-field characterizations

## DISSERTATION

zur Erlangung des akademischen Grades
Doctor rerum naturalium
(Dr. rer. nat.)

Vorgelegt
der Fakultät Mathematik und Naturwissenschaften
der Technischen Universität Dresden

von

**M.Sc. Fatih Nadi Gür**
geboren am 20.03.1987 in Karaman, Türkei

|  |  |
|---|---|
| **Eingereicht am:** | 15. Dezember 2017 |
| **Tag der Verteidigung:** | 26. März 2018 |
| **Gutachter:** | Prof. Dr. rer. nat. et Ing. habil. Michael Mertig |
|  | Prof. Dr. phil. II habil. Lukas Matthias Eng |

Die Dissertation wurde in der Zeit von Januar 2014 bis Dezember 2017 im
cfaed - Center for Advancing Electronics Dresden, TU Dresden angefertigt.

*Dedicated to all the children who could never grow up…*

*“Yesterday I was clever, so I wanted to change the world. Today I am wise, so I am changing myself.” – Rumi*

# ABSTRACT

Manipulating light by controlling surface plasmons on metals is being discussed as a means for bridging the size gap between micrometer-sized photonic circuits and nanometer-sized integrated electronics. Plasmonic waveguides based on metal nanoparticles are of particular interest for circumventing the diffraction limit, thereby enabling high-speed communication over short-range distances in miniaturized micro-components. However, scalable, inexpensive fine-tuning of particle assemblies remains a challenge and near-field probing is required to reveal plasmonic interactions. In this thesis, self-assembled waveguides should be produced on DNA scaffolds. DNA origami is an extremely versatile and robust self-assembly method which allows scalable production of nanostructures with a fine control of assemblies at the nanoscale. To form the plasmonic waveguides, six-helix bundle DNA origami nanotubes are used as templates for attachment of highly monodisperse and monocrystalline gold nanoparticles with an inter-particle distance of 1-2 nm. In the first part of this thesis, the effects of parameters which are involved in assembly reactions are systematically investigated. The assembly yield and binding occupancy of the gold nanoparticles are determined by an automated, high-throughput image analysis of electron micrographs of the formed complexes. As a result, unprecedented binding site occupancy and assembly yield are achieved with the optimized synthesis protocol. In addition, waveguides with different sizes of gold nanoparticles and different inter-particle distances, quantum dots attachments to the waveguides and multimerization of the waveguides are successfully realized. In the second part of this thesis, direct observation of energy transport through a self-assembled waveguide towards a fluorescent nanodiamond is demonstrated. High-resolution, near-field mapping of the waveguides are studied by electron energy loss spectroscopy and cathodoluminescence imaging spectroscopy. The experimental and simulation results reveal that energy propagation through the waveguides is enabled by coupled surface plasmon modes. These surface plasmon modes are probed at high spatial and spectral resolutions. The scalable self-assembly approach presented here will enable the construction of complex, sub-diffraction plasmonic devices for applications in high-speed optical data transmission, quantum information technology, and sensing.

# ZUSAMMENFASSUNG

Die Manipulation des Lichts durch die Kontrolle von Oberflächenplasmonen auf metallischen Oberflächen und Nanopartikeln gilt als vielversprechende Methode zur Überbrückung der Größen-Lücke zwischen Mikrometer-großen photonischen und nanometer-großen elektronischen Schaltkreisen. Plasmonische Wellenleiter basierend auf metallischen Nanopartikeln sind vom besonderen Interesse, da sie die Umgehung des Beugungslimits und somit eine Hochgeschwindigkeitskommunikation über kurze Distanzen in immer kleiner werdenden Schaltkreisen ermöglichen könnten. Allerdings ist die skalierbare und kostengünstige Anordnung von Partikeln eine große Herausforderung und es werden Nahfelduntersuchungen benötigt um plasmonische Interaktionen detektieren zu können. Das Ziel dieser Arbeit ist die Selbstassemblierung von multi-partikel Wellenleitern auf DNA Gerüsten. Die Verwendung von DNA-Origami bietet eine äußerst vielseitige Plattform zur skalierbaren Herstellung von Nanostrukturen mittels Selbstassemblierung und ermöglicht eine präzise Kontrolle der Anordnungen im Nanobereich. Für den Aufbau der plasmonischen Wellenleiter werden DNA-Origami Nanoröhren, bestehend aus sechs Helices als Templat für die Anbindung von monodispersen und monokristallinen Goldnanopartikeln mit einem interpartikulären Abstand von 1-2 nm verwendet. Im ersten Abschnitt dieser Arbeit werden die beeinflussenden Faktoren dieser Assemblierungsreaktion systematisch untersucht. Die Ausbeute der assemblierten Strukturen und die Besetzung der Bindungsstellen werden durch eine automatisierte und effiziente Bildanalyse von Elektronenmikroskopieaufnahmen ausgewertet. Durch die Entwicklung eines optimierten Syntheseprotokolls werden bisher unerreichte Assemblierungsausbeuten ermöglicht. Zusätzlich erfolgen die experimentelle Realisierung von Strukturen mit verschieden großen Goldnanopartikeln und unterschiedlichen interpartikulären Abständen, sowie die Anbindung von Quantenpunkten an die Wellenleiter und eine Verknüpfung der assemblierten Strukturen. Der zweite Abschnitt dieser Dissertation befasst sich mit der Untersuchung des Energietransports in selbstassemblierten Wellenleitern über einen fluoreszierenden Nanodiamanten. Dazu erfolgen hochaufgelöste Nahfeldmessungen der Wellenleiter mittels Elektronenenergieverlustspektroskopie und Kathodolumineszenz-mikroskopie. Die experimentellen Ergebnisse und zusätzlich durchgeführte Simulationen bestätigen eine durch gekoppelte Oberflächenplasmonenmoden induzierte Weitergabe der Energie innerhalb des Wellenleiters. Diese Oberflächenplasmonenmoden werden bei hoher räumlicher und spektraler Auflösung untersucht. Das hier umgesetzte Konzept der Selbstassemblierung wird den Aufbau komplexer plasmonischer Geräte für Anwendungen im Bereich der optischen Hochgeschwindigkeitsdatenübertragung, der Quanteninformationstechnolgie und der Sensorik ermöglichen.

# CONTENTS

# LIST OF PUBLICATIONS

[A] Gür, F. N.; McPolin, C. P. T.; Raza, S.; Mayer, M.; Roth, D. J.; Steiner, A. M.; Löffler, M.; Fery, A.; Brongersma, M. L.; Zayats, A. V.; König, T. A. F.; Schmidt, T. L. Self-assembled plasmonic waveguides for excitation of fluorescent nanodiamonds. *arXiv*.1712.09141.**2017**

[B] Gonçalves, D. P. N.; Rodriguez, R. D.; Kurth, T.; Bray, L. J.; Binner, M.; Jungnickel, C.; Gür, F. N.; Poser, S. W.; Schmidt, T. L.; Zahn, D. R. T.; Androutsellis-Theotokis, A.; Schlierf, M.; Werner, C. Enhanced Targeting of Invasive Glioblastoma Cells by Peptide-Functionalized Gold Nanorods in Hydrogel-Based 3D Cultures. *Acta Biomater.* **2017**, 58, 12–25.

[C] Agarwal, N. P.; Matthies, M.; Gür, F. N.; Osada, K.; Schmidt, T. L. Block Copolymer Micellization as a Protection Strategy for DNA Origami. *Angew. Chem. Int. Ed.* **2017**, 56, 5460–5464.

[D] Gür, F. N.; Schwarz, F. W.; Ye, J.; Diez, S.; Schmidt, T. L. Toward Self-Assembled Plasmonic Devices: High-Yield Arrangement of Gold Nanoparticles on DNA Origami Templates. *ACS Nano* **2016**, 10, 5374–5382.

[E] Lin, W.; Reddavide, F. V.; Uzunova, V.; Gür, F. N.; Zhang, Y. Characterization of DNA-Conjugated Compounds Using a Regenerable Chip. *Anal. Chem*. **2015**, 87, 864–868. (From Master study)

**Patents:**

[1] Wiener, E.; Gür, F. N.; Kurth, T.; Ader, M.; Schmidt, T. L. Verfahren und Mittel zur parallelen Detektion einer Vielzahl von Antigenen in der Elektronenmikroskopie. Patent filed, Germany.

All papers have been published during my PhD study. The results of papers A and D are discussed in detail in this dissertation.

# LIST OF FIGURES

# LIST OF ABBREVIATIONS AND ACRONYMS

| | |
|---|---|
| µ | Micro (x$10^{-6}$) |
| 1D, 2D, 3D | One-, two-, three-dimensional |
| 6-HB | Six-helix bundle |
| a.u. | Arbitrary unit |
| AFM | Atomic force microscopy |
| Au | Gold |
| AuNP | Gold nanoparticle |
| BEM | Boundary element method |
| bp | Base pair |
| BS | Binding site |
| BSA | Bovine serum albumin |
| BSPP | Bis(p-sulfonatophenyl) phenylphosphine dihydrate dipotassium salt |
| CCD | Charge-coupled devices |
| CL | Cathodoluminescence |
| CTAB | Hexadecyltrimethylammonium bromide |
| CTAC | Hexadecyltrimethylammonium chloride |
| Da | Dalton |
| DNA | Deoxyribonucleic acid |
| ds | Double-stranded |
| EDTA | Ethylenediaminetetraacetic acid |
| EELS | Electron energy loss spectroscopy |
| EFTEM | Energy filtered transmission electron microscopy |
| FDTD | Finite-difference time-domain |
| FND | Fluorescent nanodiamond |
| HQ | Hydroquinone |
| IR | Infrared |
| k | Kilo (x$10^{3}$) |
| L | Liter |
| L | Longitudinal |

| | |
|---|---|
| LSP | Localized surface plasmon |
| M | Mega (x$10^6$) |
| M | Molar |
| min | Minute |
| nm | Nanometer ($10x^{-9}$ meter) |
| NSOM | Near-field scanning optical microscopy |
| nt | Nucleotide |
| NV | Nitrogen vacancy |
| PBS | Phosphate buffered saline |
| PEG | Polyethylene glycol |
| PL | Photoluminescence |
| Qdot | Quantum dot |
| rcf | Relative centrifugal force |
| rpm | Revolutions per minute |
| RT | Room temperature |
| s | Second |
| SEM | Scanning electron microscopy |
| SP | Surface plasmon |
| SPPs | Surface plasmon polaritons |
| SPR | Surface plasmon resonance |
| ss | Single-stranded |
| STEM | Scanning transmission electron microscope |
| T | Transverse |
| TEM | Transmission electron microscopy |
| TIRF | Total internal reflection fluorescence |
| Tris | Tris(hydroxymethyl)aminomethane |
| tSEM | Transmission scanning electron microscope |
| UV | Ultraviolet |
| Vis | Visible |
| ZLP | Zero-loss peak |
| ZPL | Zero-phonon line |

# 1 INTRODUCTION

## 1.1 Plasmonics

Plasmonics is an emerging and rapidly growing field of science and technology, which exploits the peculiar optical properties of metallic nanostructures to generate, confine, manipulate, control and route light at the subwavelength scale [1]–[3]. This demanding field has broad applications in physics, chemistry, materials science, biology, medicine and integrated optics. To give some examples, field-enhanced spectroscopies [4], [5], advancing near-field optical techniques [6], [7], optical switching, transmission and light-emitting devices [8]–[10], metamaterials [11], [12], tracking biological dynamic processes [13], drug delivery [14] and cancer diagnosis and therapy [15], [16]. There are three fundamental driving forces behind the advancement of the plasmonics. First, development of chemical synthesis, self-assembly and lithographic techniques that allow production of metallic nanostructures and assemblies with large diversity and high complexity. Second, development of spectroscopy and measurement techniques which enable high-resolution mapping, imaging and ultra-fast time-scale probing of plasmonic structures. Last, advancement of electromagnetic modeling methods which are expanded to simulate complex plasmonic systems and thereby provide detailed information and quantitative analysis.

### 1.1.1 Surface plasmons

The interaction of electromagnetic waves with metals relies on the response of collective oscillation of free conduction electrons in metals, called plasmon, to the electric field. The Drude model based on classical mechanics [17] describes that the oscillation of the free electrons is 180° out of phase with the electric field which results in a negative dielectric constant for the most metals. That leads a very high reflectivity and is the reason why bulk metals are shiny. In contrast, in the case of the interaction of light with metal nanostructures, the feature of plasmons is prominent and resulting extraordinary optical scattering and absorption properties in the visible regime for the noble metal nanostructures such as copper, aluminum, silver and gold [18].

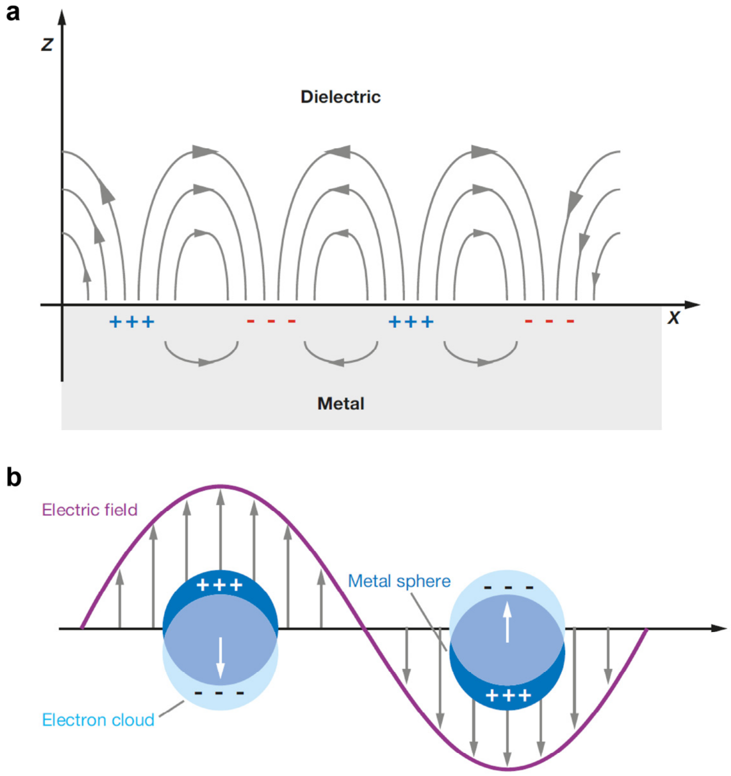

***Figure 1.1 | Schematic illustrations of surface plasmons****. (a) Propagating surface plasmon (or surface plasmon polaritons) at the metal-dielectric interface. (b) Plasmon oscillation in spherical metal nanoparticle (localized surface plasmons). Reproduced from [19].*

Figure 1.1a depicts a surface plasmon (SP) which propagates as an electron density wave when the electromagnetic wave interacts with a thin metal film. This incident light induces alternating positive and negative charges on the metal surface, which lead to propagating SPs, often called surface plasmon polaritons (SPP), in the x- and y-directions along the metal-dielectric interface. Their electromagnetic field intensity is highest at the metal surface and decays exponentially in the z-direction [20]. When the light interacts with metal nanoparticles (in the case of the size particles is much smaller than the wavelength of incident light), the plasmons locally oscillate around the particles. This is so-called localized surface plasmons (LSPs), see Figure 1.1b. The LSPs are able to squeeze light into nanoscale volumes and generate large local electromagnetic fields enhancements. This enhancement decreases evanescently with the distance from the surface.

The surface plasmon wave (or electron density wave) is a transverse magnetic polarized wave (magnetic vector is perpendicular to the direction of propagation of the surface plasmon wave). The SPs resonate when the frequency of plasmon mode (dipole, quadrupole, etc. depending on the size and type of metal structure) is the same as the frequency of incident light. This condition is called surface plasmon resonance (SPR) and the strongest signal of SP is obtained at this condition. The wave vector of the surface plasmon is related to the dielectric constant (hence refractive index) of both surrounding medium and metal. The local environment can be sensed by measuring the shift of SPR wavelength or measuring the changes of angle in the reflected signal. Therefore, the SPR is widely used in well-established optical biosensing technology [21], [22].

### 1.1.2 Optical properties of metal nanoparticles

The optical properties of metallic nanoparticles have fascinated people since the Romans. Historically, metal nanoparticles were used to stain glass windows and ceramic pottery, such as the example seen in Figure 1.2a, the Lycurgus cup from the 4th century A. D. The glass cup displayed in the British Museum exhibits a ruby red color when it is viewed in transmitted light, whereas it appears green in reflection. This behavior arises from small gold nanoparticles embedded in the glass. Although this effect has been known for centuries, the scientific understanding has only begun with the development of classical electromagnetic theory.

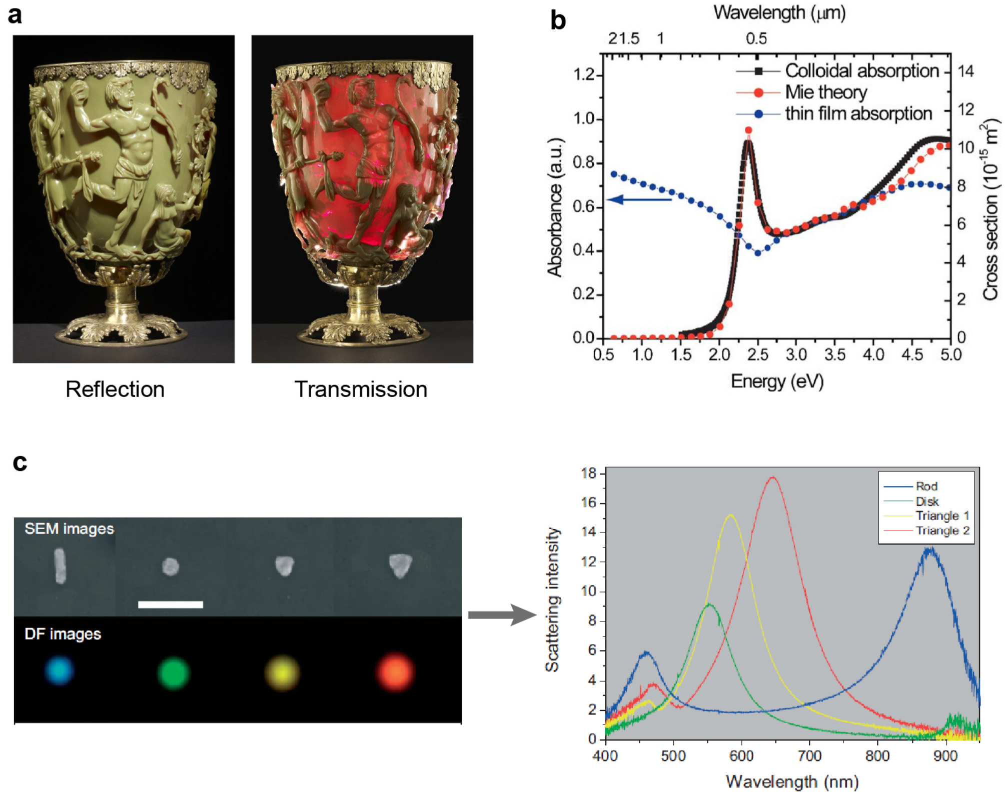

***Figure 1.2 | Optical properties of noble metal nanoparticles.*** *The Lycurgus glass cups, demonstrating the green color in reflected light (left), and bright red color in transmitted light (right), from the British Museum [23]. (b) Calculated (red dots) and measured (black dots) absorption spectra of 30 nm gold nanoparticles. For comparison, the calculated absorption spectrum of a thin gold film (blue dots) [24]. (c) Scanning electron micrographs (top-left), dark-field images (bottom-left), and dark-field scattering spectra (right) of a rod, a disc, and two triangles (from right to left), scale bar 300 nm [25]. Reproduced from the respective references of the panels.*

In 1908, Gustav Mie developed a theory approximating the solution of Maxwell's equations, describing the interaction of visible light with submicron size metal particles [26]. This approximation explains the strong absorption of green light by a spherical gold nanoparticle when the plane wave is incident on the particle, see Figure 1.2b.

The optical properties of metal nanoparticles such as silver, copper, gold show differences compared to their bulk or thin-film optical responses. This is due to LSPs that strongly scatter and absorb light. Figure 1.2b demonstrates the calculated and measured absorption spectra of 30 nm spherical gold nanoparticles dispersed in water. The calculated spectra for gold sphere were obtained by solving Maxwell's equations based on Mie theory. As shown in the spectra, this quasistatic approximation matches the measurement of the gold nanoparticle nanoparticles with a diameter $d << \lambda$. In contrast, the absorption spectrum of a thin gold film (blue dots in Figure 1.2b) shows a remarkable difference compared to the optical response of the nanoparticles. The film absorbs light all over the near-infrared and visible spectral regions due to free electron absorption. In the case of gold nanoparticles, this process is strongly dampened at the energies below 2 eV in the spectrum and shows dipolar SPR absorption peak at 2.25 eV (~550 nm in wavelength).

The colors displayed by metal nanoparticles depend on the type of material they are made of, their size and shape, and the surrounding medium. Figure 1.2c shows electron micrograph and dark field microscopy image of a rod, a disc and two different sized of triangles fabricated by electron-beam lithography. They exhibit different colors in the dark-filed image due to their different SPR frequencies which were detected in scattering spectra. As explained in the previous section, the oscillating electric field of the incident light produces a force on the free conduction electrons on the surface of the metal nanoparticles, which induces a formation of a dipole (polarization of charges on the particle). The displacement of the electrons with respect to the positive charges (redistribution of the charges) leads to a restoring force. This restoring force and the polarizability of metal particles depend on the shape of the metal particle, permittivity of metal and the surrounding medium. The relative permittivity (refractive index) is not constant but varies with frequency (wavelength). The color exhibited in metal particles is defined by SPR condition where the frequency of incident light and plasmons are closest. The SPR for a gold nanodisc occurs in the green part of the spectrum (~550 nm), whereas for a gold nanorod it occurs in near infrared region (or infrared depending on the aspect ratio of the rod), as it is shown in Figure 1.2c scattering spectra.

## 1.2 DNA nanotechnology

There are two fundamental approaches for the fabrication of nanostructures: ‘top-down’ and ‘bottom-up’. The top-down approach uses large-scale materials and reduces their size to form the small structures with desired dimensions and patterns. This process requires rather expensive and sophisticated instrumentation. Conversely, the bottom-up approach uses the information of the molecules to direct the self-assembly into nanostructures. It provides highly parallel production of nanostructures with large diversity and high complexity.

In the bottom-up methods, DNA is widely-used as a building material [27], [28] for many reasons. DNA has a unique molecular recognition property which allows programmable intra- and inter-molecular interactions to construct pre-defined micro and nanostructures [29]–[31]. DNA is a stiff, biocompatible molecule that can be cheaply synthesized [32], [33]. For these reasons, the use of DNA has received considerable attention in nanotechnology for applications in various fields [34], [35].

### 1.2.1 The structure and properties of DNA

Deoxyribonucleic acid (DNA) is a molecule that stores the genetic instructions necessary for functions and biological evolution of all organisms and some viruses. In 1869, DNA was first isolated from the leukocytes’ nuclei (white blood cells) and named as “nuclein” by Friedrich Miescher [36]. In 1953, the double helical molecular model of DNA was developed by James Watson and Francis Crick [37] based on the X-ray crystallography data obtained by Rosalind Franklin and Maurice Wilkins [38]. DNA is a long polymer composed of repeating units so-called “nucleotides”. The DNA double helix structure is formed by hybridizing two complementary chains. The diameter of the right-handed double helix is 2 nm, one helical turn is 3.4 nm (10.5 nucleotides) and the spacing between adjacent nucleotides is 0.34 nm [39], see

Figure 1.3a. Each nucleotide (nt) consists of a five-carbon sugar (deoxyribose), one of four nitrogenous nucleobases adenine (A), thymine (T), cytosine (C) or guanine (G) and a phosphate group. The nucleobases are divided into two groups: purines (A and G) are fused five- and six-membered heterocyclic compounds and pyrimidines (T and C) are consisting of a six-membered ring.

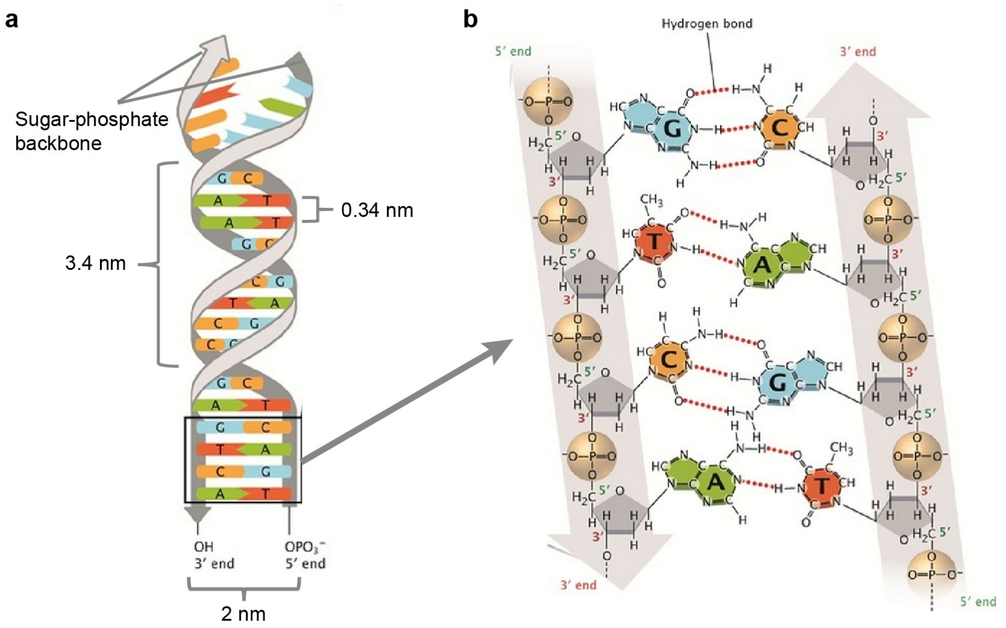

***Figure 1.3 | Scheme of the B-form, right-handed DNA double helix structure.*** *(a) Three-dimensional DNA double helix model by James Watson and Francis Crick. (b) Chemical structure and the Watson-Crick base pairing of the DNA double helix. Reproduced from [40].*

The backbone of the DNA strand is composed of alternating sugar and phosphate residues. These sugar residues are interconnected by phosphodiester bonds between the third and fifth carbon atoms of the adjacent sugar rings. In the DNA double helix, each strand has a polarity which is dictated by the sugar groups, and the two strands have opposite directionality. The DNA strands are antiparallel with a terminal phosphate group at the one end and a terminal hydroxyl group at the other end [40], see Figure 1.3b. As a result of the asymmetric arrangement of the DNA double strands, the DNA double helix has unequally sized two grooves: a major groove with a width of 2.2 nm and a minor groove with a width of 1.2 nm [41]. The major grove is usually more accessible to DNA-binding proteins, for example transcription factors, compare to the minor groove [42].

DNA can exist in various forms including right-handed B-DNA, A-DNA and left-handed Z-DNA [43]. DNA adopts the conformation depending on the base sequence and the environmental factors such as type and concentration of metal ions, hydration level and the presence of polyamines in solution [44]. For example, A-form is shorter, wider and more compact compared to the B-form, and the A-form occurs when the DNA is dehydrated or for RNA. Different DNA conformations can be observed by X-ray crystallography, but the B-form is the most common form under physiological conditions.

The DNA double strands are held together by Watson-Crick base pairing i.e. A-T base pairs with two hydrogen bonds and G-C base pairs with three hydrogen bonds [40], [45], [46]. Therefore, the DNA with rich G-C pairs is more stable than the DNA with lower G-C pairs [47]. However, the hydrogen bonding between base pairs is a relatively weak molecular force, less than one-tenth that of a covalent binding energy [48], it is a cooperative effect that stabilizes the DNA molecule. The double helix structure is maintained mainly by base stacking (π-stacking) interaction between adjacent bases [49]. The stability of DNA depends on the length, percentage of GC content, sequence (base stacking), the concentration of the DNA and the ionic strength. The stability can be determined by measuring the melting temperature at which half of the double-stranded DNA molecules fall apart to single-stranded DNA molecules [50], [51].

### 1.2.2 Structural DNA nanotechnology

In the early eighties, Nadrian Seeman introduced a revolutionary idea i.e. DNA is not only a genetic information carrier but DNA can also be used as a building material owing to its molecular recognition properties (Watson-Crick base pairing). His idea was to form a 3D crystal by self-assembling DNA branched-junctions with single-stranded overhangs (sticky ends, see Figure 1.4a) and to use this 3D crystal as a scaffold for the precise organization of proteins and other bio-macromolecules (Figure 1.4b), hence enabling the macromolecular crystallization [52].

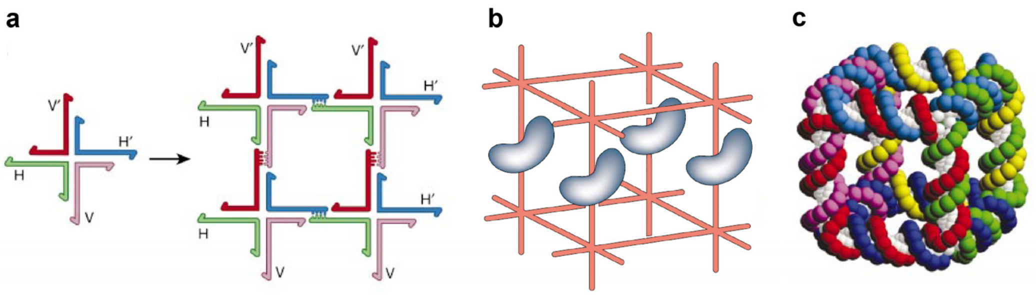

***Figure 1.4 | The groundwork of structural DNA nanotechnology.*** *(a) Self-assembly of DNA branched-junctions into a 2D crystal. (b) A DNA scaffold for positioning bio-macromolecules. (c) 3D DNA cube by ligation of DNA branched junctions. Reproduced from [53].*

In 1991, a DNA 3D cube (Figure 1.4c) was experimentally constructed by ligating the three-arm junctions with sticky-ends [54]. Afterwards, double-crossover [55] and triple-crossover [56], [57] molecules were introduced as DNA self-assembly building blocks to increase rigidity. These molecules were then used to build periodic 2D crystal lattices by sticky ends hybridization [58], [59]. This approach was further developed with the aid of computational design, and various complex shapes were assembled into 2D and 3D nanostructures by using single-stranded DNA tiles [60], [61]. The concept founded by Seeman was an important breakthrough towards the development of DNA nanotechnology.

### 1.2.3 DNA origami

In 2006, Paul Rothemund introduced a breakthrough approach, called DNA origami, which is based on folding a long, single-stranded DNA molecule into arbitrary 2D shapes [62]. This is achieved by the addition of typically around 200 synthetic short oligonucleotides, “staple strands” that bring together selected parts of the long, single DNA strand, “scaffold strand”, see Figure 1.5a. The circular scaffold strand is typically from the M13mp18 virus and ~7 kilobases in length. He demonstrated that staple strands and scaffold strand were self-assembled by Watson-Crick base pairing in one-pot annealing reaction, resulting in desired planar DNA origami shapes including squares, five-pointed stars, smiley face and many others (Figure 1.5b). These DNA origami structures are about 100 nm in diameter with 6 nm spatial resolution. He further showed patterning by designing hairpins at a defined position and combining DNA origami shapes by introducing "extended staples" that connected shapes along their edges. The patterned DNA origami structures such as a map of the western hemisphere and letters of "DNA" were assembled and larger 2D periodic lattices were realized by the controlled combination of DNA origami structures. The results presented in the paper of Rothemund [62] reveal that DNA origami is a programmable and highly versatile technique, which provides a simple, inexpensive and scalable way for producing nanostructures of high complexity.

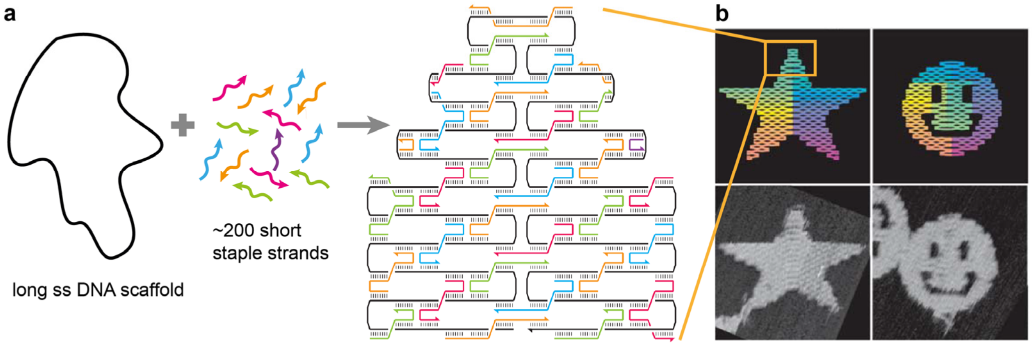

***Figure 1.5 | DNA origami technique by Rothemund.*** *(a) A long circular genomic DNA strand folded into the desired shape with the aid of small staple strands. (b) Top, diagrams of the computationally designed star and a smiley face. Bottom, AFM images of 2D DNA origami shapes. Reproduced from [62].*

In 2009, the group of William Shih transformed the DNA origami approach into 3D structures by pleating the layers of double helices constrained to a honeycomb lattice with the aid of crossover staple strands, see Figure 1.6a [63]. Subsequently, a stacking strategy of the multilayer of DNA double helices into square lattices was demonstrated for densely packed 3D structures [64]. Both honeycomb and square lattices can be used to efficiently create complex and rigid 3D DNA origami structures. DNA origami structures were designed by using a graphical interface-based, computer-aided software. This program is called caDNAno and developed by Shawn Douglas [65]. Furthermore, twisted and curved structures were introduced by targeted base insertions/deletions to adjust the distance between crossovers [66], see Figure 1.6b. In Dietz *et al.* study, they showed that the degree of curvature could be quantitatively controlled and a radius of curvature down to 6 nm was achieved [66]. Another strategy was demonstrated by Gerling *et al.* that discrete 3D DNA origami objects could self-assemble based on shape-complementarity without base pairing [67]. With this principle, dynamic devices including an actuator, a switchable gear, and a nanorobot were constructed, see Figure 1.6c. These multimeric assemblies were stabilized by base stacking interactions that compete against electrostatic repulsion between the interfaces of the multimers. They achieved to finely tune the conformation of the assemblies by the parameters such as cation concentration or temperature.

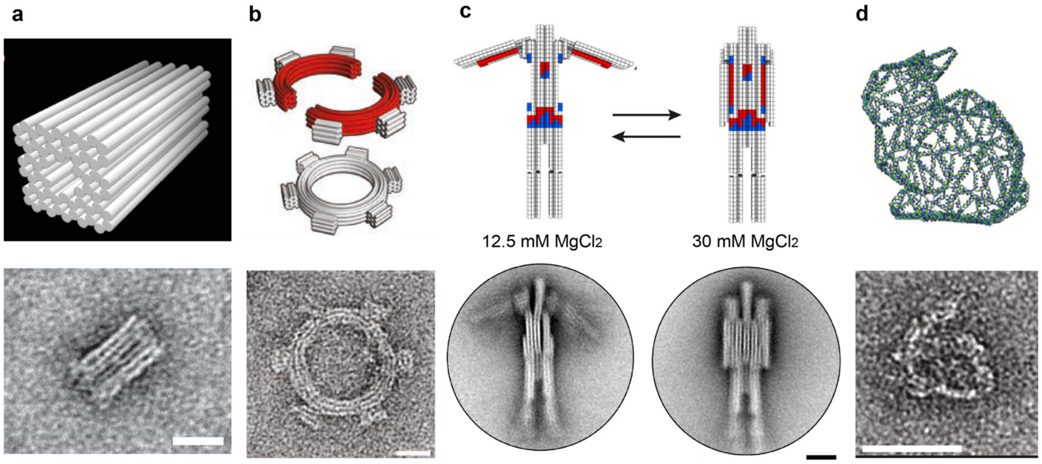

***Figure 1.6 | 3D DNA origami structures.*** *Top, the schemes of the designed DNA origami structures. Bottom, TEM micrographs of the respective assembled structures. (a) Square nut structure by Douglas et al. [63], scale bar, 20 nm. (b) Curved structure by Dietz et al. [66], scale bar, 20 nm. (c) DNA origami nanorobot by Gerling et al. [67], scale bar, 25 nm. (d) A Stanford bunny structure, 3D mesh rendered in DNA by Benson et al. [68], scale bar, 50 nm. Reproduced from the respective references of the panels.*

In addition to these strategies, different designs and structures were developed by several other groups. For examples, 3D DNA prestressed tensegrity structures [69], DNA gridiron nanostructures [70] and DNA box with a controllable lid [71]. Most recently, wireframe 3D DNA origami meshes have been created with the advanced computational designs [68], [72], [73], one example Stanford bunny is depicted in Figure 1.6d. In that study, the computer algorithm was developed to convert the structure into a triangulated mesh and the contour of the structure was traced. Unlike conventional DNA origami structures assembled from closely packed helices, these mesh designs have more open conformations thereby, they are more stable in low-salt buffers that usually used in biological assays.

### 1.2.4 DNA origami based plasmonic nanostructures

DNA origami is one of the most promising techniques which provides not only highly parallel fabrication of structures with large diversity but also the organization of materials with nanometer precision. Since DNA has remarkable recognition features and each unique staple strand in DNA origami structure can be used as a specific site, various functional elements have been precisely arranged including metallic nanoparticles [74]–[76], quantum dots [77], [78], fluorescent dyes [79], fluorescent nanodiamonds [80], proteins [81], [82], carbon nanotubes [83] and most recently semiconducting polymers [84]. The combination of metallic nanoparticles, quantum dots, and organic dyes is also hierarchically assembled [85]. The focus in this section is particularly on DNA origami-metallic nanoparticles assemblies for the study of plasmonics.

Ding *et al.* [74] demonstrated a strategy to construct a linear chain of six AuNPs with pairs of 5, 10 and 15 nm sizes on planar triangular DNA origami structure, see Figure 1.7a. The bowtie-like alignment was achieved by using orthogonal binding sites for the attachment of each size of AuNPs and functionalizing each size of AuNPs with thiol-modified oligonucleotides that were complementary to the corresponding binding sites. The binding sites were extended from the DNA origami structure and each binding site comprises three identical ss DNA extensions. Electron micrographs confirmed the designed arrangement. The UV-Vis absorption measurement of these assemblies was performed, and 5 nm red-shift was observed on the plasmon resonance peak. Since the inter-particle distance (~10) is comparable with the diameter of the particles, the plasmon coupling was not strong thereby the shift was not large. In addition to AuNPs, gold nanorods [86], silver nanoparticles [87] were also assembled on the same DNA origami design with the same strategy. Recently, the group of Ilko bald demonstrated closely spaced arrangement of 10, 20, and 60 nm AuNPs on the same 2D triangular origami structure as plasmonic gold nanolenses for surface-enhanced Raman scattering (SERS) [88].

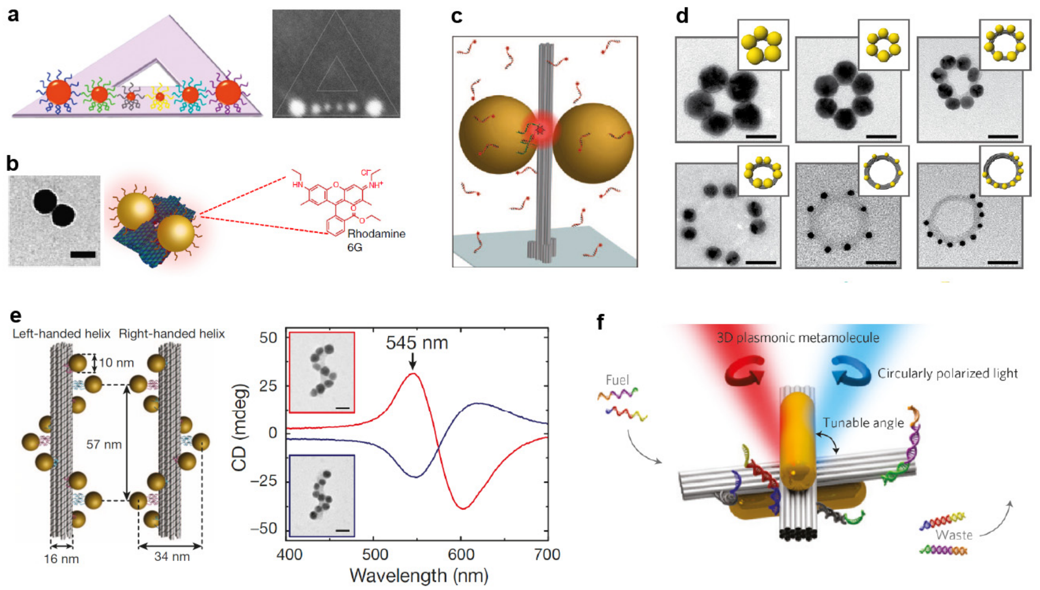

***Figure 1.7 | DNA origami templated plasmonic nanostructures.*** *(a) Different-sized gold nanoparticles assembled on a triangular DNA origami template [74]. (b) Gold nanoparticle dimer assembled a DNA origami platform for surface-enhanced Raman spectroscopy [89]. (c) DNA origami pillar with two gold nanoparticles forming a dimer for fluorescent enhancement [90]. (d) DNA origami-gold nanoparticle ring structures [91]. (e) DNA origami gold nanoparticle helices for circular dichroism [75]. (f) Reconfigurable 3D plasmonic metamolecules [92]. Reproduced from the respective references of the panels.*

The AuNP dimer assemblies act as nanoantennas so they create a local field enhancement, so-called plasmonic hot-spot, for fluorescent [90] and Raman [89], [93] signals. Thacker *et al.* demonstrated the 2x40 nm AuNPs dimer assemblies on DNA origami structure with 3.3 nm gap size [89], Figure 1.7b. They observed a local field enhancement of several orders of magnitude by the SERS detection of dye molecules. Acuna *et al.* [90] reported a nanoantenna from two 100 nm AuNPs assembled on a DNA origami nanopillar with 23 nm inter-particle distance. A docking site was introduced on the gap for the attachment of a dye-modified oligonucleotide, see Figure 1.7c. A maximum of 117-fold fluorescence enhancement was achieved when the dye molecule was positioned in the gap.

The group of Tim Liedl fabricated a wide variety of ring-shaped plasmonic metamolecules that are composed of four to eight single AuNPs, see Figure 1.7d [91]. Scattering spectra of single rings attached to a substrate (dried state) and absorption spectra of the rings (dispersed in solution) were used to reveal plasmonic features. Ring structures exhibited dipolar, multipolar and magnetic plasmon resonance modes. The correlation between the plasmon resonance modes and shape of the structures was investigated.

Two reports [75], [94] from two independent groups demonstrated that chiral assembly of AuNPs on DNA origami tubes (Figure 1.7e), exhibited defined circular dichroism, (CD), which the differential absorption of left and right circularly polarized light) in the visible range. The CD signal originated from the plasmon coupling between the particles, therefore the intensity of the signal was strongly dependent on the particle size and the inter-particle gap. The strength of the signal was increased up to 400-fold and CD peak was shifted to longer wavelengths by the metal growth of 10-nm seed AuNPs that were already into the chiral assembly. By the controlled metal growth (both silver and gold were utilized), the gap size can be tuned which led to tailoring optical response of the chiral plasmonic assemblies. After these reports, numerous CD studies [95], [96] came out including 3D gold nanorods-DNA origami metamolecules with tunable conformational states (Figure 1.7f) [92], 3D chiral tetramers [97], gold nanorod helical superstructures [98] and most recently chiral gold nanorod-nanoparticle helical superstructures [99].

## 1.3 Plasmonic waveguides based on metal nanoparticles

The fundamental problem of integrated optics is the transmission of light energy in materials which are much smaller than the corresponding wavelength of light [100]. With plasmonic waveguides based on closely spaced metal nanoparticles, sub-micron 3D confinement is achievable with defined surface plasmon resonances at a particular frequency (typically in Vis and IR regimes). For this reason, the focus in this section is particularly on plasmonic waveguides based on metal nanoparticles.

The groundbreaking work by Maier *et al.* demonstrated a direct experimental observation for energy transfer along the 1D metal nanoparticle chain waveguides [101]. The waveguide structures were fabricated serially by electron beam lithography, and consisting of silver nanorods with dimensions of 90 nm x 30 nm x 30 nm and inter-particle spacing of 50 nm. The far-field extinction spectra were measured upon transverse illumination (along to the long axis of rods chain) and a significant blue-shift, due to near-field plasmon coupling between the rods, was observed compared to the single rod. The surface plasmons in the waveguide were locally excited by the tip of a near-field optical microscope (NSOM) and the energy transfer along the rod chain over a distance of 500 nm was detected by the far-field emission of polymer beads containing fluorescent dyes, see Figure 1.8a. In this study, a decay length of 6 dB per 195 ± 28 nm was obtained. Afterwards, the major aspects of this coupling approach were verified by the numerical analysis report [102], and the applications such as condensers [103] and nanolenses [104] were suggested. However, in these studies, the scalable fabrication, hetero-complex structures with short inter-particle spacing are not possible.

The group of Stephan Link proposed a new fabrication technique which is based on the combination of a serial top-down approach and parallel bottom-up assembly of monocrystalline metal nanoparticles [105]–[107]. The chemically synthesized silver nanoparticles were deposited into the polymer trenches which were written by electron beam lithography. Complex chain geometries including straight, branched, bent

(Figure 1.8b) were characterized by bleach-imaged plasmon propagation far-field fluorescence technique, and a propagation length of ~8 micron was achieved for bent silver nanoparticle chains.

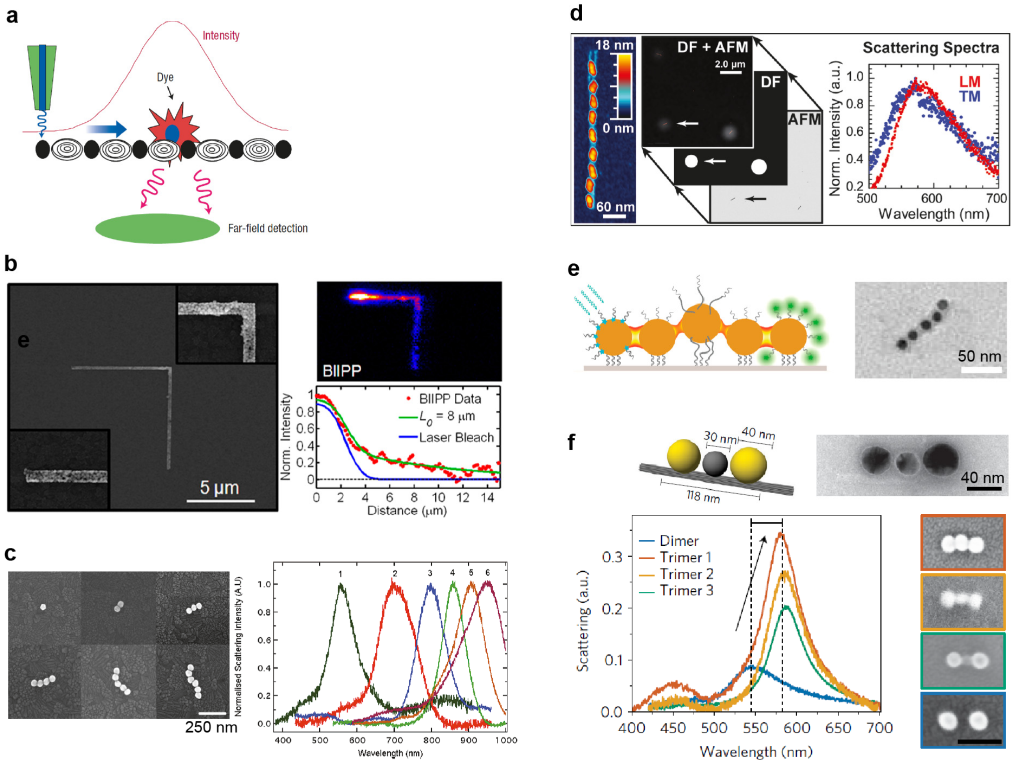

***Figure 1.8 | Plasmonic waveguides based on metal nanoparticles.*** *(a) Schematic illustration of excitation and detection of energy transport in silver-nanorod based plasmonic waveguides by NSOM, by Maier et al.[101]. (b) Bent plasmonic silver nanoparticle multi-chain waveguides by Solis et al.[107]. (c) Gold nanoparticle chains from monomer to hexamer by Barrow et al.[108]. (d) Multi-scaffold DNA origami-based nanoparticle waveguides by Klein et al.[109]. (e) DNA origami-based gold nanoparticle waveguide with a thermomechanical switch by Vogele et al.[110]. (f) DNA origami-templated heterogeneous trimer structure for non-dissipative and ultrafast energy transport by Roller et al.[111]. Reproduced from the respective references of the panels.*

The number of chains in these geometries was random, and these structures were composed of typically ~4 nanoparticles in width and ~3 nanoparticles in height.

Furthermore, they showed the properties of radiative and non-radiative plasmonic sub-modes for single nanoparticle assemblies [112]. Similar to this fabrication approach, the group of Andreas Fery showed linear assemblies with controllable line width, single particle, dimer or tetramer chains with an inter-particle spacing of 1−2 nm. The chains were fabricated over centimeter-squared areas by plasma oxidation of stretched polymer templates assisted assembly of protein-coated chemically synthesized gold nanoparticles [113]. UV/Vis/NIR spectroscopy results confirmed the strong plasmonic coupling between the particles. The shortcoming of these methods is there is no spatial control over individual particle positioning, thus producing hybrid plasmonic systems is not possible.

The work by Barrow *et al.* proposed a pure self-assembly approach for linear chains of gold nanoparticles from monomer to hexamer with an inter-particle spacing of 1 nm [108], see Figure 1.8c. The self-assembly was based on the functionalizing of gold nanoparticles with thiolated oligonucleotides. The gold nanoparticles were linked by DNA hybridization and therefore random assemblies and aggregates were also observed. The light scattering signal of these linear chain assemblies showed a gradual red-shift of the surface plasmon resonance with increasing chain length. The same group later on investigated the same assemblies by electron energy loss spectroscopy and mapped the bright and dark (radiative and non-radiative) plasmonic modes of the chains [114]. Although this study provides extremely short inter-particle spacing, it does not provide the control over the chain length. The maximum number of AuNPs in the chain they randomly found is six.

The DNA directed self-assembly of particles into linear chains was advanced in the work of Klein *et al.* by using multi-scaffold DNA origami nanotubes and controllable arranging of gold nanoparticles on the tubes [109]. These DNA origami templated waveguides were composed of gold nanoparticles with a diameter of 10 nm and a 14 nm center-to-center spacing between adjacent particles, see Figure 1.8d. The far-field polarization spectroscopy results revealed a 20 nm red-shift of the plasmon resonance of the gold nanoparticle chains. This study uses DNA origami method, hence there is a spatial control over the particle positioning. However, they used small particles with comparable inter-particle distances, and thus the plasmon coupling is not strong.

The work by Vogele *et al.* demonstrated the energy transfer through a single layer of DNA origami templated gold nanoparticle chain over a distance of 50 nm [110]. The waveguide was composed of five gold nanoparticles with a diameter of 10 nm and ~2 nm inter-particle spacing. The waveguide was excited at one end by donor fluorescent dyes which were attached to the first particle, and energy transfer was detected by fluorescence microspore measurement by the emission of acceptor dyes which were located at the last particle, see Figure 1.8e. The bulk fluorescent measurement was in solution and the results showed a very little spectral difference between the emission of the acceptor dye on the waveguides and the emission of the dyes on the single particles. The idea of this study is similar to the Maier *et al.* [101], see Figure 1.8a, however they use very small AuNPs (~5 nm) and the overall waveguide length is 50 nm. For this reason, it cannot be considered as a waveguide. The shortcomings of this study are: far-field measurement technique was used for the bulk sample measurement in solution with unknown structure conformations, lack of important control experiments, and lack of simulation results.

The study by Roller *et al.* demonstrated a DNA origami templated assembly of heterogeneous triple particle system consisting of two gold nanoparticles (40 nm in diameter) and a silver particle (30 nm in diameter) in between the two gold nanoparticles [111], see Figure 1.8f. The strong plasmonic coupling and strong hot-spots between the particles led to an almost lossless coupling and coherent ultrafast energy transfer over a distance of 118 nm. The dark-field scattering spectra revealed a ~40 nm red-shift between the homo-dimer (with missing silver particle in the middle, with 38 nm gap between the gold particles) and the hetero-trimer assemblies. This study is one of the best compared to the others in Figure 1.8. It provides scalable production with controlled heterogeneous particle assembly, and the modeling results strongly support experimental findings. However, for the waveguiding purpose, it is too short (118 nm in length) and this study used a far-field optical technique. In order to spatially resolve SP modes for the waveguiding, near-field techniques are required.

## 1.4 Characterization techniques for plasmonic nanostructures

In general, microscopy techniques can be classified into three categories: optical microscopy, electron microscopy, and scanning probe microscopy. They use light (optical microscopes), electrons (electron microscopes) or nanoscale-sharp tips (scanning probe microscopes) for the excitation and imaging the samples. In addition to obtaining static images, the excitations of the samples can provide the information about dynamic evolution and interactions in the samples. Therefore, the focus is to perform spectroscopy with the highest spatial and spectral resolution for the study of plasmonic systems. Figure 1.9 depicts an atlas of experimental spectroscopy techniques which are usually used to characterize plasmonic systems. The spectroscopy techniques are positioned in the atlas according to their spatial and energy resolutions.

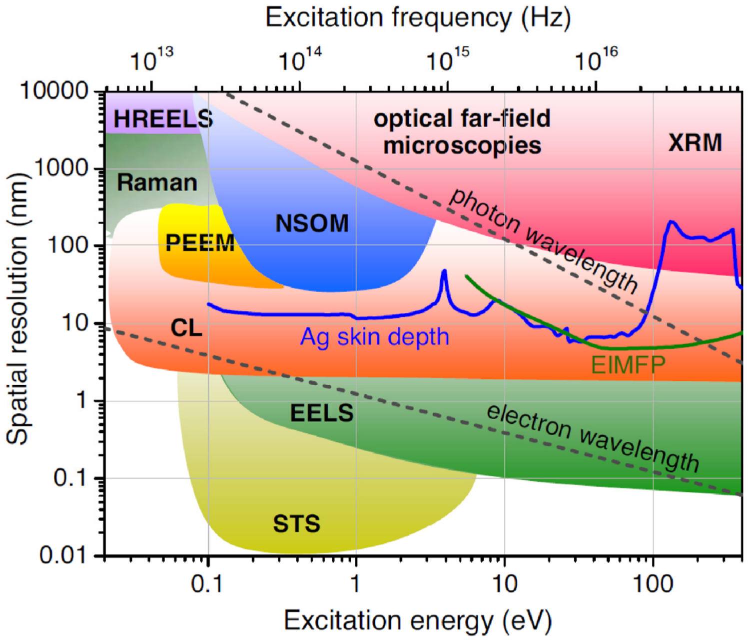

***Figure 1.9 | Atlas of spatially resolved spectroscopy techniques.*** *Reproduced from [115].*

Far-field optical microscopes including fluorescence microscopes, dark-field microscopes, circular dichroism and UV-Vis spectrophotometer are widely-used techniques to study plasmonic structures, but are in principle diffraction-limited to a resolution of about half of the wavelength of light. Several super-resolution microscopy techniques have been advanced to circumvent the diffraction limit and shortened the lateral resolution down to below 100 nm [116]. However, these optical techniques often require special fluorescent markers.

The developments in x-ray microscopy (XRM) allowed a resolution of sub-15 nm for imaging at a photon energy of 250 eV [117]. Near-field scanning optical microscopy (NSOM) uses a nanoscale tip that collects or illuminates the light. Using NSOM localized probes, the spatial resolution can be increased to tens of nanometer [118]. However, the spatial resolution is limited by the diameter of the tip which is typically ~50 nm. Scanning tunneling microscopy/spectroscopy (STM/STS) can yield a sub-angstrom spatial resolution (best on the map) and 0.1 eV energy resolution [119]. However, STS applies only for metallic samples and a close proximity between tip and sample is required to achieve sub-angstrom resolution, thereby single-electron excitations dominate the spectra which makes SPR peak indistinguishable in the spectra. In general, scanning probe techniques rely on the tip geometry that can be experimentally challenging to control and the scanning can often be slow.

On the other hand, electron microscopes are fast and reliable, thus the best option for providing sub-nanometer spatial resolution and <0.1 eV energy resolution [120] for investigation of plasmonic systems. Electron microscope based spectroscopies can be classified according to the type of the measured signal. For instance, photoemission electron microscopy is based on the photoelectric effect. For this, the sample is illuminated by light and emitted photoelectrons are collected and used to form image contrast [121], [122]. In contrary, cathodoluminescence (CL) spectroscopy uses a focused electron beam for the excitation and emitted light is detected. Electron energy loss spectroscopy (EELS) uses transmission electron microscope and measures the loss events due to inelastic scattering. EELS and CL are explained in more detail in chapter 4 and 5, respectively.

# 2 MOTIVATION AND OBJECTIVES

The main goal of current research is miniaturization of optical devices and integration of these devices into the optoelectronic circuitry. Current technologies have revolutionized fabrication of integrated optical components which are optical fibers and planar waveguides. However, these waveguides are not able to guide light around sharp corners [123]. Furthermore, the size of these devices is restricted by the diffraction limit, thereby there is a size mismatch between these waveguides (typically micron range) and integrated electronic component (typically nanometer range). There has been a remarkable effort on propagating SPs in metals over the last decades. However, the propagation of SPs in bulk metal decays evanescently when reducing the width of metal stripe below diffraction limit [124]. On the other hand, LSPs on the metal nanoparticles are able to confine light to a very small volume [2], [125], [126]. Metal nanoparticle based plasmonic devices can generate, guide and manipulate localized light for the miniaturized photonic circuits [127] thus for the next generation high-speed chip technology [124]. For this reason, metal nanoparticles play a key role in the revolution of that is pushing optics below the diffraction limit. Propagating nature of the SPs is indeed particular interest for carrying electromagnetic energy at the nanoscale [24], [128] for short-distance communications and bridging the size-gap between optical elements and electronic components.

There has been a significant amount of studies on metal nanoparticle-based plasmonic waveguides, and only a few of them reported a direct experimental realization of energy transport below the diffraction limit [9],[10]. However, most of the analyzed nanoparticle arrays rely on top-down fabrication methods, particularly electron beam lithography technique [101], [129], [130], which suffers from high cost, non-scalable production, and comparable inter-particle distances to the particle sizes (Maier *et al.,* see

Figure 1.8a). In addition, only one type flat structures can be fabricated with often crystal imperfections. Complex, multi-component, hybrid systems cannot be produced by lithography methods [131]. Alternatively, chemical synthesis can yield highly monodispersed and monocrystalline particles with a great variety of shapes and sizes including spheres, rods, cubes, triangles, stars, and many more [132]. Moreover, chemical synthesis methods provide low-cost, high scalable production. Other approaches for straight [106] and bent [107] (Solis *et al.,* see Figure 1.8b) closely packed gold and silver nanoparticle chains waveguides, respectively have been reported by combining self-assembly and lithography methods. These studies have revealed that low-loss and longer propagation length owing to extremely short inter-particle distances, which results in strong plasmon coupling. However, there is no spatial control over the positioning of individual particles in these assemblies. In addition, the dark-field and fluorescence optical spectroscopy results have clarified that the results are for collective coupling of several disordered particles in the chains but not a single particle chain.

On the other hand, DNA has been used for constructing programmable building blocks [133] and assembling colloidal metal nanoparticles into higher order, 3-D crystalline macroscopic materials [134], [135]. Moreover, DNA has recently received considerable attention for building complex plasmonic nanostructures [136], [137]. Particularly, DNA origami [28], [63] is one of the most promising approaches, which offers spatial control over the positioning of individual particles at the nanoscale with high yields [138]. DNA origami templated dimers [90], trimers [111], chains [109], [110] and chiral [75] metal nanoparticle assemblies have been experimentally realized. However, all these studies have been concentrated on the limited spatial resolution of optical microscopy techniques. Circular dichroism and fluorescent spectroscopy are commonly used, where far-field absorption and emission of bulk samples are measured in solution with often unknown chain conformation (see Figure 1.8e). Therefore, resulting in larger inter-particle distance due to the larger hydrodynamic sizes of ss DNA capped particles. Another widely used optical technique is dark-field microscopy, where single structure scattering is measured in a dried state. In this case, electron microscopy imaging is necessary to labor intense correlation of the same optically measured structure functions and morphologies.

Despite the fact that far-field optical spectroscopies provide insightful information about optical properties of particle assemblies, one cannot rely on far-field optical techniques to probe near-field radiative and non-radiative coupled plasmonic modes. Near-field scanning optical microscopy (NSOM) allows studying sample fluorescence, emission, and scattering properties. With using NSOM tip, surface plasmons can be mapped with the spatial resolution down to tens of nanometers. However, spatial resolution is still limited by the NSOM tip width (typically in the order of ~50 nm). On the other hand, electron microscopes are faster and are the most advanced method for probing both localized and propagating surface plasmons with sub-nanometer spatial resolution and less than 0.1 eV energy resolution [115], [139].

In this thesis, I propose a highly-parallel production of self-assembled plasmonic waveguides based on AuNPs with selectable sizes and spatial control over the inter-particle spacing that have been analyzed by the best choice of near-filed spectroscopy techniques. DNA origami-based self-assembled functional plasmonic waveguides with a high precision arrangement of gold nanoparticles and extremely short surface-to-surface particle distances combined with fluorescent nanodiamonds are demonstrated. Spectral and spatial characterizations of our waveguide system are cooperatively characterized by electron energy loss spectroscopy and cathodoluminescence imaging spectroscopy. SP modes are probed and direct observation of the energy transfer at the nanoscale is confirmed by cathodoluminescence emission of the fluorescent nanodiamond. Our findings open a new window for self-assembled plasmonic devices and as well as plasmon coupling to fluorescent nanodiamonds in nanophotonic applications.

# 3 TOWARD SELF-ASSEMBLED PLASMONIC WAVEGUIDES

Some of the results presented in this chapter were produced in collaborations. Automated image analysis was developed together with Dr. Friedrich W. Schwarz who was a former post-doc in the group of Prof. Stefan Diez in B CUBE - Center for Molecular Bioengineering, TU Dresden. The synthesis of larger gold nanoparticles based on hydroquinone reduction method was optimized together with Jingjing Ye who was a former master student in the group of Dr. Thorsten-Lars Schmidt in Center for Advancing Electronics Dresden, TU Dresden. In this chapter, sections 3.1, 3.2, 3.3 and 3.7 (except Figure 3.10) were reproduced with permission from the paper [D] Gür, F. N.; Schwarz, F. W.; Ye, J.; Diez, S.; Schmidt, T. L. Toward Self-Assembled Plasmonic Devices: High-Yield Arrangement of Gold Nanoparticles on DNA Origami Templates. ACS Nano 2016, 10, 5374–5382, DOI: 10.1021/acsnano.6b01537, Copyright 2016 American Chemical Society.

## 3.1 Introduction

DNA has recently received significant attention for building complex plasmonic nanostructures [136], [137]. Particularly, DNA origami [28], [62], [63], [66] is one of the widely-used, robust methods for producing anisotropic and addressable nanostructures. Functional elements such as (bio)molecules [140], [141] or nanoparticles can be introduced by functionalizing selected oligonucleotides. Gold nanoparticles (AuNPs) for example have been arranged into simple complexes using thiolated oligonucleotides since 1996 [134], [142], but complex DNA nanostructures enable more sophisticated arrangements and devices [136].

To observe the desired plasmonic effects on a single-device level and to enable applications in sensing or optoelectronics, the precise and high-yield placement of all nanoparticles of the device is of vital importance. The entire device may lose its functionality if one or more particles are absent. The yield for assemblies consisting of multiple nanoparticles is therefore determined by the yield of each individual coupling step to the power of the number of coupling steps. For example, even if the AuNP attachment yield is 80%, the final yield of a device consisting of eight particles such as the waveguide precursor described herein is only 17% ($0.8^8$). Therefore, much higher attachment yields are required. To this end, two related studies investigated the assembly yields of waveguide precursors as a function of the number of binding sites on multi-origami scaffolds [109], [143], but many other important parameters such as salt effects, AuNP functionalization protocols, linker chemistry or assembly kinetics have not systematically been studied so far. Moreover, in these previous and many other studies, only small (for example 5-10 nm) AuNPs were attached. To achieve the desired plasmonic effects such as waveguiding [130], circular dichroism [75], surface-enhanced Raman scattering (SERS) [89], [93], [144] or to create plasmonic antennas [90], much larger AuNPs with diameters of tens of nanometers have to be arranged. This is more challenging than to assemble small nanoparticles [94], [137].

## 3.2 High-yield assembly

For the high yield assembly study, a six-helix bundle (6-HB) DNA origami nanotube with eight binding sites consisting of single-stranded DNA extensions was designed. Thiol-modified oligonucleotides functionalized AuNPs hybridize to these complementary extensions, see Figure 3.1. Since small AuNPs with large inter-particle distances were employed, this complex was called “waveguide precursor” in this chapter. The influence of a set of parameters which are involved in assembly reactions was systematically investigated. The set of parameters includes salt effects, the gold−oligonucleotide linkage, stoichiometry, and the assembly kinetics as well as reversibility of assembly. For this, automated image analysis method is developed for the electron microscopy images of the resulting complexes. The automated image analysis allows to evaluate thousands of structures and eliminates laborious and potentially biased counting by experimentalists.

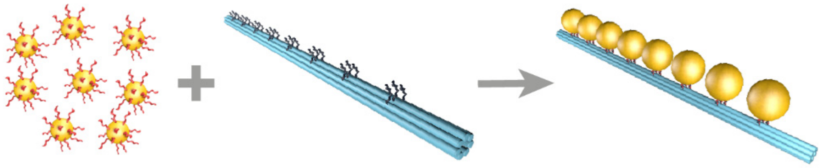

***Figure 3.1* | *Schematic illustration of waveguide self-assembly*.** *Oligonucleotides functionalized gold nanoparticles, six-helix bundle DNA origami nanotube with binding sites and resulting waveguide structure. For clarity, the shell of oligonucleotides on the AuNPs is not shown.*

### 3.2.1 Design and assembly

**DNA origami design**

The 6-HBs were used as templates to assemble "plasmonic waveguide precursors". These are composed of six parallel, interconnected DNA double helices [145], have a high aspect ratio [146] and are rigid enough to ensure linearity [147]. In order to facilitate the exchange of scaffold strands with other laboratories using different scaffolds, only the consensus sequence was used for the design resulting in ~400 nm long 6-HBs.

The size of DNA origami structures is determined by the length of the scaffold strand. Several M13 bacteriophage-based scaffold strands are used in the field such as p7249, p7308 or p8064 and many more, which consist of a 7,223 nucleotide long consensus sequence and specific inserts of varying length.

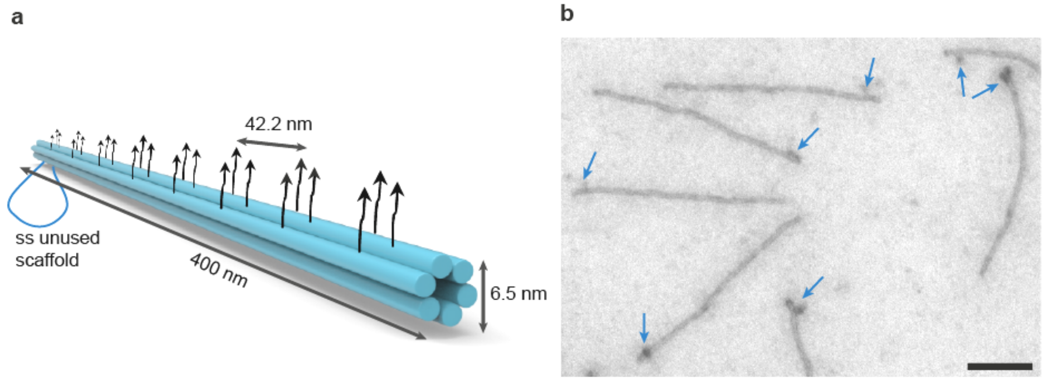

***Figure 3.2 | Design of six-helix bundle DNA nanotube with binding sites**. Schematic drawing (a) and a tSEM micrograph of six-helix bundle DNA nanotubes (b). Blue arrows indicate single-stranded unused scaffold. Scale bar, 100 nm.*

The 6-HBs were employed to align gold nanoparticles and provide eight binding sites for the AuNPs attachment. Each binding site is composed of three ss DNA extensions as depicted in Figure 3.2a with a designed center-to-center distance between two binding sites of 42.2 nm (126 bp). Using multiple extensions for each AuNP binding site increases the binding strength and positioning accuracy as reported previously [74], [143]. The single-stranded (ss) unused scaffold was designed to protrude from a helix opposite of the tethers. This unused scaffold loop is visible in transmission mode scanning electron microscope (tSEM) image, see Figure 3.2b. The binding sites are not visible.

### Assembly is a two-step process

The overall assembly is composed of two main reactions: the functionalization of AuNPs with thiolated ss oligonucleotides (reaction 1, Figure 3.3a) and the hybridization of the resulting DNA-functionalized AuNPs to their complementary ss overhangs on the DNA origami (reaction 2, Figure 3.3b). Both reactions typically involved in DNA-directed metal nanoparticle assembly were optimized.

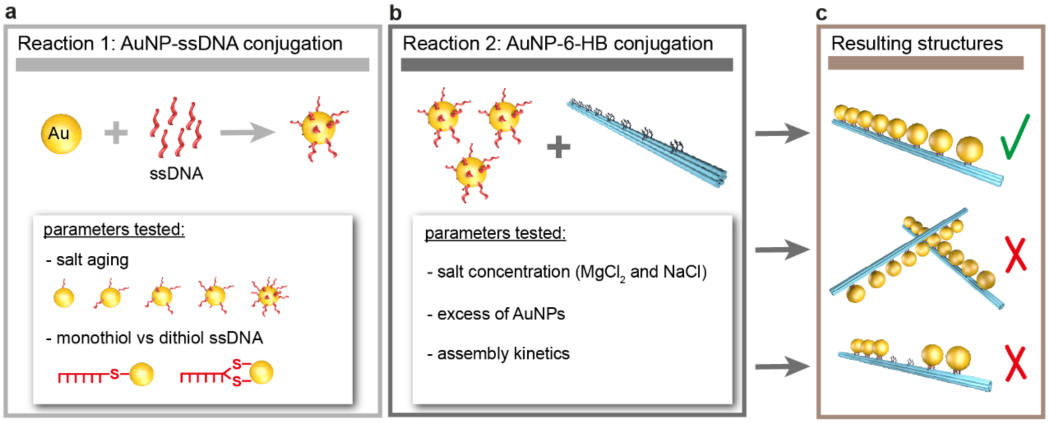

***Figure 3.3 | Schematic overview of the self-assembly steps of gold nanoparticles on six-helix bundle DNA origami nanotubes.*** *In reaction 1, AuNPs are functionalized with oligonucleotides (a), in reaction 2, these functionalized AuNPs hybridize to complementary tethers displayed on the DNA origami structure (b). The resulting structures can have different desired and undesired assemblies (c). The oligonucleotides on the AuNPs is not shown in (c) for clarity.*

AuNPs with a diameter of ~17 nm were synthesized by the standard citrate reduction method [148] and functionalized with commercially available thiolated oligonucleotides. For this modification, two approaches exist. Either only very few (for example 0-3) oligonucleotides are attached per AuNP and the conjugates with different stoichiometries are separated by gel electrophoresis [142] or the entire surface of the AuNPs is densely covered with many oligonucleotides [134]. For self-assembled plasmonic devices, a dense coverage of the nanoparticles is advantageous, as nanoparticles much larger than ~10 nm or AuNPs functionalized with short oligonucleotides cannot be separated well by gel electrophoresis. Moreover, the hybridization of densely covered particles to multiple tethers is known to yield more reliable connections [74], [75], [143], and these particles are well protected from aggregation by the electrostatic repulsion of the dense layer of highly negatively charged oligonucleotides under salt conditions necessary for reaction 2 (typically ~12 mM $MgCl_2$). To maximize loading density of oligonucleotides on the gold surface, NaCl is added during reaction 1 to shield the electrostatic repulsion of the oligonucleotides. This method is known as “salt aging” and covers the surface of each AuNPs with tens or even hundreds of oligonucleotides [149].

In reaction 2, the 6-HBs are mixed with functionalized AuNPs for the assembly of waveguide precursors and separated from excess AuNPs as well as aggregates by native agarose gel electrophoresis. The formation of the complexes is analyzed by gel electrophoresis and tSEM imaging. The influence of several parameters on the assembly yield was thoroughly examined by counting correctly and incorrectly assembled structures, see Figure 3.3c.

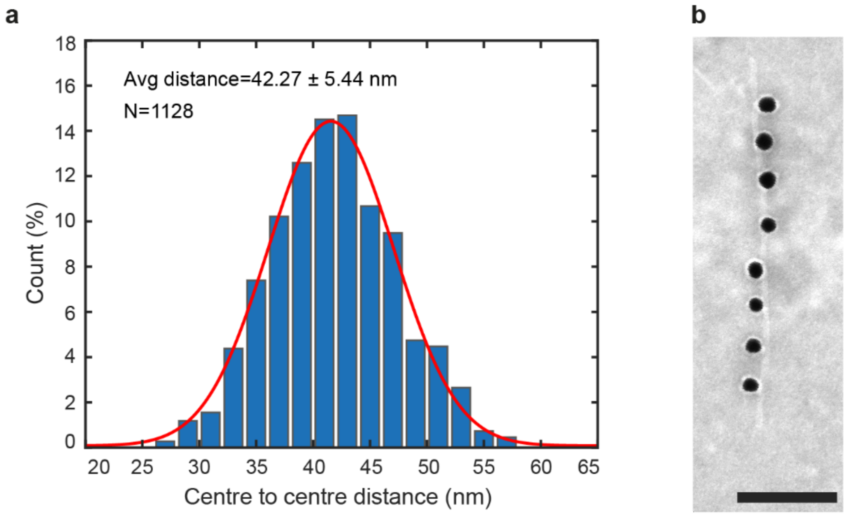

***Figure 3.4 | Center-to-center distance analysis of two neighboring gold nanoparticles in the waveguide precursors.*** *(a) Center-to-center distance distribution plot generated with 17 nm AuNPs attached to 6-HBs. Seven wide field tSEM micrographs were analyzed, only the clusters with eight AuNPs were taken into account. (b) A tSEM micrograph of a typical waveguide precursor. Scale bar, 100 nm.*

After completion of two reactions, the desired assembly of the waveguide precursor, in the ideal case, should be composed of eight particles with designed inter-particle distances. To test the designed and experimental inter-particle distance values and determine the placement accuracy, seven wide-field electron micrographs were evaluated. Figure 3.4 shows statistical analysis of center-to-center distance of two neighboring gold nanoparticles. The center-to-center distance of neighboring AuNPs was measured as an average distance of 42.27 ± 5.44 nm, which is in excellent agreement with theoretical value (0.335 nm/bp · 126 bp = 42.2 nm) [66]. The unoccupied binding sites were observed to be randomly distributed in structures lacking one or more AuNPs, which is in agreement with a previous report [143].

### 3.2.2 Automated image analysis

In order to quickly analyze a large number of tSEM images, an automated counting routine was developed based on MATLAB (see Methods). Briefly, AuNPs are automatically recognized and a boundary with a defined radius is drawn around each AuNP (Figure 3.5a). If two or more of these boundaries intersect, the algorithm considers the particles part of the same cluster. Finally, the number of particles for each cluster is reported. This way, a potential counting bias by experimentalists is avoided, see Figure 3.5b-c. With a given set of parameters such as thresholds and boundary sizes, the algorithm will process each SEM image the same way. The algorithm could also in principle be modified to recognize the number of waveguide precursors in multimers. However, the focus here was to determine the relative influence of various reaction parameters on the assembly yield and not the absolute yield.

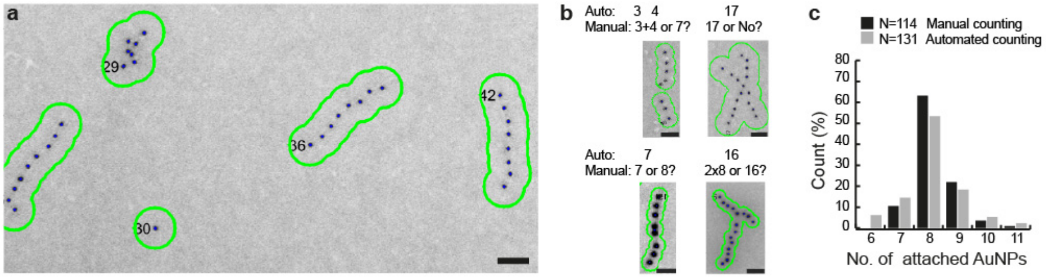

***Figure 3.5 | Automated counting of the waveguide precursors.*** *(a) An exemplary cropped tSEM image from a non-optimized assembly. The MATLAB algorithm automatically detects AuNPs due to their high image contrast and defines "clusters" where nanoparticles are within a radius of 45 nm (green outline). Scale bar, 100 nm. (b) The difference between automated and manual counting by the experimentalist. The scale bars are 100 nm. (c) A comparison of automated and manual counting.*

### 3.2.3 Functionalization and attachment of gold nanoparticles

**Oligonucleotide functionalization of gold nanoparticles**

In the first set of experiments, to optimize the assembly yields, the AuNPs were functionalized with oligonucleotides (reaction 1) at NaCl concentrations ranging from 0 to 1000 mM NaCl, excess oligonucleotides were removed, and the AuNPs were mixed with 6 HBs (reaction 2). First, the reactions were analyzed by native agarose gel electrophoresis. The fluorescent gel image (visualizing the DNA) and the real-color photograph (detection of the AuNPs scattering) reveal that correctly assembled waveguide precursor bands have a lower electrophoretic mobility than the free 6-HBs or free AuNPs (Figure 3.6a). Below 50 mM NaCl or without any NaCl in reaction 1, aggregates containing nanoparticles and 6-HBs produce a blue band just beneath the loading pocket (real-color photograph), while non-aggregated AuNPs or waveguide precursors appear red. The band of the excess AuNPs at 25 mM NaCl is not sharp and has a dark blue tone indicating the formation of AuNP aggregates. The waveguide precursor bands were extracted from the gel and imaged by tSEM. The tSEM images of the 25 mM NaCl waveguide band confirm that both monomeric and oligomeric AuNPs bind to the waveguide precursors. When increasing the NaCl concentration during Reaction 1, correctly assembled waveguide precursors were obtained.

The gel and tSEM images suggest the mechanism of the aggregation: AuNPs carry some oligonucleotides which allow them to bind to the 6-HBs in all cases, even when not salt aged. Otherwise, the band of unmodified 6-HBs would still be visible in the gel. Instead, the 6-HBs are part of the aggregate band as confirmed by tSEM. The AuNPs, however, do not carry sufficient oligonucleotides to effectively prevent them from aggregation when exposed to the folding buffer containing $MgCl_2$ in reaction 2. As a result, the AuNPs come in close proximity (less than few nm) and the plasmon absorption maximum is shifted to the red resulting in a blue aggregate.

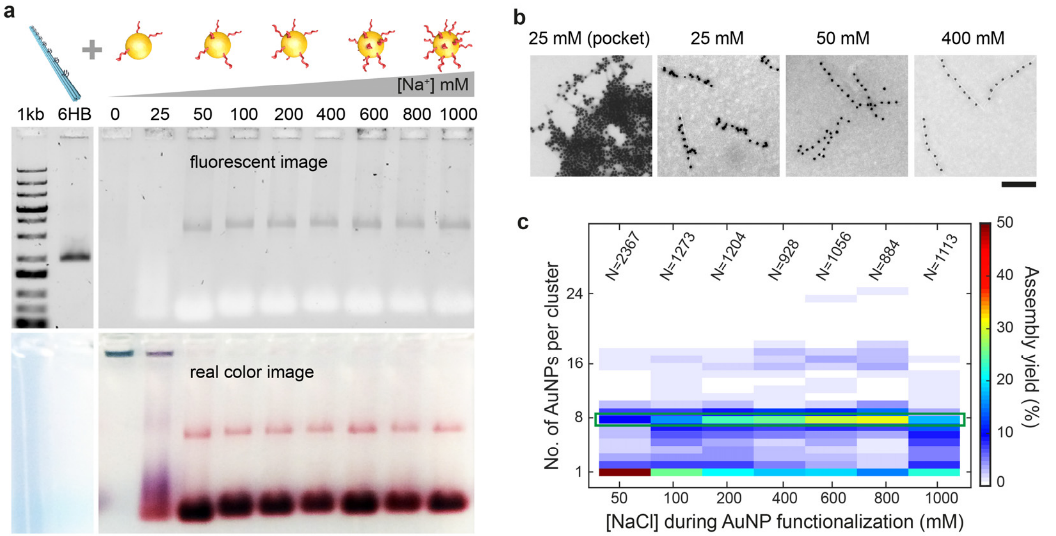

***Figure 3.6 | Effect of salt aging during the functionalization of gold nanoparticles.*** *(a) Agarose gel electrophoresis of the assembly reaction (reaction 2) of 6-HBs with AuNPs functionalized at different NaCl concentrations (reaction 1). Top: Fluorescence image obtained with Sybr safe DNA stain and the real colour photograph of the same gel (bottom). (b) tSEM micrographs of gel-purified waveguide precursors with AuNPs functionalized at 25, 50 and 400 mM NaCl concentrations. The scale bar is 200 nm. (c) Color map distribution of the number of AuNPs per cluster as a function of NaCl concentration during AuNP functionalization. N is the number of automatically counted clusters for the statistical analysis.*

From the tSEM images of the gel-purified waveguide precursors, the number of AuNPs per structure as a function of the NaCl concentration in reaction 1 is determined (see Figure 3.6c). No automated analysis was possible below 50 mM NaCl due to the high degree of AuNP aggregation. At 50 mM NaCl, more than 50% of the "clusters" are unbound free AuNPs and the assembly yield for the correct structure (eight particles) increases upon increasing the NaCl concentration. Two explanations for the free AuNPs were hypothesized. Some oligomeric AuNPs may have been hybridized to the 6-HBs just as in the tSEM image at 25 mM NaCl and these unspecific aggregates were partly dissolved during the workup giving rise to the one-particle "clusters". Alternatively, monomeric AuNPs were less tightly bound to the 6-HBs at lower NaCl salt aging concentrations. This hypothesis is supported by the decreasing percentage of incomplete waveguide precursors containing seven or fewer AuNPs upon increasing NaCl concentrations. Therefore, it is concluded that a salt aging step with at least ~500 mM NaCl is required.

### Attachment of gold nanoparticles to DNA origami

In the second set of experiments, the salt concentration effect on the assembly reaction of the waveguide precursors was studied (reaction 2). Two final $MgCl_2$ concentrations were tested (2 mM and 12 mM) with or without additional 300 mM NaCl (final concentration). The rationale for adding NaCl was to decrease the potential influence of unspecific $Mg^{2+}$-bridges between highly charged species (6 HBs and functionalized AuNPs) [150]; reduced $MgCl_2$ concentrations, on the other hand, may enable nanomedical applications [151]. After agarose gel purification of the waveguide precursors, again, several hundred structures were automatically counted from wide-field tSEM images. Figure 3.7 shows the percentage of clusters carrying 1 to 25 particles.

Although 6-HBs were visible in the tSEM images, the particle attachment yield was very low at 2 mM final $MgCl_2$ (Figure 3.7a). More than 70% of the “clusters” were unbound, single particles. This may have three reasons. First, the weakened hybridization strength of the linker itself was not sufficient to overcome the electrostatic repulsion of the negatively charged origami structures and the functionalized AuNPs. Second, the integration of the extended staple strands at the binding sites into the 6-HBs (the binding to the scaffold strand) was weakened too much under low-salt conditions such that they were disconnected from the scaffold strand. Third, the gold-thiol bond itself may have been weakened by the buffer exchange. In this case, released ssDNA strands could block binding sites on the 6-HBs.

Supplementing the reaction with either additional NaCl (Figure 3.7b) or increasing the $MgCl_2$ concentration to the standard value of 12 mM, improved the assembly yield substantially. A mixture of 12 mM $MgCl_2$ and 300 mM NaCl further improved the yield of waveguide precursors to more than 30%, see Figure 3.7d. The highest yield was achieved when combining dithiol-oligonucleotides with both salts, see Figure 3.7e.

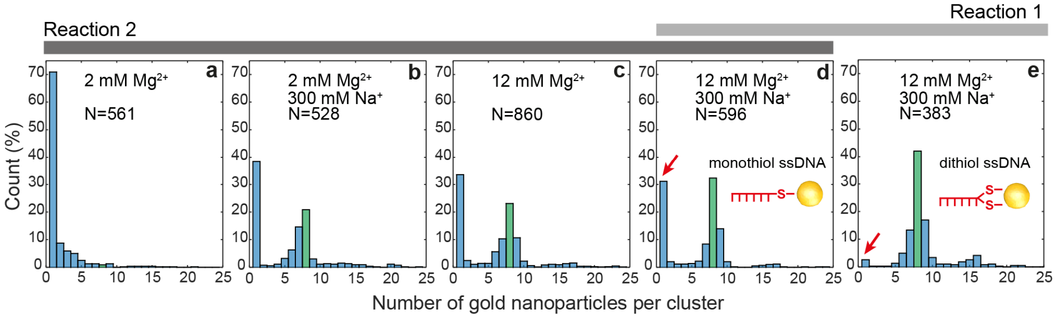

***Figure 3.7 | Assembly reaction 2 and the influence of the thiol linkers.*** *Number of AuNPs per clusters at different salt concentrations during the waveguide precursor assembly reaction (reaction 2, a-d) and comparison of thiol-modified oligonucleotides (d) with dithiol-modified oligonucleotides (e) in reaction 1. The green bars indicate eight AuNPs (correct number of AuNPs attached). The red arrows indicate one particle clusters.*

In the experiments described here, 15 A-T base pairs connect the AuNPs and the 6-HB. This interaction is expected to be stable at room temperature and 12 mM $MgCl_2$, particularly when considering the cooperative effect of the three tethers per binding site. It could be hypothesized that the instability of the gold-thiol bond may explain the remaining one-particle "clusters" (Figure 3.7d) which were also observed by other groups [75], [109], [143], [152]. Therefore, two assembly reactions of AuNPs bound to either monothiol or dithiol-modified oligonucleotides under identical conditions were compared (Figure 3.7d-e). With a dithiol-modification, a 10-fold decrease of unbound AuNPs was observed and the assembly yield of waveguide precursors was improved to around 42%. This is in agreement with a report by Sharma *et al.*, where a dithiol-modified oligonucleotide bound better to a AuNP than a monothiol-oligonucleotide [153]. In that study, however, only one oligonucleotide was attached per AuNP and purified by gel electrophoresis (similar to the original approach by Alivisatios *et al.*) [142], whereas in the case of experiments presented here, an approach by Mirkin *et al.* [134] was aimed for a dense coverage of the Au surface.

### Complexes can contain more than eight gold nanoparticles

The 6-HB design described here has eight AuNP binding sites. Surprisingly, complexes containing nine, ten or even 11 AuNPs were also found. These are attributed to an unforeseen interaction of the functionalized AuNPs with ss scaffold loops in the design connecting adjacent helices at the faces of the 6-HBs and/or the scaffold loop containing the non-consensus (scaffold-specific) sequence. Similar observations were made by Kuzyk et *al.* [75]. Complexes with 9-11 AuNPs could presumably be prevented by redesigning the ends of the 6-HBs and by eliminating or protecting the scaffold-specific loop. For the scope of this study, however, additional unintended interactions were ignored. Only rarely and only for small AuNPs two AuNPs sharing a binding site were observed.

Figure 3.8 shows waveguide structures carrying more than the 8 designed binding sites. This may occur when poly-T-functionalized AuNPs interact cooperatively with poly-A sequences in the unused single-stranded scaffold loops of the 6-HBs. Such loops can be found on both ends of the 6-HBs (Figure 3.8, green loops) or at the side (blue loop).

The loops at the faces of the 6-HBs (green) connect adjacent helices and are often used in DNA origami designs as an entropic brush to prevent unintended aggregation of 6HBs due to blunt-end stacking. The long unused scaffold loop at the side of the 6-HBs (blue) is present as only the consensus sequence of the M13 clones was used. Its length is 841 nt for p8064 and p8064 was used in most experiments shown here. All single-stranded loops can contain a few poly-A sequences. Up to six consecutive A were found in retrospect. Few A-T base pairs alone should not suffice to stably attach a functionalized AuNP at standard conditions (room temperature, 12 mM MgCl2), but several of these interactions can be formed simultaneously with the polyvalent AuNPs.

Apparently, several cooperative interactions are strong enough to stably connect the AuNPs and therefore waveguide precursor structures with 9-11 AuNPs were observed. This was not anticipated in the initial design but does not alter the main message of this study. The unintended attachment could be prevented by redesigning the 6-HBs such that no single-stranded scaffold loops containing poly-A sequences are left. In that case, only the designated binding sites would act as attachment points.

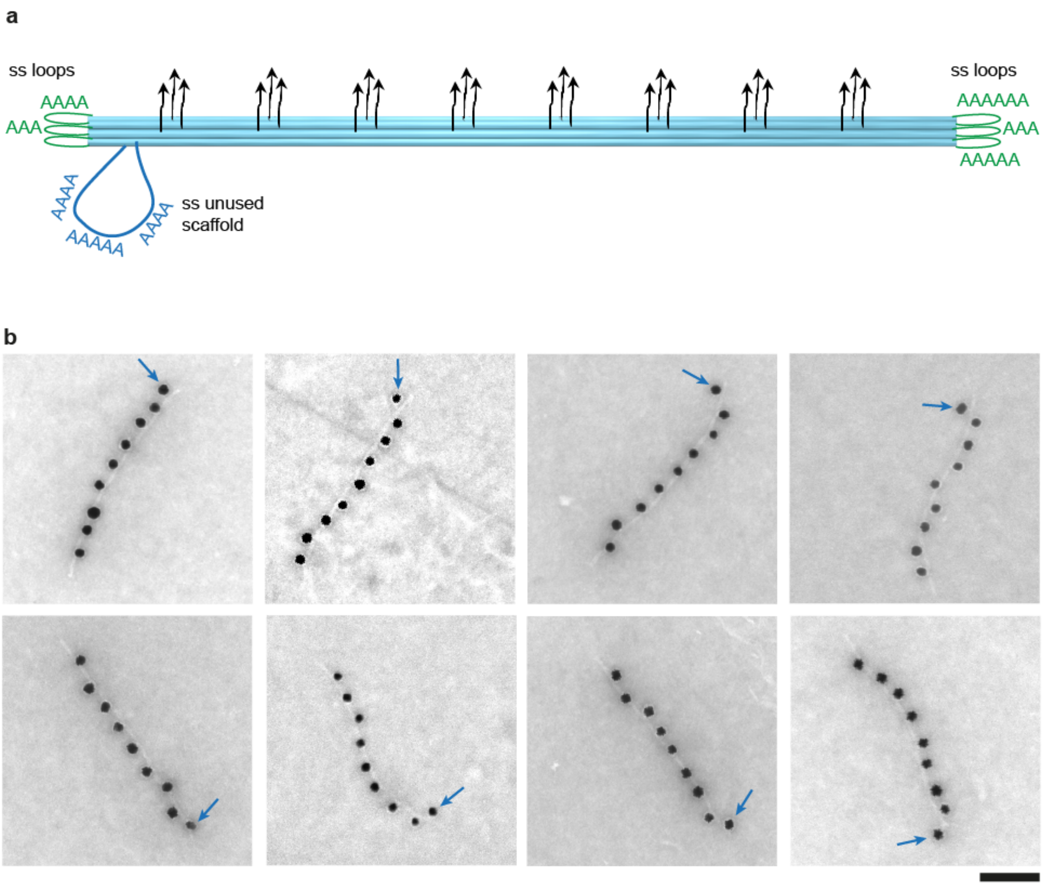

***Figure 3.8 | Complexes can contain more than eight AuNPs.*** *(a) Design of 6-HB with eight binding sites, single-stranded unused scaffold and single-stranded loops between helices can contain poly-A sequences (poly-A sequences in green are contained in the respective loops at the ends). (b) tSEM micrographs of waveguide precursors with nine AuNPs. Blue arrows indicate possible unspecific attachments due to poly-A sequences on the single-stranded unused scaffold or due to poly-A sequences on the single-stranded loops between helices. Scale bar, 100 nm.*

Complexes containing less than eight AuNPs, on the other hand, can form in two ways. Either, the AuNPs detach from the 6-HB after the synthesis, during the workup or during the deposition on the TEM grid or some ssDNA released from the AuNPs block the attachment sites. The latter mechanism is presumably responsible for an increase of single particles when oligonucleotide-modified AuNPs are stored for a longer period of time (days or weeks) before mixing them with the 6-HBs. Therefore, it is crucial to only use freshly modified and purified AuNPs.

### 3.2.4 Assembly kinetics and preventing crosslinking

The polyvalent nature of densely functionalized AuNPs allows crosslinking of multiple binding sites on different DNA origami structures and therefore can induce aggregation. Waveguide precursor design contains eight identical binding sites on the same side of the 6-HB DNA nanotubes and is therefore particularly prone to a cooperative crosslinking between multiple structures. Arranged in other ways, for example as a spiral [75], crosslinking is less likely. To explore the effect of the molar excess of AuNPs over binding sites (each consisting of three ss overhangs) during reaction 2, a 1.25 to a 15-fold molar excess of AuNPs was scanned and reactions were analyzed by native agarose gel electrophoresis, see Figure 3.9. The intensity of the waveguide band is very low at an excess of only 1.25 AuNPs / binding site, increases up to a 7.5-fold excess and remains constant at a higher excess. At a low molar excess of AuNPs, aggregates were observed both in the gel (as a band on the bottom of the loading pocket) and in the tSEM images, see Figure 3.9.

The color of the aggregates here is red and not blue as in Figure 3.6a as the nature of the aggregates is different. Without proper salt aging, the AuNPs themselves aggregated and the surfaces of the AuNPs came into contact leading to a broader plasmon band with a higher absorption in the red spectra. Here, the AuNPs are shielded well by the dense layer of oligonucleotides and the color of these crosslinked aggregates is indistinguishable from monodispersed AuNPs. In both cases, aggregates have a greatly reduced electrophoretic mobility and plasmonic devices would be unusable.

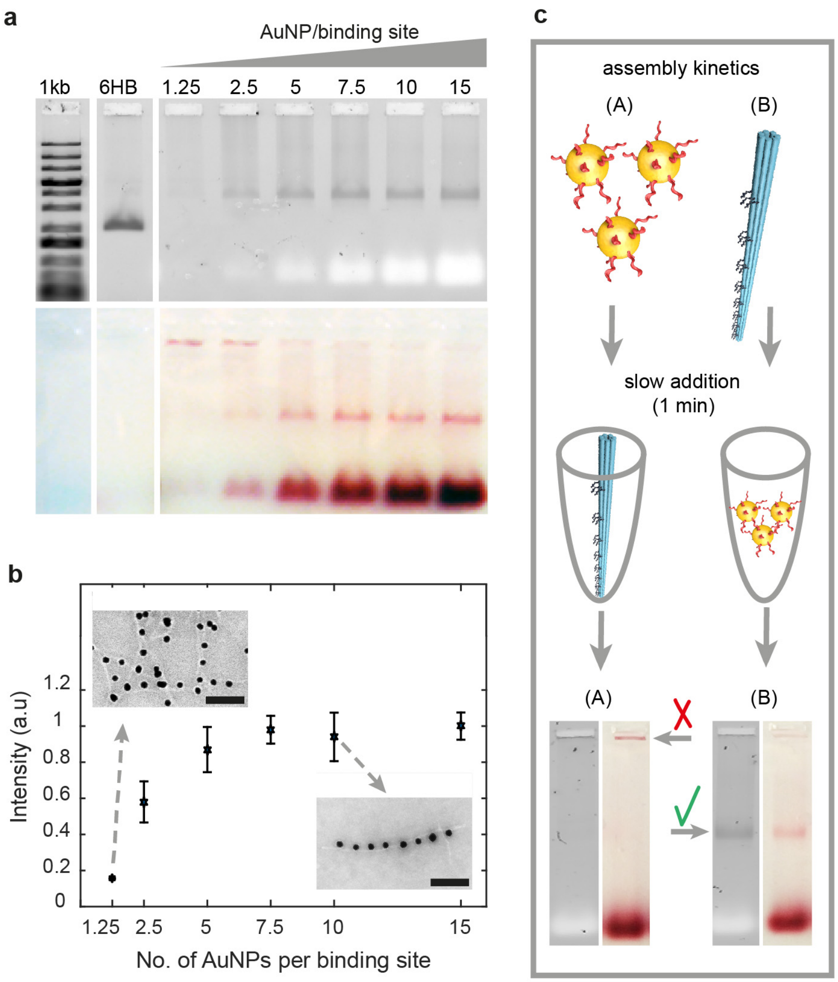

***Figure 3.9 | Effect of the excess of AuNPs per binding site on the waveguide precursor assembly.*** *(a) Agarose gel electrophoresis of the assembly reaction (reaction 2) of 6-HBs with functionalized AuNPs: Fluorescence image (top) and the real color photograph of the same gel (bottom). 1 kb DNA ladder, 6-HBs, and crude assembly reaction mixes with a 1.25 to 15-fold excess of AuNPs per binding site. (b) Fluorescent intensity of the waveguide precursors bands as a function of the excess of AuNPs per binding site. tSEM images of the experiment with a 1.25-fold and 10-fold excess of AuNPs per binding site (scale bars = 100 nm). (c) Assembly reaction (reaction 2) of a 10-fold excess of AuNPs with 6-HBs in different addition orders. (A) 6-HBs are slowly added to AuNPs, (B) reversed addition order.*

Some common protocols call for incubation times of many hours or even a full day for reaction 2 [75], [85], [89], [91]. To explore the assembly kinetics for this hybridization reaction, a 10-fold molar excess of AuNPs was slowly added to a 6-HB solution (see Figure 3.9c) over the course of one minute. In the control experiment, the addition order was reversed and 6-HBs were slowly added to the same excess of AuNPs. In the first case, a strong aggregation was observed, in the second case, a formation of the waveguide precursors. The formation of aggregates in the first case can be explained by the high number of 6-HBs that the first added AuNPs are exposed to. These AuNPs quickly crosslink the large excess of available 6-HBs. This crosslinking could not be undone by the large excess of AuNPs later on, nor by subsequent heating to 45 °C for 25 min and reannealing.

In the other case, where 6-HBs were slowly added to the AuNP solution, 6-HBs were always exposed to a large excess of AuNPs. Therefore, the probability of a AuNP to crosslink two 6-HBs is greatly reduced. A very quick addition and instant mixing did not show substantial differences and mainly proper waveguide precursors were formed.

From this, it is concluded that the assembly reaction takes place within seconds at room temperature and that the reaction is irreversible under conditions where the DNA origami itself is stable. This suggests that the hybridization time can be shortened from many hours to few minutes and that additional annealing ramps for the assembly [143] are unnecessary for designs with comparable linker strengths.

Next, the effect of a number of binding sites on overall assembly yield was investigated. For this, the 6-HBs were designed and folded with two, four, six and eight binding sites. Figure 3.10 shows statistics of the number of attached particles for the corresponding structure shown in tSEM images from the automated image analysis. As expected, the complexes with two binding sites have the highest site occupancy, which is above 80%. The site occupancy is gradually decreasing when the number of binding sites is increasing. One should take into account that the site occupancy and the assembly yield would be much higher if they were evaluated by manual counting.

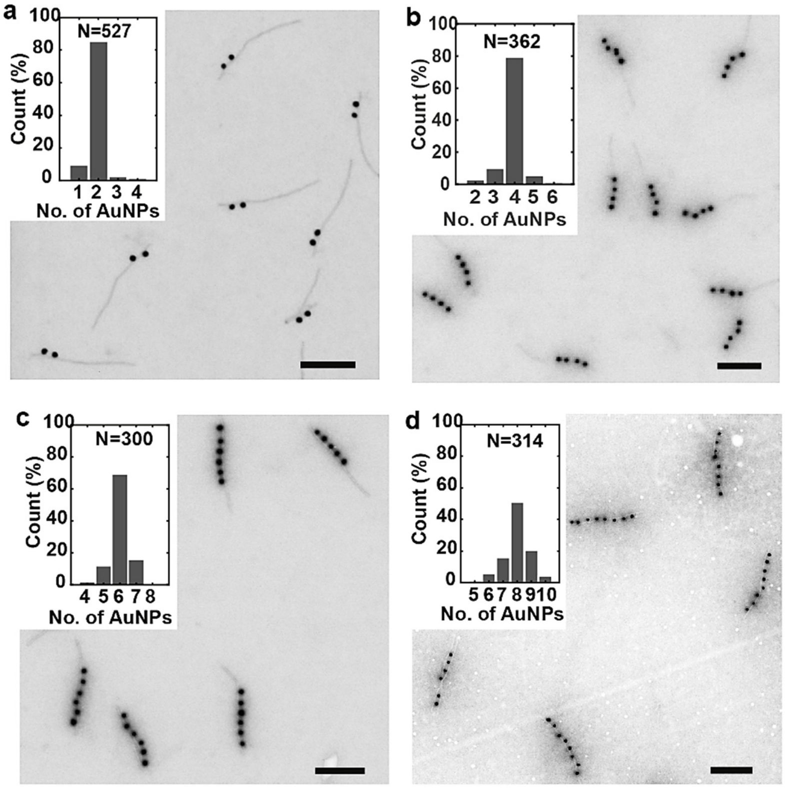

***Figure 3.10 | Number of binding site dependency on assembly yield.*** *Automated image analysis results of complexes with two particles (a), four particles (b), six particles (c) and eight particles. Scale bars, 200 nm.*

### 3.2.5 Site occupancies and assembly yields

It is not easy to define and compare the final assembly yield results presented here and the results of other previous reports where different criteria have been applied [75], [94], [109], [143], [152], [154]. In all cases, AFM or TEM images were evaluated manually and misfolded or nonlinear structures and aggregates were not taken into account. Single AuNPs were visible in many studies, but they were ignored in all those reports. However, it is likely that these unconnected AuNPs must have detached from the structures after purification and are a good measure for the strength of the attachment chemistry and assembly conditions. It should be stressed that here in this study the wide-field images with more than ~30 waveguide precursors were exclusively evaluated. This eliminates the risk of unconsciously selecting regions where intact structures are enriched.

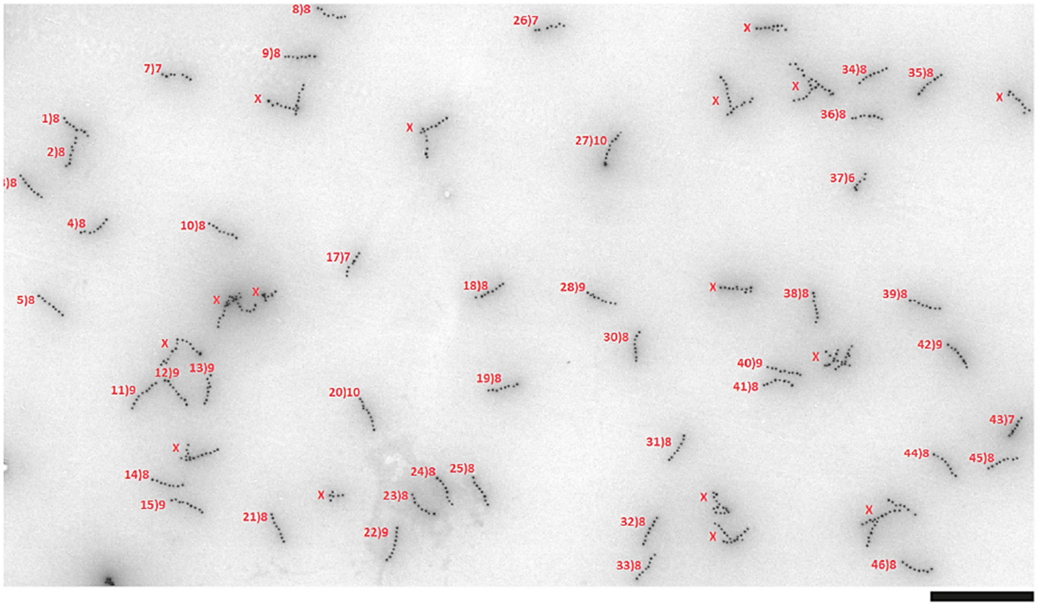

***Figure 3.11 | Manual counting result of purified waveguide precursors from the wide-field tSEM micrograph.*** *Scale bar, 1 µm.*

In addition to the standard automated counting and to allow a comparison with previous reports, three images (one of them depicted in Figure 3.11) from the experiment in Figure 3.7e were evaluated, according to the criteria above, i.e. incomplete, nonlinear, cross-linked, and twisted structures were excluded, and clusters containing more than eight AuNPs were counted as eight AuNPs/cluster [75]. It was found that 98.7% of the designed binding sites were occupied by AuNPs and that 89.5% of the structures had all eight AuNPs binding sites occupied (N=114). These are the highest numbers reported so far for multi-particle systems (above five particles). The binding occupancy would gradually approach 100% when the number of binding site decreases from eight to one (see Figure 3.10). The site occupancy could potentially be further increased when smaller AuNPs are attached [94], [137], small AuNPs (~5 nm) with less number of binding site are employed [110] or more than three ss DNA extensions are used for one binding site [143].

## 3.3 Attachment of larger gold nanoparticles

The AuNPs with a diameter of ~17 nm were used in all the experimental results presented so far. These AuNPs with a narrow size distribution are reasonably inexpensive and easy to synthesize. However, to facilitate strong plasmon coupling, AuNPs with the diameter above a few 10 nm might be necessary.

The quality of commercially available AuNPs is usually not good, the size distribution is broad especially for large AuNPs (see Figure A.1 in Appendix) and their surface ligands and the buffer conditions are often unknown. For these reasons, AuNPs with a diameter of ~28 nm and ~56 nm were synthesized by a two-step seeded growth process using hydroquinone as a reducing agent [155].

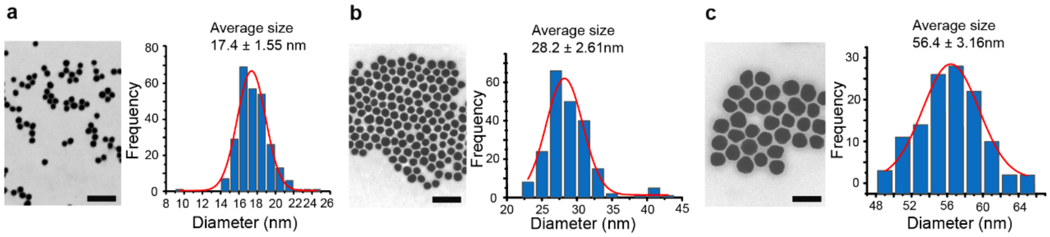

***Figure 3.12 | Characterization of gold nanoparticles with different diameters****. tSEM micrographs of AuNPs with ~17 nm (a), ~28 nm (b) and ~56 (c) nm in diameter and size distribution analysis of the corresponding AuNPs determined from the tSEM micrographs. Scale bars, 100 nm.*

The particles were characterized by the tSEM and electron micrographs revealed that the particles were highly monodispersed and spherical. The size distribution analysis shows that mean size of the AuNPs are 17.4 nm ±1.55 nm, 28.2 nm ±2.61 nm, and 56.4 nm ± 3.16nm, see Figure 3.12.

To test if the optimized parameters can be applied for the attachment of larger AuNPs, they were functionalized with thiolated oligonucleotides, salt aged and mixed with 6-HBs at an excess of 10 AuNPs per binding site. For the 28 nm AuNPs, the same 6-HB design was used as described above with eight binding sites with a center-to-center distance of 42.2 nm. For the 56 nm AuNPs, only every second binding site was incorporated in the 6-HB design reducing the number of binding sites to four with a distance of 84.4 nm.

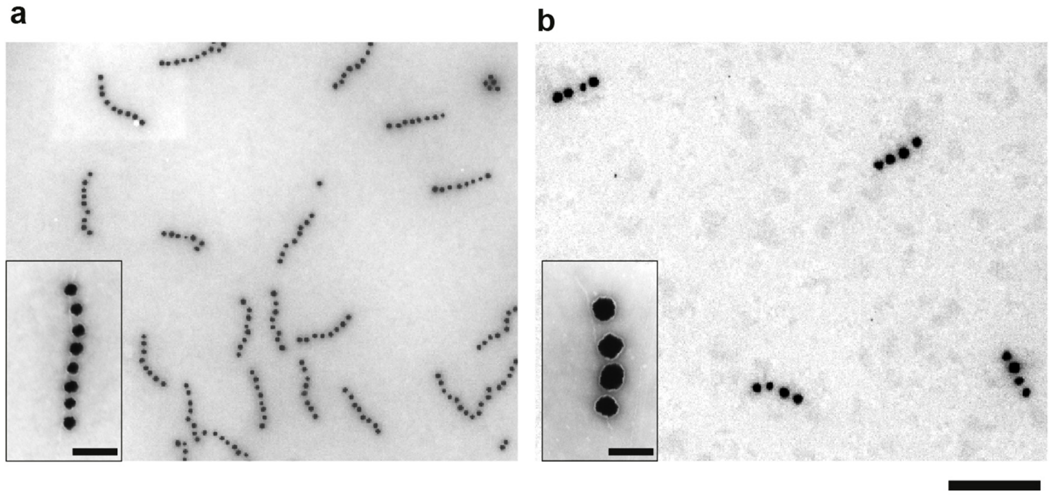

***Figure 3.13 | Attachment of larger gold nanoparticles to the six-helix bundles.*** *tSEM micrographs of (a) 8 x 28 nm AuNP and (b) 4 x 56 nm AuNP waveguide structures. Scale bar, 500 nm, and inset scale bars, 100 nm.*

The tSEM images in Figure 3.13 show mostly well-assembled structures suggesting that the optimized protocols work for the attachment of 17-60 nm (and potentially larger) AuNPs to DNA origami. These results also imply that the local flexibility of the 6-HBs and the tethers is not high enough to allow binding of two or more binding sites of one 6-HB to one AuNP.

## 3.4 Attachment of quantum dots

In order to test the function of the waveguides with the optical fluorescent microscope, a donor quantum dot (Qdot 525), a yellow-green, and an acceptor Qdot (625), red, were attached to the waveguide. For this, in addition to the binding sites for the attachment of AuNPs (from BS 1 to BS 8), the 6-HBs with containing two orthogonal binding sites (BS 0 and BS 9) that are located in the terminal positions were designed, as depicted in Figure 3.14a.

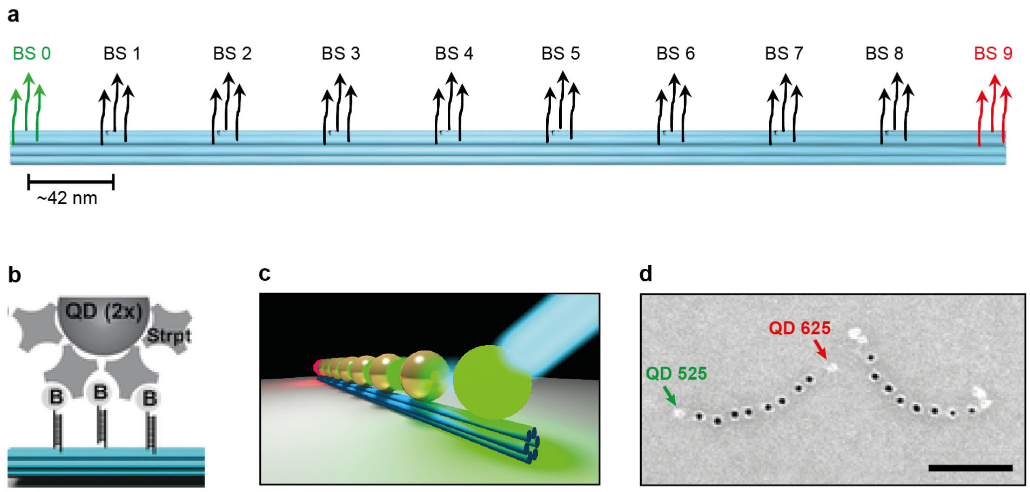

***Figure 3.14* | *Quantum dot attachment to the waveguides.*** *(a) 6-HB design with orthogonal binding sites for the attachment of two different Qdots as well as AuNPs, ss loops and unused ss scaffold are not shown for clarity. (b) Schematic illustration of biotin-modified oligonucleotides functionalized Qdot, binding to the designated position on the 6-HB. (c) Artistic representation of the waveguide excitation and emission. (d) tSEM micrograph of the waveguides with two type of quantum dots attached at the terminal positions, scale bar, 200 nm. Panel (b) reproduced from the reference [156], and panel (c) courtesy of Dr. Diana Goncalves Schmidt.*

The donor Qdot can be used as a nanoscale light source for the local excitation of surface plasmons on the first AuNP and the acceptor Qdot can be used as a reporter particle which emits to the far field after the propagating surface plasmons couple to it. Here, it is important that the emission of the donor Qdot should match the resonance frequency of the single AuNP and the excitation of the acceptor Qdot should match the coupled plasmonic modes of the waveguide. Moreover, donor and acceptor Qdots spectrum should not overlap, because far-field excitation by the microscope should excite only the donor Qdot. Therefore, the choice of the Qdot pair is quite important in this experiment.

Commercially available Qdots with streptavidin conjugates were functionalized with biotin-modified orthogonal oligonucleotides for donor and acceptor Qdots. After removing excess biotin modified oligonucleotides, Qdots were first mixed with 6-HBs and then ~17 nm functionalized AuNPs were added to the solution. The whole assembly including AuNPs and two type of Qdots was purified by gel electrophoresis.

The attachments of donor and acceptor Qdots to the waveguides were successfully realized by tSEM imaging (see Figure 3.14d). However, electron micrographs indicated that the attachment yield was not as high as the attachment yield of the AuNPs. Moreover, since the core of the Qdots is relatively small (~5 nm), it was quite difficult to visualize them by the electron microscope. From this, it was hypothesized that the attachment yield was actually better, and that they were often just invisible in the final images. In addition, other types of Qdots (Qdot 565 streptavidin conjugate and Qdot 705 streptavidin conjugate) were also tested and larger AuNPs (see Figure A.2 in Appendix) and obtained similar attachment results.

For the optical measurements (in collaboration with Dr. Friedrich Schwarz / Diez lab), it was aimed to determine the mean on-intensity of the individual Qdots and analyze the variation of intensity as a function of laser excitation intensity as a baseline. In order to localize the intact waveguides, the experiments were performed by total internal reflection fluorescence (TIRF) microscope based on parabolic shaped quartz prism approach [157] that allows for the detection of Qdots emission as well as scattering properties of the waveguide. Unfortunately, these experimental measurements were not successful for the following reasons. First, binding of the waveguides to the glass slide was not optimal, the streptavidin on the glass slide and the biotin on the 6-HBs were not efficiently bound. Second, since the measurements were done in solution, significant background scattering signal from biotin, BSA, or impurities was observed. Therefore, the scattering signal from the waveguides could not be identified. Third, inhomogeneous illumination of the TIRF set-up gave rise to different emission intensities of Qdots. For those reasons, conclusive results were not obtained from these experiments and this approach was not pursued further. Instead, electron energy loss (chapter 4) and cathodoluminescence imaging (chapter 5) spectroscopies were studied.

## 3.5 Multimerization of the waveguides

The maximum length of the waveguides is limited by the length of the DNA origami structure that are used to assemble the waveguides. The 6-HB DNA origami structure is ~400 nm long as it is limited by the size of the scaffold which is used for the DNA origami folding (an M13 clone, 7249 nt). Here, it was further advanced for a synthesis of longer waveguides (up to 1.2 micron) with a length control. For this, the monomer 6-HBs were employed and interconnected by introducing interfaces at the ss loop of the monomers. As shown in Figure 3.15a,b, three monomer 6-HBs (A, B, C) were designed by introducing additional staple strands for blocking the left and right sites (left side of the monomer A, AL and right side of the monomer C, CR) and interconnecting A-to-B-to-C with 5 nt extensions from the B which is complementary to the missing part of A and C in the ss loops. The 6-HB monomers (A, B and C) were folded separately with respective staple strands and purified by PEG precipitation. Afterwards, monomers were mixed at 1:1:1 molar ratio and incubated at room temperature.

Agarose gel electrophoresis and tSEM imaging confirmed the formation of trimer 6-HBs, see Figure 3.15c, d. Two bands were observed in the lane labeled ABC, one representing trimer 6-HBs and the band below representing monomer 6-HBs. Monomer 6-HBs might still be present in the sample because the amount of each monomer could be unequal due to the pipetting or concentration measurement errors. The aggregates in the gel pocket of ABC lane were observed which may come from unspecific blunt-end stacking. This can be eliminated by redesigning staple strands in the end loops (AL and CR), simply by extending them by a few random nucleotides.

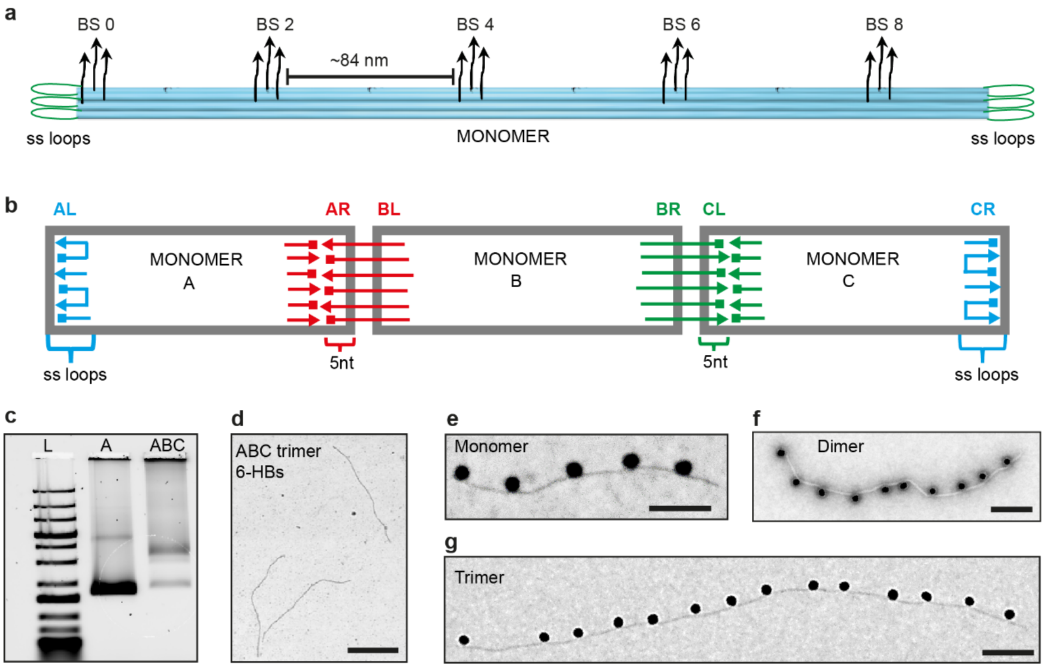

***Figure 3.15 | Multimerization of the waveguides.*** *(a) Schematic illustration of the 6-HB design with every second binding site for the attachment of AuNPs. (b) The interface design of the 6-HB for multimerization of monomers. (c) Agarose gel electrophoresis image, showing 1 kb ladder (L), monomer 6-HBs (A) and trimer 6-HBs (ABC) bands. (d) tSEM micrograph of the trimer 6-HBs, scale bar 500 nm. tSEM micrographs of the (e) monomer, (f) dimer and (g) trimer waveguides, scale bars 100 nm.*

To test the working principle, the monomer waveguides with functionalized AuNPs with a diameter of ~17 nm with the standard protocol. A, B and C monomer waveguides were mixed at a molar ratio of 1:1:1 and incubated them at room temperature. Electron micrographs revealed that monomer, dimer, and trimer waveguides were correctly assembled. As the number of binding sites was increased to 15 for the trimer waveguides, the probability for waveguides with all sites occupied is decreased. The trimer waveguide assembly with larger AuNPs was also tested and similar assembly results were achieved (see Figure A.3 in Appendix).

In another approach, AuNPs were directly attached to the agarose gel electrophoresis purified trimer 6-HBs and assembled trimer waveguides were purified again by a second agarose gel electrophoresis. In this case, the population of trimer waveguides was higher. In this case, the population of trimer waveguides was higher. However, since the number of binding sites is relatively higher in trimer 6-HBs, ensuring a 10-fold excess of AuNPs might be challenging if the molar concentration of trimer 6-HBs is kept the same as the molar concentration of monomer 6-HBs. Because reaching very high stock concentration is critical especially for the big (above 20 nm) size AuNPs.

## 3.6 Concluding remarks

In this chapter, a set of parameters that affect the attachment yield of oligonucleotide-functionalized AuNPs to 6-HB DNA origami nanotubes were investigated. To compare the optimized experimental results presented this chapter according to criteria of previous reports [75], [109], [110], [143], complexes in the wide-field tSEM micrographs were manually counted. The site occupancy of 98.7% and 89.5% of intact waveguides, where all binding sites were occupied, were achieved. As an outcome of this comprehensive study, the following set of optimized rules were identified to achieve the unprecedented synthesis yields for multi-gold nanoparticles (above five) attachment to the DNA origami.

The first optimized parameter is the salt aging during the functionalization of AuNPs to prevent aggregation of the AuNPs and to ensure strong hybridization. Particles should be salt aged with at least ~500 mM NaCl. Second, AuNPs modified with dithiol-modified oligonucleotides can be bound more stably to DNA structures than AuNPs with monothiolated oligonucleotides. Third, a high ionic strength is necessary to stably hybridize the AuNPs to the tethers on the origami. The addition of 300 mM NaCl to the standard 12 mM $MgCl_2$ increases the binding efficiency. Low ionic strength buffers, where the DNA origami structures themselves are stable, do not suffice to stabilize assembled AuNP-origami complexes. Forth, at least a 7.5-fold molar excess of AuNPs should be used per binding site to avoid cross-linking of different origami structures. Fifth, the hybridization of the AuNPs only takes seconds. Therefore, mixing should be performed rapidly or DNA origami should be added slowly to the solution containing the AuNPs to avoid the formation of aggregates crosslinked by multivalent AuNPs.

Sixth, aggregates cannot be dissolved by additional annealing steps. Crosslinking of neighboring binding sites by on AuNP was rarely observed even though hybridization was performed at room temperature. Increased incubation times of many hours or additional annealing steps do not seem necessary. Seventh, freshly functionalized and purified AuNPs should be used for the assembly.

The set of optimized parameters can be reliably used to attach AuNPs with a diameter up to 56 nm, which is necessary to enhance plasmonic effects and to produce functional devices. This systematic study will, therefore, help to improve yield and reliability of DNA-based plasmonic devices for applications in photonics, optoelectronics or nanomedicine. In addition, multi-components attachment to 6-HBs was demonstrated by employing functionalized Qdots with orthogonal oligonucleotides. Furthermore, 6-HBs interface design for the multimerization of the waveguides was developed. With this, producing longer waveguides up to 1.2 micron length was demonstrated. These results indicate that DNA origami is an extremely versatile and robust method for construction of complex, multi-component, functional and hybrid plasmonic systems.

## 3.7 Materials and Methods

**Synthesis of gold nanoparticles.** AuNPs with a diameter of ~17 nm were synthesized by the reduction of tetrachloroauric acid ($HAuCl_4$) (Sigma Aldrich) based on a one-step method [148] with trisodium citrate (Applichem) as a reducing agent. Before the synthesis, all glassware was cleaned with aqua regia (2 vol. of concentrated hydrochloric acid and 1 vol. of concentrated nitric acid) and carefully rinsed with copious amounts of water. 50 mL of a solution of 0.25 mM tetrachloroauric acid were brought to a rolling boil in an Erlenmeyer flask. Under vigorous stirring, 1.5 mL of freshly prepared 34 mM (1% w/v) sodium citrate solution was added very quickly. After the colour had changed from pale to grey to red, the solution was refluxed for another 30 min. The colloidal nanoparticle solution was filtered through a syringe filter (VWR) with a pore size of 0.2 µm.

For ~28 and ~56 nm AuNP synthesis, the ~17 nm AuNPs were used as seeds. The protocol based on hydroquinone reduction [155] was used by adjusting the number of seeds to achieve the ~28 and ~56 nm AuNPs. The particles were synthesized in 50 mL batches. Hydroquinone (Alfa Aesar) and sodium citrate solutions were freshly prepared. The Gold chloride solution was centrifuged at 17,000 rcf for 60 min before synthesis to remove any aggregates. For both syntheses, 500 µL of a 1% (w/v) $HAuCl_4$ solution was added to 34-47 mL of ultra-pure water (depending on the seed volume; final volume = 50 mL) in a 250 mL Erlenmeyer flask. For the ~28 nm AuNP synthesis, 15 mL of 3.2 nM 17 nm seeds, for the ~56 nm AuNP synthesis 1.6 mL of the seeds were added. The solution was vigorously stirred at room temperature. 110 µL of a 1% sodium citrate solution was then added, immediately followed by 500 µL of 0.03 M hydroquinone. The colour change of the solution occurred immediately after the addition of hydroquinone and the reaction was stirred for another hour. Finally, the colloidal nanoparticle solution was filtered through a syringe filter (VWR) with a pore size of 0.2 µm.

A drop of colloidal gold solution was placed on a carbon-coated formvar TEM copper grid (Science Services), incubated for 5 min and washed with a drop of water. The AuNPs were characterized by SEM/tSEM (FEI, Helios 660) with a 15 kV acceleration voltage. The size distribution of particles was measured from wide-field tSEM micrographs by using an image processing and analysis program (ImageJ).

**Functionalization of gold nanoparticles.** Next, the citrate shell was exchanged for a more stable phosphine ligand for the concentration of the AuNPs [75]. For this, 20 mg Bis(p-sulfonatophenyl) phenylphosphine dihydrate dipotassium salt (BSPP, Sigma-Aldrich) were added to 50 mL of the colloidal AuNP solution and were shaken overnight. An aqueous 5M NaCl solution was added dropwise until a colour change from red to dark blue was observed. The solution was then centrifuged for 30 min at 1,600 rcf, the supernatant was removed, and the particles were resuspended in 1 mL of an aqueous 2.5 mM BSPP solution and an equal volume (1 mL) of methanol. The sample was centrifuged once more (1,600 rcf, 30 min), the supernatant was carefully removed, and the AuNPs were once more resuspended in 1 mL of a 2.5 mM BSPP solution. The concentration was determined photometrically at 524 nm assuming a molar extinction coefficient for 17.4 nm AuNP of $2.4 \times 10^8$ $L*mol^{-1}*cm^{-1}$ as in ref. [149] The concentrations of ~28 nm and ~56 nm AuNPs were calculated from the number of the 17 nm seed particles.

Next, AuNPs were conjugated to thiol-modified oligonucleotides (5'-ThioMC6-T19) or dithiol-modified oligonucleotides (5'-DTPA/T19 (Integrated DNA Technologies)). First, the thiol-modified oligonucleotides were incubated with TCEP (Tris(2-carboxyethyl)phosphine hydrochloride), Sigma-Aldrich; 20 mM final concentration) for 45 min. Then, AuNPs and the thiol-modified oligonucleotides were mixed in 0.5X TBE (Tris base, boric acid, EDTA, pH = 8.0) buffer at a ratio of 1:300 (AuNP:DNA) for 17 nm AuNPs, 1:750 for 28 nm AuNPs and 1:2000 for 56 nm AuNPs.

Salt aging was performed to maximize the oligonucleotide density on the AuNPs. Depending on the final NaCl concentration (0-1000 mM), the addition steps varied. For 25 mM and 50 mM final NaCl, the NaCl solution was added once. For a final concentration of 100 mM or above, extra NaCl solution was added 2-7 times to achieve 50, 100, 200, 400, 600, 800 and 1000 mM final NaCl. After each stepwise addition of NaCl, the sample was sonicated for 10 sec and incubated for 20 min. After the last NaCl addition, the mixture of AuNPs and oligonucleotides was incubated for 1 day at 25 rpm and room temperature in a rotator. The excess of oligonucleotides was removed by five ultrafiltration and washing steps (400 µL of 0.5X TBE buffer) with a pre-wetted 100 kDa molecular weight cut-off filter (MWCO, Amicon Ultra, AMD Millipore) at 10 000 rcf for 5 min just before hybridization to 6-HBs to avoid blocking of binding sites on 6-HBs by free oligonucleotides.

**Folding of six-helix bundles.** Selected staple strands were extended with poly-A linkers on their 3' end on 3 adjacent helices to bind to poly-T-functionalized AuNPs. Each binding site is composed of 3 overhangs (5'-A15). To form the 6-HBs, 10 nM of p8064 scaffold, 170 short staple strands (IDT, depending on the binding site design with or without poly-A extension) at 100 nM (each), 5 mM Tris (Applichem), 1 mM EDTA (Applichem) (pH 8) and 12 mM $MgCl_2$ (Applichem) were mixed. The mixture was annealed from 80 °C to 65 °C at a rate of 1 °C per min and from 65 °C to room temperature at a rate of 1 °C per 20 min. Excess staple strands were removed by ultrafiltration (100 kDa cut-off, Millipore) and washing five times with 400 µL 1X TE containing 12 mM $MgCl_2$ at 10,000 rcf for 5 min.

**Waveguide assembly and gel purification.** The purified 6-HB solution (2 nM final concentration for ~17 nm AuNP attachment, 1 nM for ~28 nm and ~56 nm AuNP attachment) was quickly mixed with functionalized AuNPs (10 AuNPs / binding site) in 1X TE containing 12 mM $MgCl_2$ and 300 mM NaCl unless specified otherwise and incubated for 90 min at room temperature. For purification of the assembled waveguides from excess AuNPs and aggregates, a 0.75% agarose gel (Roche) was cast with 0.5X TBE buffer containing 12 mM $MgCl_2$ and stained with Sybr safe DNA gel stain (Life technologies). 0.5X TBE buffer with 12 mM $MgCl_2$ was used as a running buffer. All samples were mixed with a 20% volume of gel loading dye (50% glycerol, 5 mM Tris, 1 mM EDTA, 0.25% bromophenyl blue). Electrophoresis was performed in a fridge at 4 °C at 85 V for 2.5 h. As a reference, a 1 kb DNA ladder (Thermo Scientific) and 6-HBs were used. The selected bands were cut out and chopped into small pieces. The waveguide precursors were extracted from the gel with Freeze 'N Squeeze spin columns (Bio-Rad) by centrifugation at 5,000 rcf for 10 min. The waveguide precursors formed a pellet at the bottom of the tube. The supernatant was discarded and the pellet was resuspended in 1X TE containing 12 mM $MgCl_2$ buffer to the desired concentration.

**Quantum dot attachment to the waveguides.** For quantum dot attachment experiments, 6-HBs containing two binding sites that are located in the terminal positions (BS 0 with 5'-GAAGAAGAAGAAGAAGAA and BS 9 with 5'-GTGTGTGTGTGTGTGTGT extensions) for attachment of two different quantum dots and eight binding sites (from BS 1 to BS 8 with 5'-A15 extensions) for attachment of AuNPs, were folded and purified as described above. Qdot 525 streptavidin conjugate and Qdot 625 streptavidin conjugate (Thermo-Fisher Scientific) were functionalized with biotin modified 5'-BIO TTCTTCTTCTTCTTCTTC and 5'-BIO ACACACACAC ACACACAC (Eurofins), respectively. Qdots were mixed with biotin-modified oligonucleotides at 1:400 (Qdot:DNA) ratio in Qdot incubation buffer, (2% BSA in 50 mM borate, pH: 8.3 with 0.05% sodium azide, Thermo-Fisher Scientific). The solution was incubated overnight for the biotin attachment to the streptavidin in a thermo-shaker at room temperature. After that excess biotin-modified oligonucleotides were removed by ultrafiltration (100 kDa cut-off, Millipore) and washed eight times with 400 µL 1X phosphate buffered saline (PBS at pH 7.4) at 10,000 rcf for 5 min. Purified Qdots and 6-HBs were mixed and incubated for 30 min. After that poly-T functionalized ~17 nm AuNPs were added and the solution was incubated for 1 h. Gel electrophoresis was then performed as explained above in the waveguide assembly protocol and finally tSEM imaging was performed.

**Multimerization of the waveguides.** For the multimerization of the waveguides, three different monomer 6-HBs were folded, that contained staple strands for the AuNPs attachment at every other binding site (BS 0, BS 2, BS 4, BS 6 and BS 8 with 5'-A15 extensions). Monomer 6-HBs A, B and C were folded separately with adding extra staple strands for blocking left/right sides (for A, staple strands of AL and for C, staple strands of CR) in the ss loops and interconnecting staple strands (for A, staple strands of AR- for B, staple strands of BL and BR- for C, staple strands of CL) again in the ss loops. A list of staple strands can be found in the appendix. The standard 6-HBs folding protocol was used as described above. After folding each monomer, 6-HBs were purified by PEG precipitation for each monomer (A, B and C) separately. For this, the unpurified 6-HBs solution was mixed at a 1:1 (v/v) ratio with PEG precipitation buffer (containing 15% PEG 8000 (VWR), 505 mM NaCl, 5 mM Tris and 1 mM EDTA). The solution was then mixed by tube inversion and centrifuged at 16,000 rcf for 25 min at room temperature. After the centrifugation, the supernatant was removed by a pipette. The pellet was re-suspended in the 1X TE containing 12 mM $MgCl_2$ folding buffer and incubated for 30 min at room temperature. To test multimerization of only 6-HBs before the AuNPs attachment, monomers (A, B, C) were mixed at 1:1:1 molar ratio in 1X TE containing 12 mM MgCl2 folding buffer and incubated overnight. After that, agarose gel electrophoresis and tSEM imaging were performed. For the waveguide multimerization, monomer waveguides were prepared separately with ~17 nm AuNPs as described above and after agarose gel electrophoresis purification of the monomer waveguides, they were mixed at a molar ratio of 1:1:1 and incubated overnight at room temperature. Afterwards, tSEM imaging was performed.

**tSEM characterization.** Carbon-coated TEM grids (400 mesh copper, carbon on formvar, Science Services) were plasma-treated for 20 seconds. 5 µL of the sample solution were applied on the TEM grid and incubated for 5 min. The excess solution was removed from the grid with a filter paper. Next, 5 µL of a 2% uranyl acetate solution was applied for 15 s to stain the 6-HBs and the solution was removed with a filter paper. The samples were scanned on a Helios 660 SEM/tSEM system (FEI) operated at 15 kV.

**Automated counting.** The contrast of the tSEM images was adjusted such that the 6-HBs were invisible, and only the AuNPs were visible. A custom MATLAB [158] routine was used to automatically identify and count the AuNPs in waveguide precursors (MATLAB script available in the appendix). The three main steps in the procedure are: (1) Localization, indexing and measuring of all observed AuNPs, performed on a thresholded image using the MATLAB function (MF) bwlabel, regionprops. (2) Identification of waveguide structures using a spatial clustering algorithm. For this, AuNPs were grouped into clusters if they were continually connected with center-to-center Euler-distances below a given threshold distance (90 nm within an error of one pixel). (3) Filtering and sorting of the clusters. Clusters contained 1 AuNP (mostly unbound AuNPs) to 25 AuNPs (mostly cross-linked waveguide precursors or waveguide precursors accidentally lying in close proximity). Clusters with more than 25 AuNPs were rarely observed, which were disregarded from the statistics. All clusters that were located closer than 90 nm to the boundary of the tSEM image were excluded.

# 4 ELECTRON ENERGY LOSS SPECTROSCOPY

The results presented in this chapter were produced in various collaborations. Electron energy loss spectroscopy measurements and analysis were performed by Assist. Prof. Søren Raza who was a former post-doc in the group of Prof. Mark L. Brongersma at Stanford University. Spherical monocrystalline CTAC capped gold nanoparticles were synthesized by Anja M. Steiner who is a PhD student in the group of Prof. Andreas Fery in Leibniz Institute for Polymer Research Dresden. Boundary element method simulations were performed by Martin Mayer (PhD student in the group of Prof. Andreas Fery) and Dr. Tobias König in Leibniz Institute for Polymer Research Dresden. Some sections of this chapter are based on the paper [A] Gür *et al., "*Self-assembled plasmonic waveguides for excitation of fluorescent nanodiamonds", *arXiv*.1712.09141*,* 2017.[159]

## 4.1 Introduction

Electron energy-loss spectroscopy (EELS) is a well-established analytical technique based on measuring the energy lost by swift electrons due to the inelastic scattering in a thin specimen [160]. EELS has been widely used for several decades and is considered an important experimental technique to acquire chemical, structural and optical information of nanoscale regions of the specimen [161]. Since EELS is performed in a transmission electron microscope (TEM) which uses focused electrons with initial kinetic energies of 60-300 keV, very high spatial resolution down to atomic level [162]–[166] and high energy resolution (100-200 meV) can routinely be achieved [167]. There are two approaches in which EELS data can be acquired [168]. The first approach is based on energy loss spectral information from the sample and that is why it is denoted as spectroscopy mode. This spectroscopy mode is more commonly applied which uses scanning TEM (STEM), where a highly-focused electron beam with an angstrom-sized spot is impacting a sample. The spectra from each spatial position of the sample, same size of the electron probe, are sequentially collected [169]. As the EELS is carried out in STEM mode, this technique is often abbreviated STEM-EELS. The second alternative approach is called energy filtering mode used in TEM (EFTEM) [170], where the sample is illuminated by a parallel electron beam for imaging larger areas. The image is then filtered according to the energy loss of the incident electrons which creates specific contrast effects in the image. Although both methods EFTEM and STEM-EELS produce comparable results [169], here the focus is on STEM-EELS mode as this method has been used in the experiments presented in this chapter.

### 4.1.1 Experimental description

The instrumentation of a standard EELS system is shown in Figure 4.1, which is incorporated into a TEM. The electron source, either thermionic or field electron emission, emits electrons which are accelerated to a preferred energy between 60-300 keV. The electron beam is then focused to a subnanometer-sized area on the specimen by electromagnetic lenses. The electron beam penetrates a very thin specimen, typically 10-200 nm thick, and subsequently scattered electrons are directed by another set of electromagnetic lenses. The scattered electrons with large angles by the specimen are directed to the annular detector to form an image of the sample. The scattered electrons with a smaller angle are directed to the EEL detector through a magnetic prism which is connected to the bottom of the microscope. The magnetic prism disperses (or bends) the inelastically scattered electrons depending the amount of energy that they have lost and such that they can be detected by the EEL spectrometer.

The electrons can interact with the sample in many different ways. Figure 4.1 illustrates the possible excitation and scattering events due to the electron beam irradiation. The elastically scattered electrons penetrate through the sample without any loss events, while the inelastically scattered electrons lose energy due to the various excitations in the sample. The sample with the excited state transitions to the unexcited state by the relaxations in the form of photons, X-rays, or Auger electrons. For examples, the relaxation of X-rays can be used for elemental analysis of the sample by energy dispersive X-ray spectroscopy [171] and the emission of photons upon excitation of plasmons in metallic samples can be detected by cathodoluminescence spectroscopy [172], [173]. Cathodoluminescence spectroscopy is explained in more details in chapter 5.

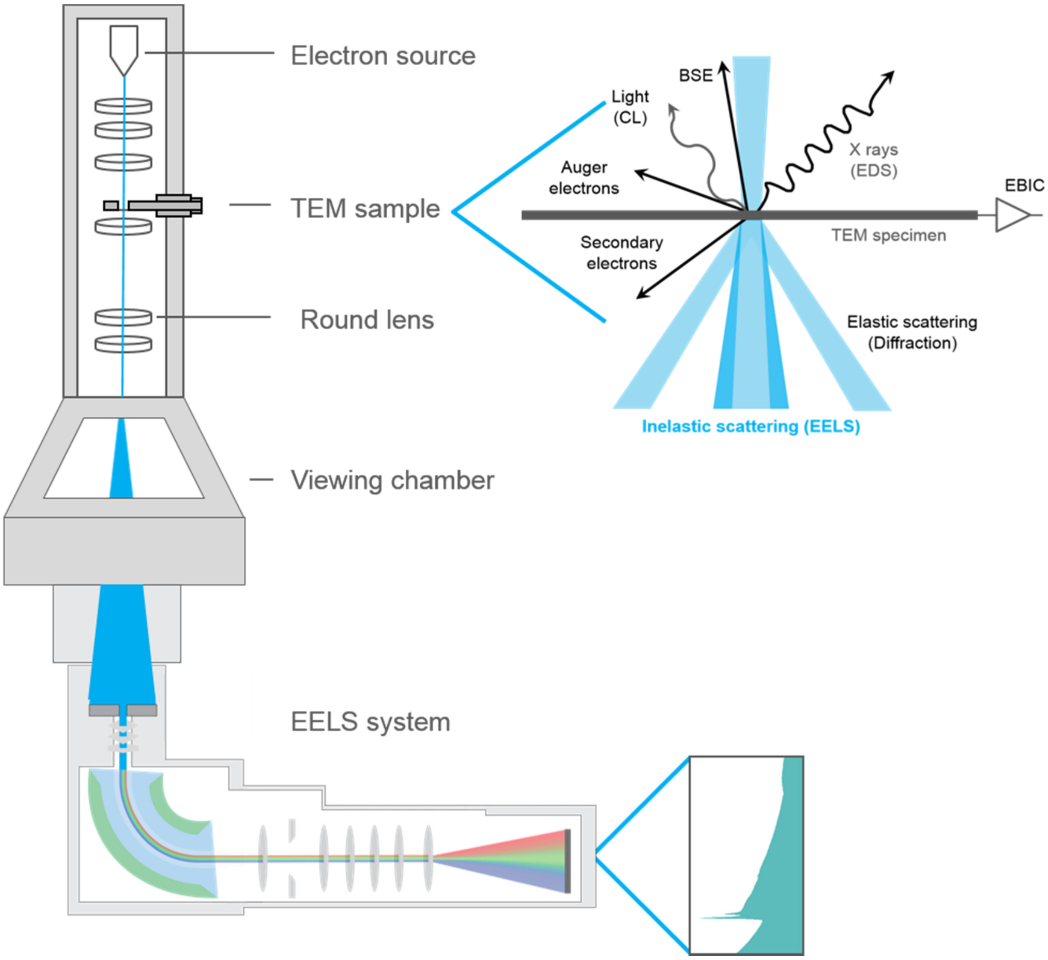

***Figure 4.1 | Schematic illustration of EELS instrumentation and swift electrons interaction with the sample, showing the possible scattering and excitation events due to the electron beam irradiation.*** *Reproduced from reference [174].*

A typical EEL spectrum as the one in Figure 4.2 depicts many prominent features and three separate regions can be distinguished. The first peak occurs at 0 eV and is therefore called the zero-loss peak (ZPL). The ZPL primarily represents all the incident electrons which have been elastically scattered due to the interaction with the atomic nucleus. Since the nuclear mass is much larger compared to the electron rest mass, the elastically scattered electrons lose very little energy which cannot be detected by EELS. In addition, inelastically scattered electrons with energy losses below the EELS resolution, typically below 100 meV (such as due to the phonon excitation), also appear in the ZPL peak. Since the ZPL is the strongest peak (for very thin samples) in the EEL spectrum, it is favorable to subtract the ZPL by post-processing (see method part) to best reveal the plasmonic features in the low-loss region.

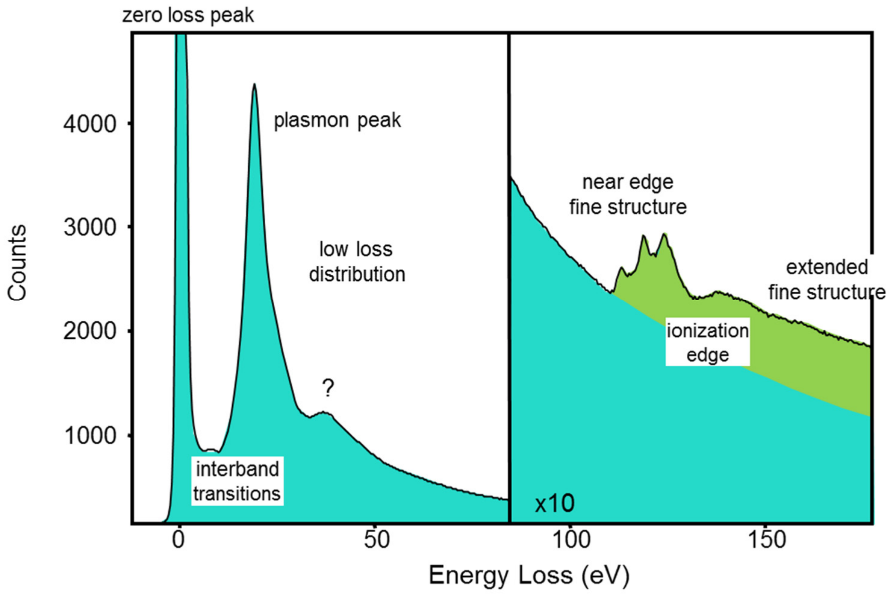

***Figure 4.2 | A typical EEL spectrum, showing the prominent features in three separate regions: zero-loss peak, low-loss, and core-loss regions.*** *Reproduced from reference [174].*

The low-loss region (below 50 eV) comprises the inelastic scattering events due to the interaction between incident electrons and weakly bound electrons in the sample. This energy region provides information about optical properties and band structure of the materials due to the plasmon excitations, exciton excitations, and inter-band transitions. The core-loss region (between 50 eV and hundreds of eV) covers the vast inelastic scattering events due to the incident electrons interaction with tightly bound core electrons of the atoms. The signal intensity in the core-loss region is much lower than the low-loss region and these high-energy losses can yield a two-dimensional map for structural and chemical information of the specimen at atomic resolution [175].

### 4.1.2 EELS for plasmonics

Here, the focus is on the low-loss EELS region for the study of optical properties of metallic structures, particularly inelastic scattering due to the excitations of surface plasmons (SPs). Mapping of localized surface plasmons of single metal nanoparticles with EELS technique was first reported in 2007 by two independent groups [176], [177]. During the last decade, EELS has received significant interests for SP mapping [115], [139], [178], [179] in the infrared, visible and ultraviolet regimes by taking advantage of its unbeaten high spatial resolution. EELS is now considered as the most advanced method to probe plasmonic modes and it is progressively used to study more complex nanostructures. Some examples of reported EELS studies for plasmonic systems are nanospheres [180], [181], nanorods [182], flat nanostructures [183], resonators [184], [185], nanoantennas [186], dimers [187], [188], trimers [189] and nanoparticle chains [114].

In this chapter, the self-assembly of functional plasmonic waveguides from highly monodispersed and monocrystalline AuNPs on 6-HB DNA origami nanotube was demonstrated. Both complete waveguides and as a negative control incomplete waveguides were prepared as shown in Figure 4.3. To characterize the optical properties of the assemblies at a single-particle level with the high spatial and spectral resolution, a highly localized fast electron beam was used as a point source to excite surface plasmons. The energy loss of the electrons due to the excitation of SPs and various coupled plasmonic modes was measured by EELS.

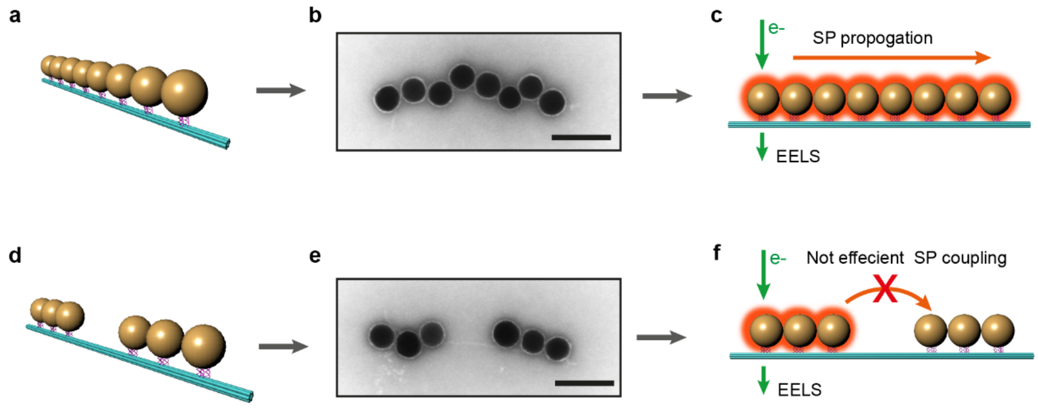

***Figure 4.3 | Overview of self-assembled DNA origami-based plasmonic waveguides in electron energy loss spectroscopy.*** *Schematic representation and corresponding transmission mode scanning electron microscope (tSEM) bright-field micrographs of complete (a, b) and incomplete waveguides (d, e). Surface plasmon (SPs) are excited by an electron beam and the energy loss of the electrons is detected by electron energy loss spectroscopy (c, f). SPs do not efficiently couple across the large gap. Scale bars, 100 nm.*

For all the EELS measurements in this chapter, the samples were deposited on a thin (10 nm thick) silicon nitride membrane and the transmission electron microscope system was used in scanning mode (STEM-EELS). A focused electron beam at an acceleration voltage of 300 keV was irradiated on the sample with 0.5 nm spatial resolution. The energy losses of swift electrons caused by SPs excitation and various SP modes were measured with an energy resolution of 0.1 eV.

### 4.1.3 Surface plasmon modes in nanoparticle chains

The electromagnetic field of the incident electrons can couple to the SPs of metal nanoparticles, hence, polarize them and give rise to SP excitations. This creates effective dipole moment and SP in nanoparticles hybridize differently depending on the orientation of excited dipoles.

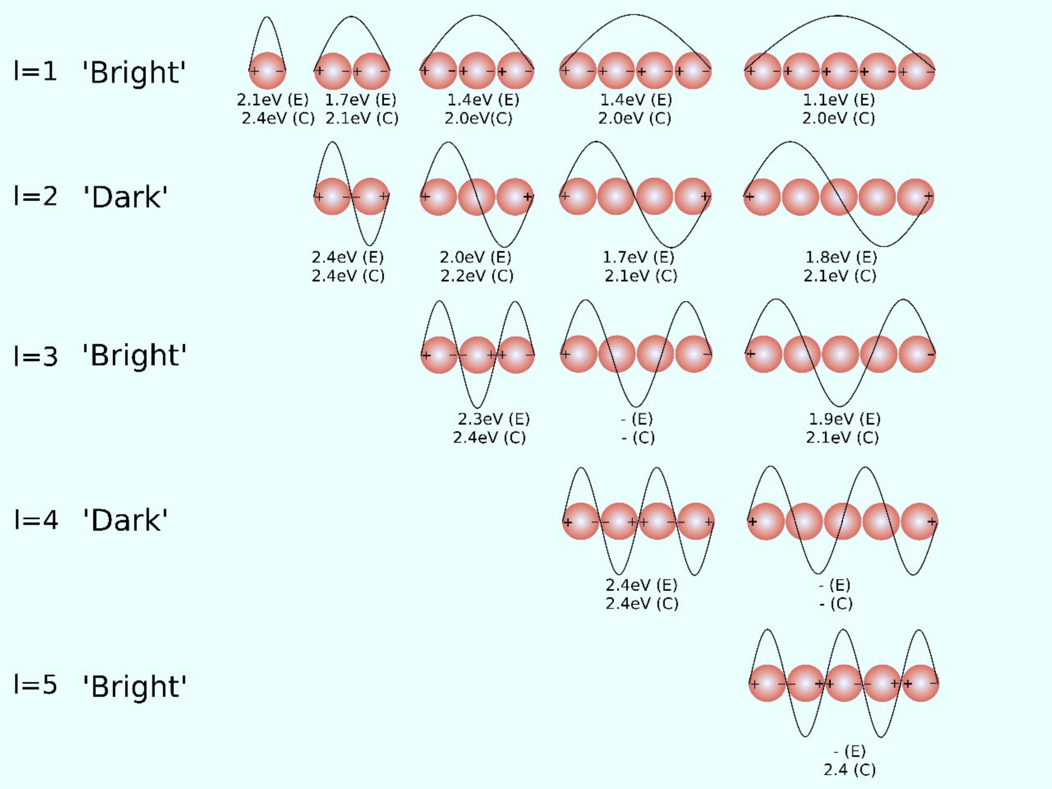

***Figure 4.4 | Schematic illustration displaying the longitudinal surface plasmon bright and dark modes in gold nanoparticle chains as a function of chain length.*** *Experimental (E) and calculated (C) energy loss values for each mode are depicted for 45 nm AuNPs with 1 nm inter-particle spacing. The dipolar surface charges shown on the structures are not quantitative. Reproduced from reference [114].*

There are two main SP coupling modes: longitudinal (L), where the dipoles are parallel to the particle line and transverse (T) mode, where the dipoles are perpendicular to the AuNP chain. Figure 4.4 depicts the evolution of the L modes as a function of a number of particles in the chain and energy. One can label the L modes according to mode number (1, 2, 3...) from lowest to highest energy. The lowest energy L1 mode, referred to super-radiant mode [114], is a fundamental dipole mode where individual dipole of each nanoparticle creates a large dipole moment. The odd mode numbers (L: 1, 3, 5...) are assigned as bright modes as they have a net dipole, while the even mode numbers (L: 2, 4...) are considered non-radiative dark modes since they have no net dipole.

## 4.2 EELS characterization of waveguides with a comparable inter-particle distance to the particle size

In the first set of EELS measurements, oligonucleotide functionalized AuNPs with a dimeter of ~28 nm were used, which were synthesized based on hydroquinone method (for the synthesis, functionalization and assembly details, see section "3.3 Attachment of larger gold nanoparticles" in chapter 3). A single AuNP, a randomly assembled dimer and a waveguide with nine AuNPs were analyzed, as shown in Figure 4.5 TEM micrographs. The ninth AuNP is a result of an unspecific binding to the single-stranded loops at the end of the 6-HB, for the details see the subsection "complexes contain more than eight gold nanoparticles" in chapter 3.2.3.

Figure 4.5a shows the EELS spectra for a single AuNP and the spectra are collected according to electron beam excitation positions, colored squares in TEM micrograph. Since the AuNP is spherical and symmetric, irrespective of electron beam impact areas single energy-loss peak at 2.3 eV was observed, which plasmon resonance energy of the single particle is. The experimental EELS map at this resonance energy reveals that the energy-losses are due to the dipolar mode of the AuNP.

Figure 4.5b shows the EELS spectra of the AuNP dimer with about 1 nm spacing. Associated electron beam impact positions (colored squares), on the edge of the dimer and on the center of the gap, are depicted. As previously reported for metal dimer EELS studies [187], [190]–[193], plasmon coupling within the dimer splits into two distinct dipoles, bonding and anti-bonding dipoles, which result in the energy-loss peaks at 1.75 eV and 2.3 eV respectively. In agreement with the literature [114], these resonances can be assigned L1 super-radiant, bright mode (bonding interaction) at 1.75 eV and L2 dark mode (anti-bonding interaction) at 2.3 eV. The transverse mode and L2 dark mode show similar experimental EELS maps as in good agreement with previous reports [114], [194], [195]. Since the resonance energies of transverse mode and L2 mode are very close and probably spectrally broad, they could not be distinguished in EELS.

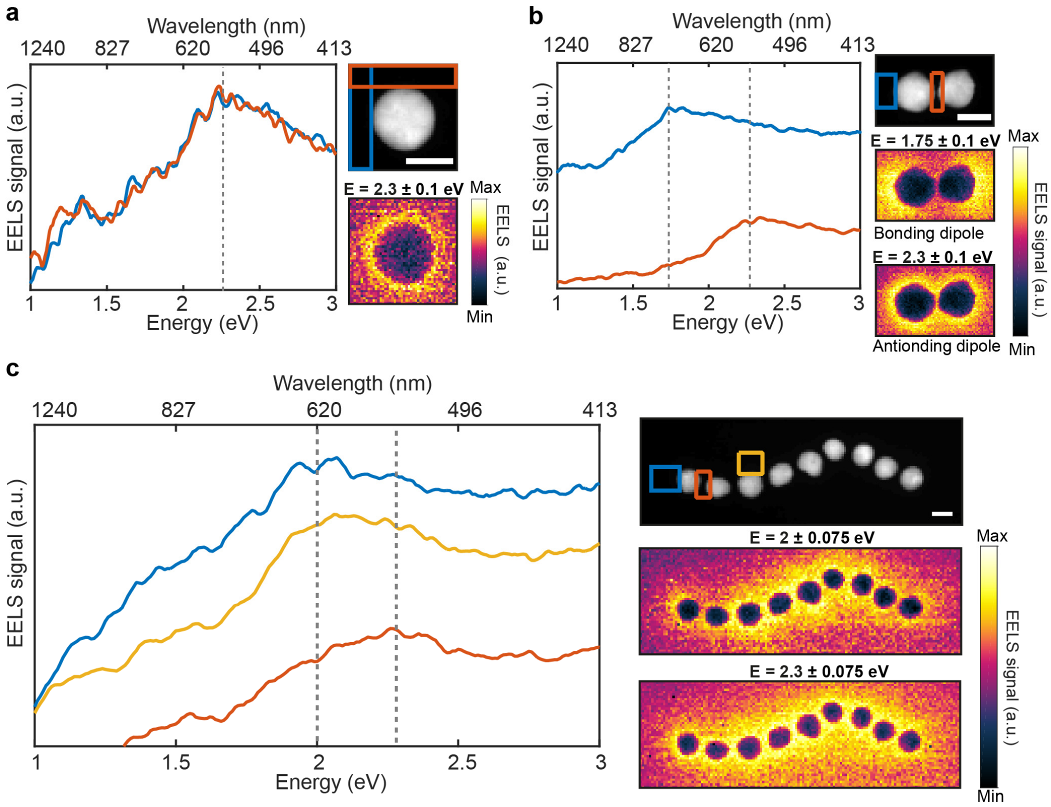

***Figure 4.5 | Electron energy loss characterization of a single particle, a dimer, and a waveguide.*** *Experimental EELS spectra are acquired from all the electron beam excitation points within the squares in corresponding colors in TEM micrographs. The EELS maps show EELS intensity as a function of electron beam excitation spot at the corresponding resonance energies. All the AuNPs are ~28 nm in diameter. Scale bars, 20 nm.*

Figure 4.5c shows the EELS spectra and EELS maps of the waveguide with nine AuNPs attached and a ~14 nm spacing. The electron beam was irradiated at different locations in the vicinity of AuNPs in the waveguide, and the corresponding spectrum was acquired according to electron beam excitation locations. Irrespective of the excitation locations, all the spectra show the same profile with a broad peak. The EELS maps were recorded at 2.3 eV and at 2 eV where these energies appear in the broad peak of the EELS spectra. The EELS map at 2.3 eV, where single particle plasmon resonance was observed at this energy, can be considered as a transverse mode of the waveguide. Since the SP coupling is weak due to the large inter-particle spacing, neither EELS spectra nor EELS maps are distinct at 2 eV. Therefore, it cannot be concluded that what mode the waveguide has at this energy. However, it is probably L1 mode, since L1 is always the lowest energy mode.

## 4.3 EELS characterization of waveguides with closely spaced particles

As it has shown from the experiments described in the previous section, the inter-particle distance is a critical aspect for SP coupling. Therefore, minimizing inter-particle spacing and maximizing plasmonic coupling between the AuNPs are required. For this, AuNPs with a size equal to the distance of binding sites on the 6-HB were synthesized by seed-mediated method [196]. This method provides more control over the size and shape of the AuNPs compare to HQ method which was used in chapter 3.

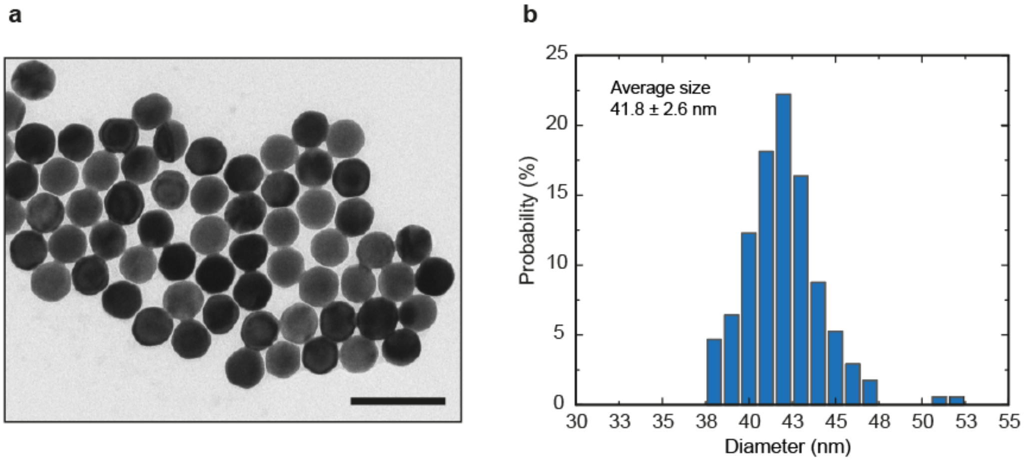

***Figure 4.6 | Characterization of monocrystalline and monodispersed ~42 nm gold nanoparticles.*** *A TEM image (a) and size distribution analysis (b) of AuNPs. Scale bar, 100 nm.*

Since this method produced AuNPs with precise size and highly spherical shape, CTAC capped AuNPs were used for the rest of the studies presented in this theses. Due to the changes of the ligand cap from BSPP to CTAC, the new protocol was developed for the functionalization of AuNPs with thiol-modified oligonucleotides, see Materials and methods section for details. Size distribution analysis and TEM micrograph reveal that the mean size of the AuNPs is ~42 nm as shown in Figure 4.6.

These highly monodispersed and monocrystalline AuNPs were functionalized with thiol-modified oligonucleotides. The functionalized AuNPs hybridize to complementary binding sites displayed on the 6-HB DNA origami nanotube (same as in chapter 3).

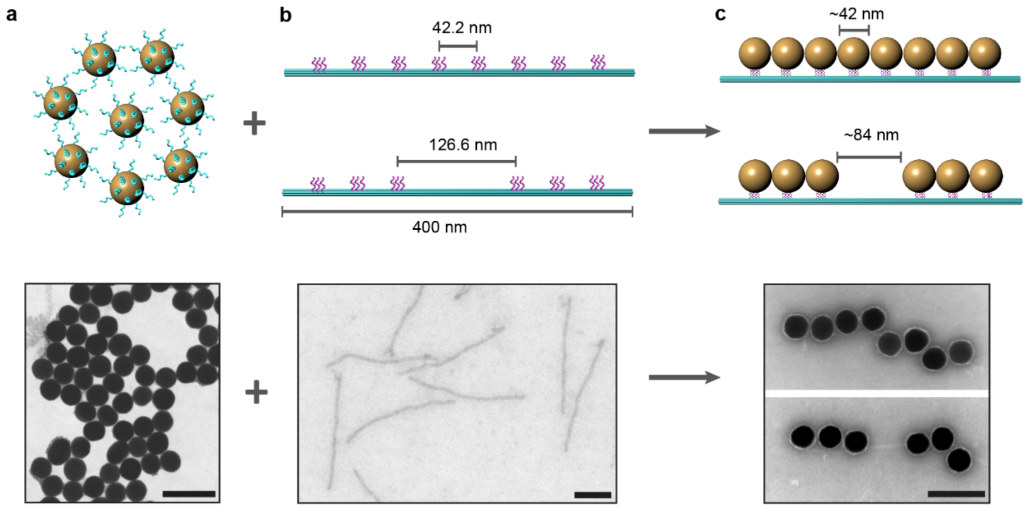

***Figure 4.7 | Design and assembly reaction of waveguides: schemes and corresponding tSEM bright-field micrographs.*** *(a) Thiol-modified oligonucleotides functionalized ~42 nm AuNPs. (b) 6-HBs design with binding sites for complete and incomplete waveguides. (c) Correctly assembled eight particles attached complete waveguide and six particles attached incomplete waveguide with ~84 nm gap between trimers. Scale bars, 100nm.*

As shown in Figure 4.7, the 6-HB structures were mixed with functionalized AuNPs and excess AuNPs and aggregates were removed by agarose gel electrophoresis. Eight AuNPs attached complete waveguides with an estimated inter-particle gap of 2 nm and incomplete waveguides where binding sites were omitted for two particles in the center of the 6-HBs were prepared. This incomplete waveguide with a gap of about 84 nm served as a negative control for the measurements. The correctly assembled complete and incomplete waveguides were visualized by tSEM micrographs and these assemblies are in good agreement with the designs, see Figure 4.7.

First, begin with the single particle analysis, Figure 4.8 shows EEL spectrum of a single AuNP with a diameter of ~42 nm where the electron beam was used to excite the vicinity of the AuNP, indicated by the blue square. The spectrum shows the plasmon resonance energy of the single AuNP at 2.3 eV (~539 nm). Experimental and simulated EELS maps were recorded at this resonance energy, showing energy loss intensity of the electrons (or electron count at this resonance energy) as a function of electron impacting spots. For the single particle, as in the previous section, only a single energy-loss peak in the spectrum was observed due to the excitation of dipolar mode, confirmed by both experimental and simulated EELS maps.

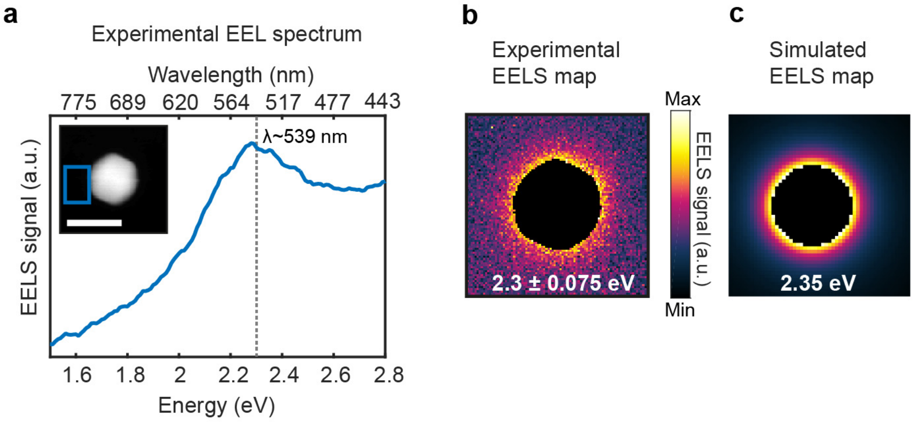

***Figure 4.8 | Electron energy loss spectroscopy characterization of a single gold nanoparticle****. EEL spectrum of a single AuNP (a), taken in the location indicated by the blue square in dark-field TEM micrograph inset, Scale bar, 50 nm. Experimental (b) and simulated (c) EELS map of the single AuNP. The AuNPs are 42 nm in diameter.*

Next, the waveguide assemblies composed of ~42 nm AuNPs were investigated. Figure 4.9 (a, d) shows the experimental EELS spectra of a complete and an incomplete waveguides, the spectra were collected by impacting a focused electron beam in the vicinity of AuNPs indicated by the squares in corresponding colors in TEM micrographs insets. The gap between the trimers in the incomplete waveguide in Figure 4.9d was measured as ~81 nm which is in good agreement with theoretical value in the design.

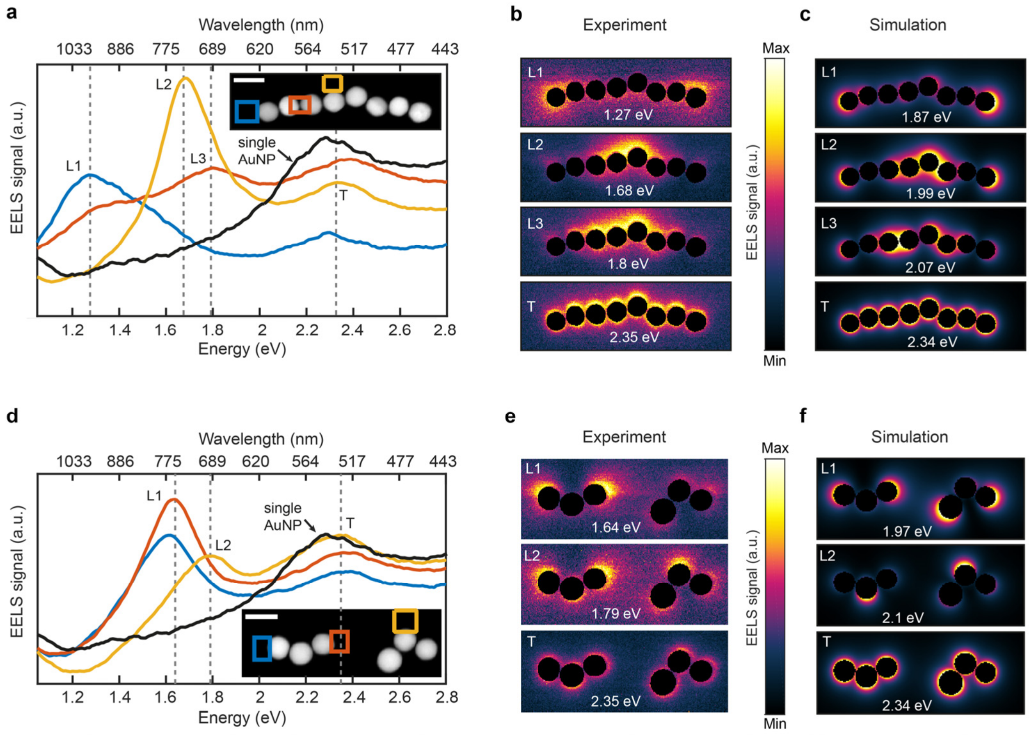

***Figure 4.9 | Electron energy loss characterization of a complete and an incomplete waveguides****. Experimental EELS spectra (a, d) are acquired from all the excitation points within the squares in corresponding colors in the TEM micrographs insets. Scale bars, 50 nm. Experimental (b, d) and simulated (c, f) EELS maps at different energies, showing longitudinal super-radiant mode (L1), dark mode (L2), bright mode (L3), and transverse (T) modes. Experimental EELS maps are centered at the resonance energies of each mode with a spectral window of 0.15 eV. The AuNPs are ~42 nm in diameter.*

The energy loss peaks for longitudinal (L = dipoles along the waveguide) and transverse (T = dipoles perpendicular to the waveguide direction) modes can clearly be distinguished. The energies of the L modes are red shifted while the energy of the transverse mode (2.35 eV, 527 nm) is slightly blue shifted compared to single AuNPs resonance energy (2.3 eV, ~539 nm, in Figure 4.8). The lowest energy mode L1, super-radiant mode, is detected at 1.27 eV (~976 nm). The L2 dark mode (non-radiative) at 1.68 eV (~738 nm) and L3 bright mode (radiative) at 1.8 eV (~689 nm) were detected. Dark modes are also considered to effectively support propagation of SP modes along the closely spaced metal nanoparticle due to lower radiative losses than bright modes [197].

The EELS maps of complete and incomplete waveguides at all the detected resonance energies shown in the spectra were recorded. In order to assign each mode, boundary element method (BEM) simulations were performed with the same particle arrangement as in the experiments. The size and location of AuNPs were obtained from high-resolution electron micrographs. The modeled maps for each mode are in good agreement with experimental results. The energy differences of the modes between experiment and simulation come from the parameters which were not included in simulations for simplicity, such as DNA capping on the AuNPs surface, deviations from perfect spheres and the refractive index of silicon nitride substrate. These EELS results resemble the previous report where they study the surface plasmon resonances of strongly coupled AuNP chains from monomer to hexamer was studied [114].

In principle, there are even higher order bright and dark sub-modes (L: 4, 5, 6, 7, 8). However, these modes could not be detected for some reasons: first, the resonance energies are too close to one another and these higher order modes overlap with the strong T mode, which makes hard to distinguish them (see Figure 4.9). The second reason is that the surface plasmon moves slower at higher energies [1], i.e. it takes a longer time to form the higher-order modes. Perhaps this “formation” time of the higher-order modes is too long compared to the interaction time of the swift electrons. In addition, surface plasmons with lower group velocity also experience more losses [198], and hence, the higher-order modes may have weaker amplitudes. Both effects contribute to low EELS intensities. However, in the measured EELS spectra, the observed spectral shape of transverse mode slightly varies depending on the electron beam excitation positions, which might be a sign of these different higher order sub-modes, see Figure 4.9 (a and d).

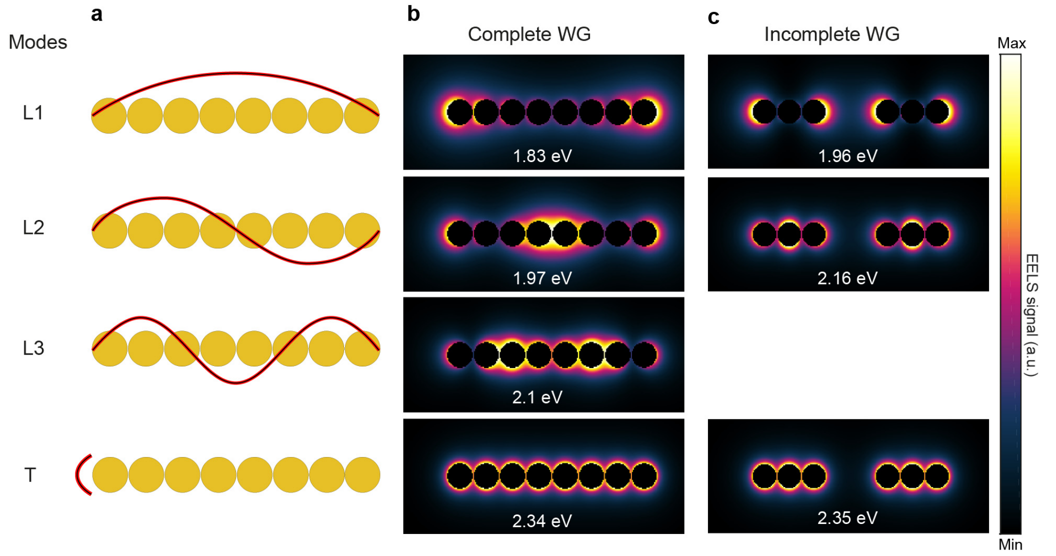

***Figure 4.10 | Schematics of coupled plasmonic modes and boundary element model simulations of linear complete and incomplete waveguides EELS maps.*** *Scheme illustrating the SP modes evolution in the complete waveguide (a). Simulated EELS maps (b, c) showing the longitudinal modes: super-radiant mode (L1), dark mode (L2) and bright mode (L3), and transverse mode (T). The size of AuNPs is assumed as 42 nm with a 2 nm inter-particle spacing. The gap between trimer AuNPs in the incomplete waveguide is assumed as 90 nm.*

The incomplete waveguide reveals plasmon resonances of individual trimers that couple differently one another across the large gap, whereas the complete waveguides are supporting continuous SP propagation along the entire chain of eight particles. The larger redshift of the super-radiant mode (L1) and the dark mode (L2) in the complete waveguide compared to L1 and L2 modes of the incomplete waveguide is also an evidence for an effective SP propagation. To investigate the effect of the geometrical deviations from a non-linear assembly, linear complete and incomplete waveguides were simulated, see Figure 4.10. The simulation results suggest only small energy differences for each mode compared to the slightly disordered waveguides in Figure 4.9c. This is also confirmed by a previous simulation study where disordered and irregular sizes of single particle chains were investigated [112].

## 4.4 EELS characterization of waveguides with extremely short inter-particle distance

The inter-particle spacing can be further decreased by preparing slightly bigger AuNPs than the distance between the binding sites in the 6-HB design. The size distribution analysis and a TEM micrograph reveal that the mean size of the AuNPs of this batch is ~45 nm as shown in Figure 4.11.

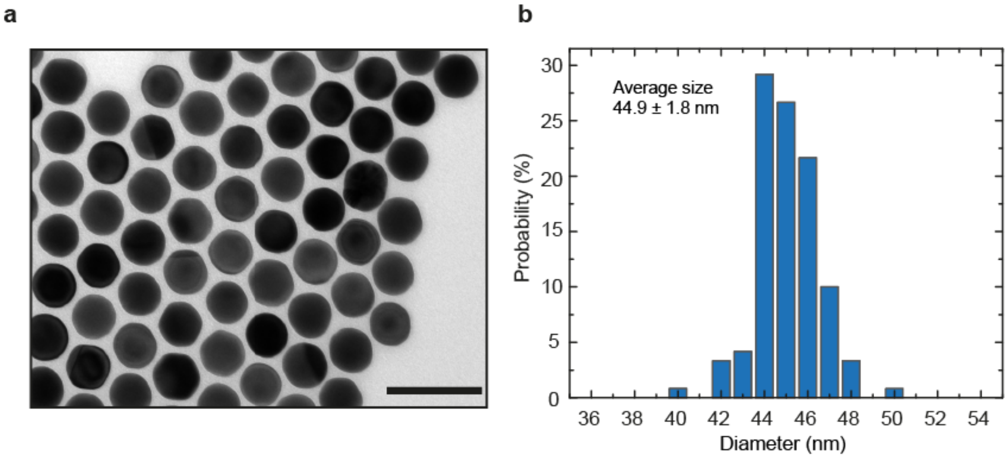

***Figure 4.11 | Characterization of monocrystalline and monodispersed ~45 nm gold nanoparticles.*** *TEM image (a) and size distribution analysis (b) of AuNPs. Scale bar, 100 nm.*

As the combined diameter of the AuNPs and the oligonucleotide shell is larger than the distance between the binding sites on the 6-HB (42.2 nm), the particles are assumed to minimize their free energy during the drying process [113], thereby minimizing the inter-particle spacing, which occasionally results in slightly deformed zigzag patterns, see Figure 4.12. This mechanical compression of the protective oligonucleotides layer around the AuNPs allowed reducing gap sizes from around 7 nm for mechanically uncompressed functionalized AuNPs [156] to below 1 nm. Reinforcing the DNA origami scaffold [109] may straighten the structures into more linear configurations if so desired.

Figure 4.12 shows EELS characterization of the complete waveguides composed of ~45 nm AuNPs with a spacing that is estimated to be less than 1 nm from high-resolution TEM images. The EEL spectra are collected by impacting a focused electron beam in the vicinity of AuNPs indicated by the squares in corresponding colors in TEM micrographs insets. The lowest energy mode L1 is detected at 0.62 eV for a waveguide composed of seven particles and at 0.42 eV for an eight particle waveguide. These energies lie in the infrared regime. Compared to the results in Figure 4.8a, a redshift for all the L modes were observed, which are attributed to the increased plasmon coupling from smaller gaps. By using the same DNA origami template, the waveguide resonances can be tuned simply by changing the particle size. The particle size only changed by ~3 nm in this section, and the L1 mode shifted by almost 1 eV for the eight particle waveguide. This is a good control for tuning the resonances of the waveguides. There is a probability that the electron beam could initiate the fusing process [199] between AuNPs due to the high energy dose and very narrow gaps (below ~1 nm) between the particles.

The gradual redshift might theoretically also be a result of fused particles which act as a nanowire. Since the experimental and simulated EELS maps match very nicely and unfused particles were used in the simulations, one can consider that is probably a good sign of the particles not being fused into one long linear chain. A possible situation could be that a couple of particles were fused, but probably not the whole waveguide.

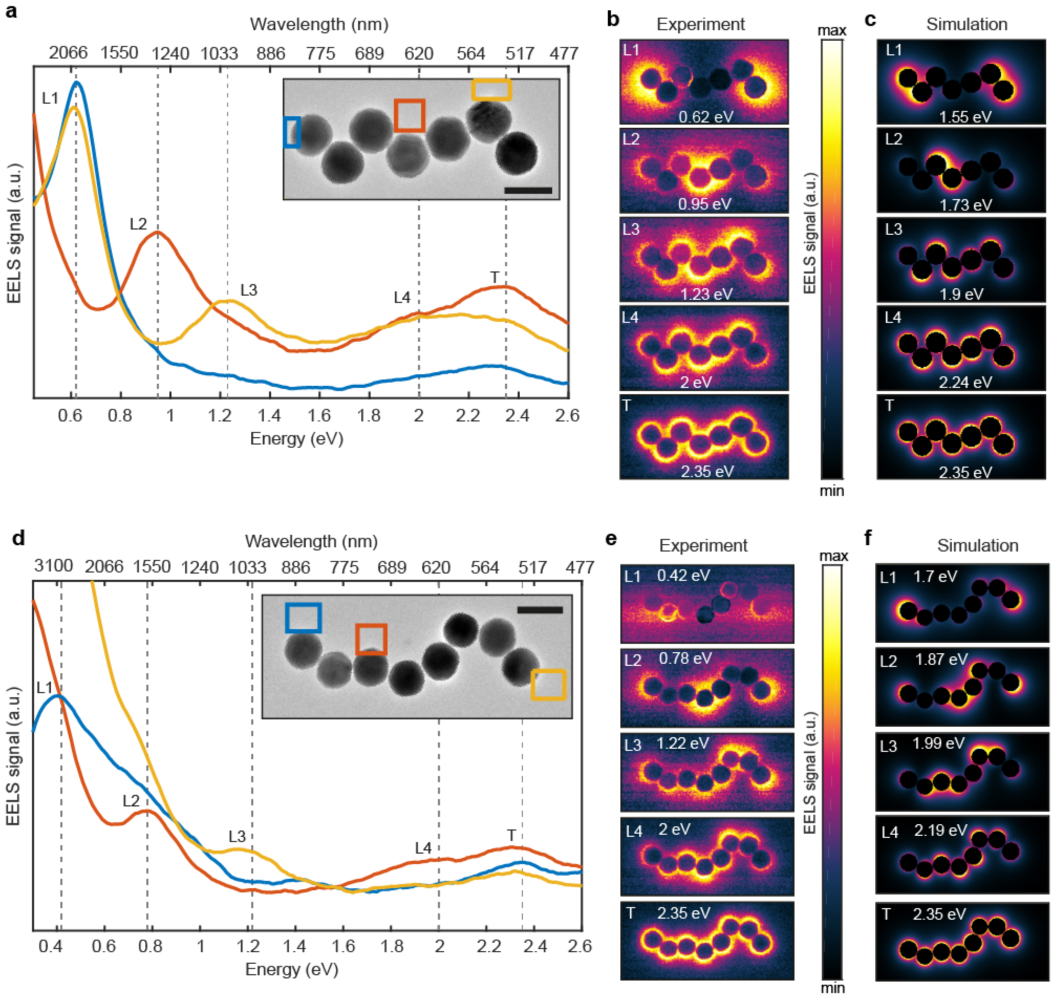

***Figure 4.12 | Electron energy loss spectroscopy characterization of complete waveguides composed of ~45 nm gold nanoparticles with less than 1 nm inter-particle spacing.*** *Experimental EELS spectra (a, d) of the waveguides are acquired from all the excitation points within the squares in corresponding colors in the TEM micrographs insets. Scale bars, 50 nm. Experimental (b, e) and simulated (c, f) EELS maps of the longitudinal modes (L1, 2, 3, 4) and transverse (T) mode. Experimental EELS intensity maps are centered at the resonance energies of each mode with a spectral window of 0.15 eV.*

## 4.5 Concluding remarks

In conclusion, the nature and spatial distribution of SP modes were systematically studied in both complete and incomplete waveguides with different sizes and inter-particle distances. The understanding of fast electrons coupling to SPs was addressed by both experimental and modeling EELS results. The results reveal that SP coupling between the particles increases with a decreasing inter-particle spacing caused by an increasing particle diameter at a constant distance between binding sites. With the aid of programmability of the binding sites on the DNA origami template and synthesis of precise sized AuNPs, a good control was demonstrated to tune SP resonances of the waveguides. High-resolution energy mapping of the waveguide assemblies by the spectral and spatial EELS probing showed multiple coupled bright and dark SP modes ranging from the visible to the infrared regimes. Furthermore, EELS probing allows the detection of the dark SP modes which cannot be resolved by any other optical techniques. The experimental results are in excellent agreement with boundary element method EELS simulation results.

## 4.6 Materials and methods

**Synthesis of monocrystalline spherical AuNPs**. The AuNPs were synthesized based on a seed-mediated growth and the protocol adopted from Steiner *et al.*[196]. To form single-crystalline 2 nm Au seeds, 25 µL of 50 mM hydrogen tetra-chloroaurate ($HAuCl_4$, >99.9%, Sigma Aldrich) were added to 4.7 mL of 0.1 M hexadecyltrimethyl-ammonium bromide (CTAB, 99%, Merck KGaA) solution and slowly stirred for 10 min at 32 °C. Afterwards, 300 µL of freshly prepared 10 mM sodium borohydride ($NaBH_4$, 99%, Sigma Aldrich) were injected under vigorous stirring, which was continued for 30 seconds. For the next overgrowth step, the seeds were aged for 25 min at 32 °C to ensure the complete reaction of $NaBH_4$ and also reproducibility.

To prepare 8 nm Au seeds, 20 mL of 200 mM of hexadecyltrimethylammonium chloride (CTAC, 25 wt.% in ultrapure water, Sigma Aldrich), 15 mL of 100 mM ascorbic acid (AA, $C_6H_8O_6$, >99%, Sigma Aldrich), and 1 mL of the initial CTAB- capped Au seeds were mixed in a 100 mL beaker. Subsequently, 20 mL of aqueous 0.5 mM $HAuCl_4$ solution was quickly injected under stirring. The reaction was allowed to continue for 15 min at room temperature (RT). The seeds were centrifuged at 15,000 rcf for 1 h and washed once more with ultrapure water. For the next round of growth, the Au seeds were dispersed in 10 mL of aqueous CTAC solution (10 mM).

For this study, two batches of AuNPs were used with a diameter of 41.8 ± 2.6 nm or 44.9 ± 1.8 nm. To prepare CTAC-capped AuNPs, aqueous solutions of CTAC (60 mM, 200 mL), AA (1 M, 260 µL) and 2.5 mL (for a diameter of 41.8 nm), 1.95 mL (for a diameter of 44.9 nm) of the 8 nm seeds were mixed. Additionally, 200 mL of a growth solution including $HAuCl_4$ (1 mM) and CTAC (60 mM) were prepared and heated up to 45°C until the precursor complex was formed. Afterwards, the growth solution was added dropwise under moderate stirring using a syringe pump system at an injection rate of 1.0 mL/min. The reaction was allowed to continue for 12 h at RT after the injection was finished. The final product was collected by centrifugation at 12,000 rcf for 20 min and washed twice with 2 mM CTAC solution. For further use, the nanoparticles were re-dispersed in 30 mL of aqueous CTAC solution (5 mM). The respective size distribution (41.8 ±2.6 nm, 44.9±1.8 nm) was determined by TEM image analysis of at least 120 particles.

**Functionalization of AuNPs.** Before the functionalization of AuNPs with oligonucleotides, the CTAC cap was exchanged with bis (p-sulfonatophenyl)-phenylphosphine dihydrate dipotassium salt (BSPP, Sigma-Aldrich). For this, first 1 mL of the CTAC capped AuNPs was centrifuged at 10,000 rcf for 5 min to remove the excess CTAC, and they were dissolved in 1 mL of ultrapure water. After washing with ultrapure water, AuNPs were once more centrifuged at 10,000 rcf for 5 min, and resuspended in 1 mL of 5 mM BSPP supplemented with 1% Tween-20 (Applichem). The solution was then shaken for overnight. After that, 1 mL of methanol was added (the colour changed from red to blue), and centrifuged at 10,000 rcf for 5 min. The supernatant was discarded and AuNPs were resuspended in 1 mL of a 5 mM BSPP solution. After that, the AuNP solution was vortexed, and then shaken for 2 h at 25 rpm in a rotator. During this time, the solution was sonicated for 20 s several times until the AuNP solution turned red.

Next, AuNPs were conjugated to thiol-modified oligonucleotides (IDT), as described in chapter 3. First, the thiol-modified oligonucleotides (5’ ThioMC6-T15) were incubated with 20 mM TCEP (Tris (2-carboxyethyl) phosphine hydrochloride, Sigma-Aldrich) for 45 min. Then, AuNPs and the thiol-modified oligonucleotides were mixed in 0.5X TBE (Tris base, boric acid, EDTA, pH = 8.0) buffer at a ratio of 1:3000 (AuNP: ssDNA). To increase the oligonucleotide loading density on the surface of AuNPs, an aqueous 5 M of NaCl solution was added in four steps to reach a final concentration of 500 mM NaCl. After each addition of NaCl, the AuNPs solution was sonicated for 20 s and incubated for 20 min. After the last NaCl addition, the mixture of AuNPs and oligonucleotides was shaken for 2 days at 50 rpm with vibration mode at RT in a rotator. During this time, the solution was sonicated for a min several times to prevent unspecific dimer, trimer AuNP formation. After that, the solution was centrifuged at 10,000 rcf for 5 min to concentrate the AuNPs and supernatant was removed, and AuNPs were resuspended in 400 µL of 0.5X TBE buffer. Afterwards, the excess of oligonucleotides was removed by ultrafiltration (100 kDa MWCO, Amicon Ultra, AMD Millipore) and washed five times with 400 µL of 0.5X TBE buffer at 10,000 rcf for 5 min right before mixing with 6-HBs.

**Folding of 6-HBs.** The same 6-HB design and staple strands were used as in chapter 3. Briefly, to attach the thiol-modified poly-T conjugated AuNPs, 6-HBs were designed for eight binding sites (binding sites numbers from 1 to 8) with a center-to-center distance of 12 helical repeats (126 bp) resulting in 42.2 nm between two binding sites. Each binding site consisted of three single-stranded poly-A (5’-A15) extensions of staple strands on three adjacent helices. For the incomplete waveguides, binding sites number 4 and 5 staple strands without poly-A extensions were used resulting in a center-to-center distance of 126.6 nm between binding sites number 3 and 6. To form the 6-HBs, 10 nM of p8064 scaffold (obtained from Dr. David Smith, IZI Leipzig), 170 short staple strands (IDT) (including respective binding sites as poly-A extensions) at 100 nM (each), 5 mM Tris (Applichem), 1 mM EDTA (Applichem) (pH 8) and 12 mM MgCl2 (Applichem) were mixed. The mixture was annealed in a thermal cycler (Bio-Rad C1000

Touch) from 80 to 65 °C at a rate of -1 °C/min and from 65 °C to RT at a rate of -1 °C/20 min. After the folding reaction, 6-HBs were purified from excess staple strands by ultrafiltration (100 kDa MWCO) washing five times with 400 µL of 1X TE containing 12 mM MgCl2 at 10,000 rcf for 5 min.

**Waveguide assembly.** The purified 6-HB solution (0.8 nM final concentration) was quickly mixed with freshly functionalized and purified AuNPs (10 AuNPs/binding site) in 1X TE containing 12 mM $MgCl_2$ and incubated for 1 h at RT. Correctly assembled waveguides were separated from excess AuNPs and aggregates by agarose gel electrophoresis in a 0.75% agarose gel (Roche) containing 0.5X TBE buffer and 12 mM $MgCl_2$. The same buffer was used as the running buffer. All samples were mixed with a 20% volume of gel loading dye (50% glycerol, 5 mM Tris, 1 mM EDTA, 0.25% bromophenol blue and 0.25% of xylene cyanol) just before loading the samples to the gel pockets. Electrophoresis was performed in an ice-box at 4 °C for about 2 h at 70 V. The selected bands were cut out and chopped into small pieces. The waveguides were extracted from the gel with Freeze 'N Squeeze spin columns (Bio-Rad) by centrifugation at 5,000 rcf for 10 min.

To confirm the waveguide assembly, waveguide samples were imaged by SEM/tSEM. For this, carbon-coated TEM grids (carbon on formvar, Science Services) were plasma-treated for 20 s. Next, 5 µL of the waveguide sample solution was applied on the TEM grid and incubated for 5 min. The excess solution was removed from the grid with a filter paper. Next, 5 µL of a 2% uranyl formate solution was applied for 1 minute to stain the 6-HB structures, and the solution was removed with a filter paper. The samples were scanned on Gemini SEM500 (Zeiss) and Helios 660 SEM/tSEM system (FEI) operated at 15 kV.

**EELS sample preparation.** Silicon nitride TEM membranes (10 nm thick, nine windows, SiMPore TEM Grids) were used as a thin substrate for EELS measurements. The TEM grids were plasma-treated for 3 min. Next, 10 µL of poly-L-ornithine solution (0.01%, Sigma-Aldrich) was applied and incubated for 30 s and finally, the membrane was rinsed with ultrapure water and excess water was removed with a filter paper. Next, 10 µL of waveguide sample solution was applied and incubated for 2 min. Then the

TEM membrane was washed once more with ultrapure water and the excess solution was removed with a filter paper.

**EELS Measurements.** The EELS measurements were performed with a FEI Titan transmission electron microscope equipped with a monochromator and an image corrector. The microscope was operated in monochromated STEM mode at an acceleration voltage of 300 keV, providing a spot size of approximately 0.5 nm and an energy resolution of 0.10 eV (measured as the full-width at half-maximum of the zero-loss peak). The microscope was equipped with a Quantum 966 electron energy-loss spectrometer and the Gatan DigiScan acquisition system, which recorded an entire EELS intensity map in 5 to 25 min, depending on the number of pixels. A C3 aperture size of 50 μm, a camera length of 38 mm, an entrance aperture of 2.5 mm and a spectral dispersion of 0.01 eV per pixel was used. In addition, the automatic drift and dark current correction function included in the acquisition system was used. The individual EELS spectrum of the EELS intensity maps (with pixel sizes typically of 1–1.5 nm) were recorded with acquisition times ranging from 5 to 15 ms.

**EELS spectral processing.** To minimize the impact of monochromator drift during EELS acquisition, each row in the EELS data matrix was normalized to the EELS spectrum of the first column in the corresponding row. Afterwards, the zero-loss peak of each EELS spectrum was removed. To this end, two different methods were used, which both provide similar results: (i) the reflected-tail method, where the negative energy part of the zero-loss peak is mirrored around the zero-energy point to reconstruct the zero-loss peak, or (ii) fitting of a power-law function in the energy range 0.5 eV to around 1 eV to reconstruct the background signal. The resonant EELS intensity maps shown in this chapter depict the summed background-removed EELS signal in a 0.15 eV spectral window centered at the resonance energies. The EELS signal from inside the nanoparticles was noisy and therefore removed in the map depictions. To detect the pixels inside the nanoparticles, image analysis was performed using the Image Processing Toolbox in MATLAB.

**EELS-BEM simulations.** Simulations of electron energy loss spectra and mappings were performed using the MATLAB MNPBEM13 toolbox [200], which is based on the boundary element method (BEM) open source code by F. J. Garcia de Abajo and A. Howie [201]. Each sphere of the waveguide was approximated by triangulation (400 vertices/particle). The dimensions and relative positions of the AuNPs were approximated to those observed in the TEM micrographs of the corresponding waveguide. The dielectric properties of gold were taken from P. B. Johnson and R. W. Christy [202]. An effective medium (n = 1.3) was chosen to compensate the lack of the vacuum/substrate interface. The energy of the simulated electron beam was set to the experimental accelerating voltage of the TEM. For each waveguide, several spectra were evaluated in the energy range from 1-4 eV at different electron beam positions (non-penetrating) to ensure excitation of all possible plasmonic modes. Electron energy loss mappings were performed at selected energy levels and were simulated by a 2 nm mesh of the electron beam.

# 5 CATHODOLUMINESCENCE IMAGING SPECTROSCOPY

The results presented in this chapter were obtained in various collaborations. Cathodoluminescence imaging spectroscopy measurements and analysis were performed together with Dr. Cillian McPolin who was a post-doc in the group of Prof. Anatoly V. Zayats in King's College London at the time of the measurements. Photoluminescence measurements and analysis were done together with Diane Roth who is a PhD student in Prof. Anatoly V. Zayats group in King's College London. I was supported by the cfaed inspire grant for the research stay in King's College London. The simulation results were produced by Dr. Tobias König in Leibniz Institute for Polymer Research Dresden. Some sections of this chapter are based on the paper [A] Gür *et al., "*Self-assembled plasmonic waveguides for excitation of fluorescent nanodiamonds.", *arXiv*.1712.09141*,* 2017.[159]

## 5.1 Introduction

The discovery of cathodoluminescence (CL) was in the mid-nineteenth century when the light emission was observed from cathode electron rays that were irradiating on a glass substrate. A familiar example, CL has been used as an emission source for computer monitors and televisions. CL is the inverse process of the photoelectric effect. Light (UV-Vis-IR) is generated when an electron beam is incident on the specimen. Since CL spectra provide detailed information about material features, CL is now a widely used method for the characterization of materials in mineralogy, geology, semiconductor physics, materials science, plasmonics and many other fields.

In addition to EELS, cathodoluminescence imaging spectroscopy has been used to map surface plasmons [115]. Compare to the EELS signal, CL signal is often much weaker, which is limiting when the good signal-to-noise ratio is necessary to resolve multi spectral features. However, CL has some benefits, since there is no need to collect transmitted electrons, it can be performed in scanning electron microscopes (SEMs) and allows to work with thick samples. There are several studies that used this technique for mapping surface plasmons over the last decade, some examples, for gold Yagi-Uga antennas [203], gold nanorods [204], gold nanodecahedras [205] and in Fabry-Perot gold resonators [206].

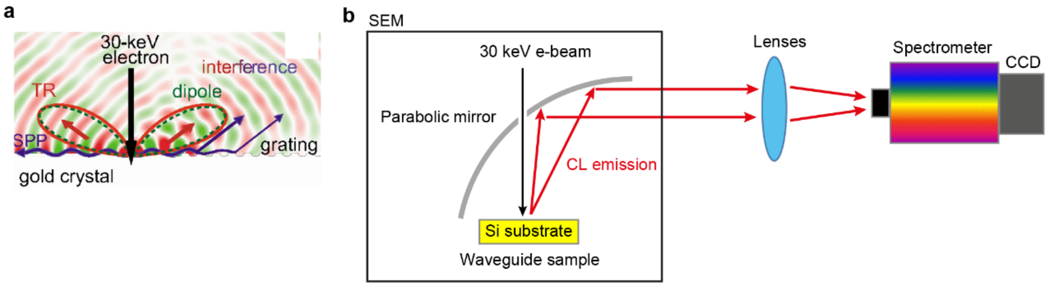

***Figure 5.1 | Schematic overview of electron beam interaction with gold crystal and SEM-CL measurement setup.*** *(a) Schematic of an electron beam impacting on a gold surface, generating surface plasmon polaritons (SPPs) and transition radiation (TR). The background shows the interference pattern of SPPs outcoupled by a grating. (b) A 30 keV electron beam passes through a hole in a parabolic mirror and irradiates the sample, producing cathodoluminescence signal. The photons emitted into the far-field are collected by a parabolic mirror and directed into the CL detector, which contains a spectrometer with a CCD camera. The electron beam is scanned across the sample, with the CL spectrum collected at each excitation position. Panel (a) reproduced from [206].*

Figure 5.1a shows electron beam interaction with the gold surface. The electron beam excitation generates transition radiation (TR) and surface plasmons propagation. SPs and TR emission are coherent, and when the plasmonic modes are converted to free space light, that is by scattering from a grating, in the far field where the CL detection takes place [207]. Because the electron beam excitation is highly localized, it acts like a large range of optical wave vector and induces efficient coupling with SPs which scatter to the far field as a CL signal.

The main component of cathodoluminescence imaging spectroscopy system is the SEM which includes electron source and allows imaging with the aid of secondary and backscattered electrons, see Figure 5.1. The electron source provides beam currents in the nA regime which is required to produce detectable CL intensities. The generated CL signals are collected by a parabolic mirror which redirects the CL signals to the spectrometer and CCD with the help of the lenses.

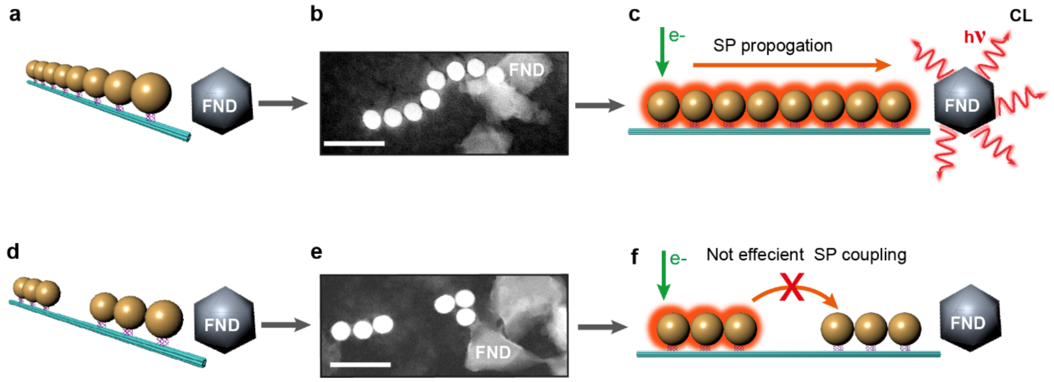

***Figure 5.2 | Overview of self-assembled DNA origami-based plasmonic waveguides in cathodoluminescence imaging spectroscopy.*** *Schematic representations and corresponding tSEM dark-field micrographs of complete (a, b) and incomplete waveguides (d, e) with a fluorescent nanodiamond in close proximity. Surface plasmons are excited by an electron beam and the plasmons propagating to the FND excite a fluorescence that is being detected (c) by cathodoluminescence imaging spectroscopy. Surface plasmons do not efficiently couple across the large gap. Scale bars, 100 nm.*

In order to understand luminescence properties of the waveguide system and the evolution of the SPs modes, the same complete and incomplete waveguides presented in chapter 4, combined with and without a fluorescent nanodiamond were studied by the SEM-CL system. The waveguide structures were deposited on a silicon substrate and a focused 30 keV electron beam was scanned across the samples with ~15 nm spatial resolution. The energetic electron beam induced an effective dipole that couples to the plasmon modes of the nanoparticles, with the resulting far-field photon emission detected by the CL system, see Figure 5.2.

## 5.2 CL characterization of waveguides

In the first set of experiments, complete and incomplete waveguides without a FND were investigated by the combined SEM-CL system, showing excitation of SP modes at the nanoscale with an electron beam and their propagation along the AuNP chain. SP modes were detected as photons after decoupling as free-space light in the far-field.

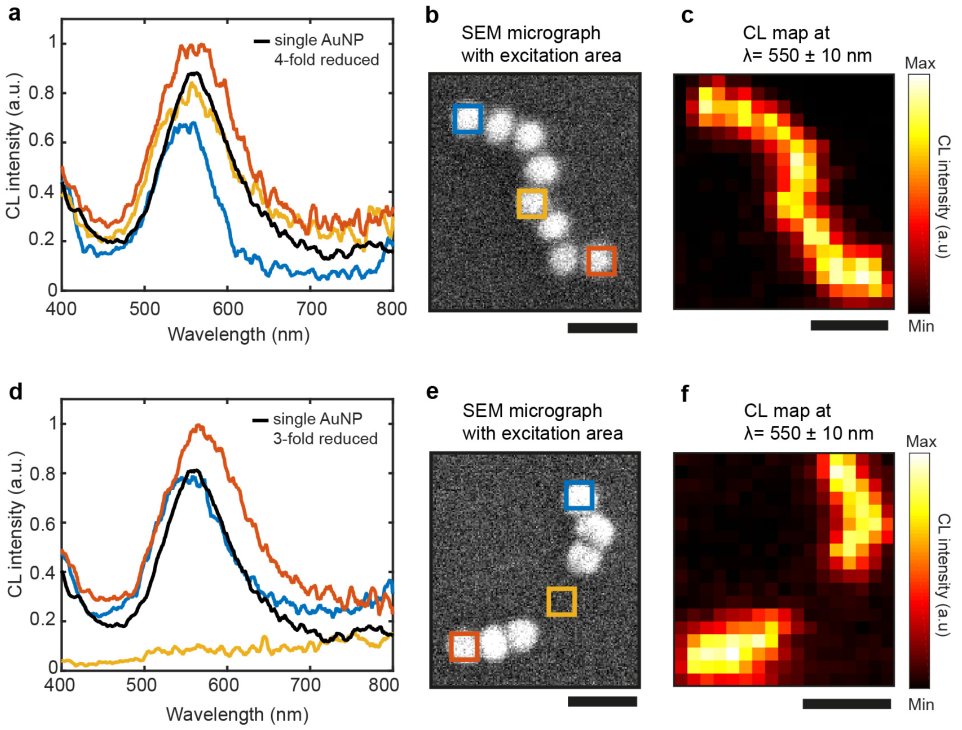

***Figure 5.3 | Cathodoluminescence imaging spectroscopy characterization of a complete and an incomplete waveguides.*** *Experimental CL spectra (a, d) collected from the electron beam excitation locations indicated by the squares in the SEM micrographs (b, e). Spatially-resolved CL maps of the waveguides at the detection wavelength of 550 nm ± 10 nm (c, f), showing CL intensity as a function of electron beam excitation positions (pixel size ~15 x 15 nm). Scale bars, 100 nm.*

Figure 5.3 shows CL spectral and spatial analysis of a complete waveguide and an incomplete waveguide with a gap of ~85 nm between the trimers. Electron beam impact areas are marked by squares in corresponding colors in the SEM micrographs. Spatially resolved CL maps of the waveguides at the detection wavelength of 550 nm ± 10 nm show the CL intensity variations as a function of electron beam excitation locations (in pixels; pixel size ~15 x 15 nm).

The CL spectra show peak maxima at ~540 nm for the complete waveguide and at ~545 nm for the incomplete waveguide which correspond to the T modes of the respective waveguides. As it was seen in EELS, the transverse mode is blue shifted compared to the single particle resonance energy, which has a peak maxima at ~557 nm (see also Figure 5.4a). Observation of larger blue shift in complete waveguides could be an indication of efficient SP coupling over the eight particles, and the less blue shift in the incomplete waveguide can be attributed to SP coupling of three particles.

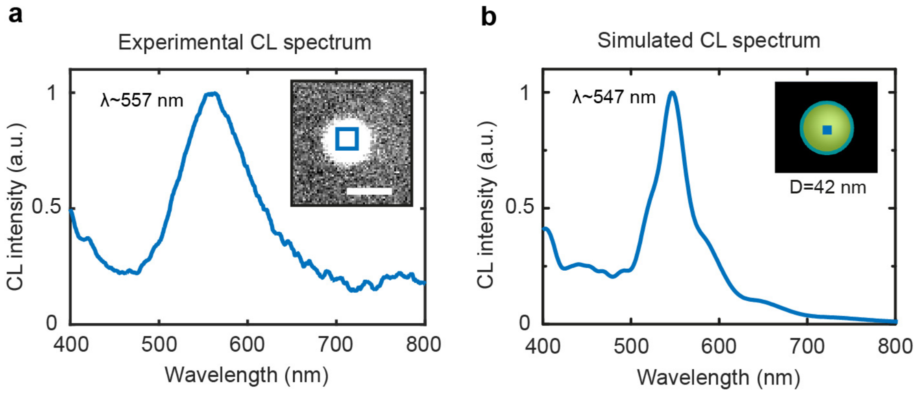

***Figure 5.4 | Cathodoluminescence spectroscopy characterization of a single AuNP.*** *(a) Experimental CL spectrum of a single AuNP, acquired at electron beam excitation location indicated by the blue square in the SEM micrograph inset. Scale bar, 50 nm. (b) Simulated CL spectrum of a single AuNP, where single electron beam excitation at the center, as indicated by a blue dot in modeled image. The size of AuNP is 42 nm.*

The variations of the CL intensity in CL map at 550 nm depending on electron beam excitation locations can be interpreted as a sign of the excitation of different SP modes or exciting the same SP mode with different intensities. Unfortunately, resolving neighboring spectral features from the CL spectra is difficult due to the low signal-to-noise ratio. In order to classify the SP modes, finite-difference time-domain (FDTD) simulations were used for modeling. The same complete waveguide which is presented in Figure 5.3a was modeled.

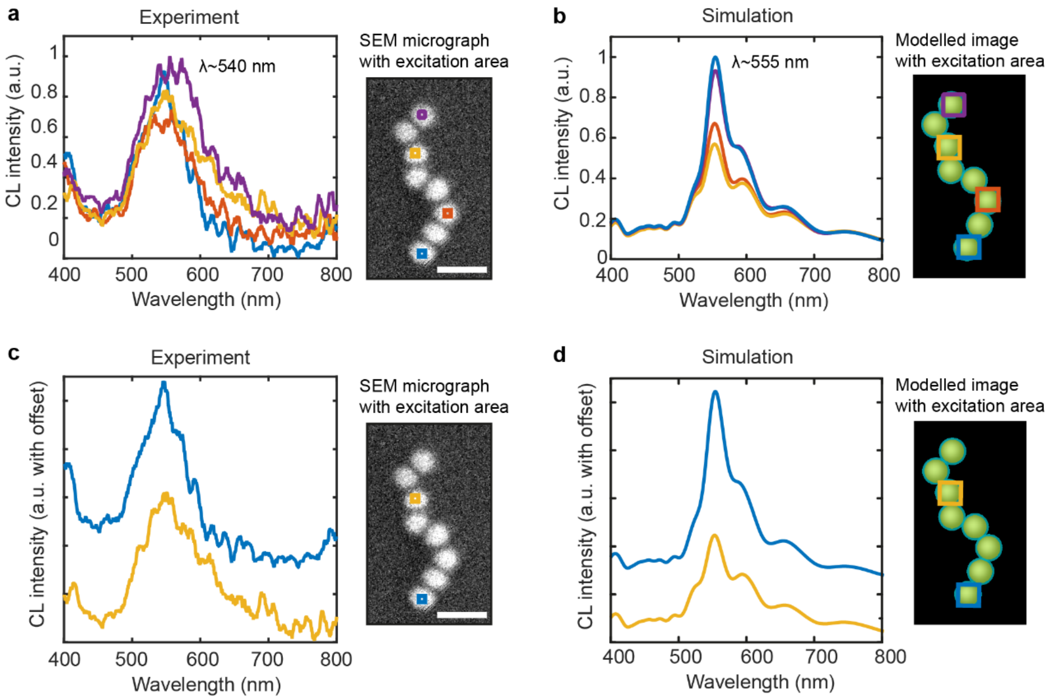

***Figure 5.5 | Cathodoluminescence experimental and simulation spectral analysis of complete waveguide.*** *Normalized experimental CL spectra of a complete waveguide taken at a single pixel (not averaged over several pixels) (a, c). FDTD simulation of normalized CL spectra of the same complete waveguide (b, d). Electron beam excitation locations are indicated by the squares in corresponding colors in SEM and modeled image. Scale bars, 100 nm. This is the same structure as in Figure 5.3a.*

Figure 5.5 depicts experimental and simulated CL spectra of a complete waveguide measured at different electron beam excitation positions in the AuNPs chain. Averaging pixels can give rise to a sum of different modes and change neighboring spectral features. For this reason, single pixel analysis was used in experimental CL spectra instead of smoothing the data by binning every two or three wavelength measurement. In both experiment and simulation, CL intensities are higher in excitation of end particles (blue and purple) than the excitation of particles in between (red and yellow). Although the experimental spectra are still noisy (in Figure 5.5c), they quite resemble modeling spectra with slight differences at the maximum peak. The differences come from the particle sizes and inter-particle distance since the particles were assumed perfectly spherical with 42 nm in diameter and 2 nm spacing between the particles in the simulations.

The highest peak is measured at 540 nm in the experiment and at 555 nm in simulation; these can be interpreted as transverse modes of the waveguide. Unlike single particle CL spectra (in Figure 5.4) where one clear peak for single particle resonance was detected, additional peaks and shoulders were observed in complete waveguide CL spectra. As the dark modes cannot radiate to the far-field and cannot be detected in CL spectroscopy, those additional peaks can be interpreted as a feature of the higher order bright sub-modes.

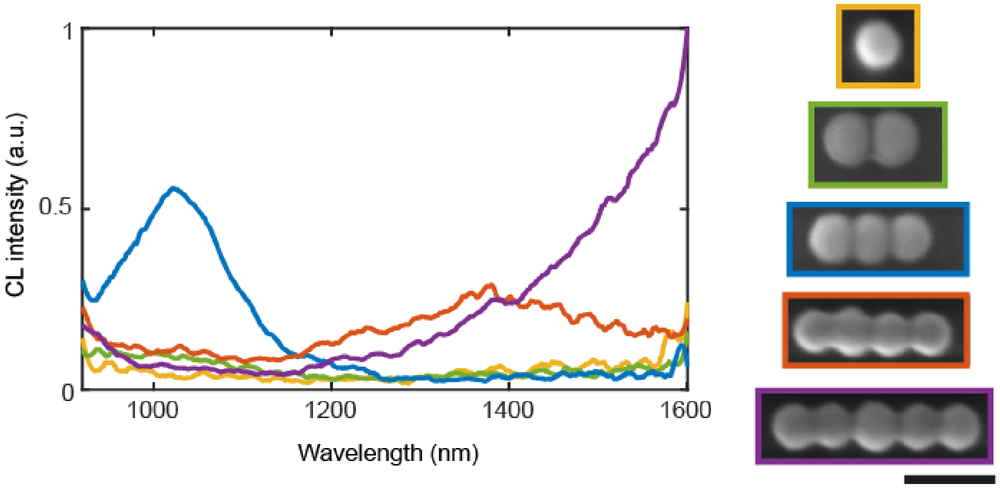

***Figure 5.6 | Cathodoluminescence spectral analysis of single particle to five particle chain in the infrared region.*** *Averaged and normalized CL spectra of single to five AuNPs chain, each spectrum is color indicated by squares in corresponding colors in SEM micrographs. AuNPs are ~45nm in diameter with less than 1 nm inter-particle spacing. Scale bar, 100 nm.*

Since the lowest energy L1 mode (super-radiant bright mode) was detected in infrared regime in EELS study, L1 mode could not be detected in the visible regime in the CL measurements. To confirm this, CL spectra of 1-5 AuNPs series were measured with an infrared detector. The averaged CL spectra show the gradual redshift of the super-radiant mode in the infrared when the particle number is increasing in the chain, see Figure 5.6. The CL signals from the single and dimer particles are not seen since single particle plasmon resonance peak was observed in the visible region and dimer AuNPs should also radiate in the visible region. Here slightly bigger AuNPs (~45nm) were used and the spacing could not be estimated due to the low-resolution SEM imaging. However, from the continuous large shift, one can interpret that particles are extremely close and they show rod-like behavior resulting from strong plasmon coupling over the particles or particles might be fused as it was the case in EELS. Although, the particles in SEM images seem to be fused, the particles were not initially fused, but high-dose imaging with the electron beam could initiate the fusing process. The fusing in the CL can be more drastic compared to the EELS, because of the very thick substrate and thus the electron beam interaction volume is much larger than that of the thin silicon nitride substrate. Moreover, fusing can happen both during imaging and measurement.

## 5.3 Energy transfer through a plasmonic waveguide

In order to facilitate experimental observation of SPs propagation through waveguides, a reporter particle is required as an emitter that SPs can couple to it. For this, organic fluorophores, quantum dots, and fluorescent beads were tested as reporter particles. However, their emission drastically changes and their corresponding spectra deviates due to the vacuum environment and high-energy electron beam irradiation. As these reporter particles are not sufficiently stable, nitrogen-vacancy (NV) color center fluorescent nanodiamonds (FNDs) were employed, since they are extremely photostable, bright and relatively invariant to the chemical and physical environments and are therefore the best option for electron microscopy studies.

Since FNDs have excellent optical properties, they have been used for thriving applications in photonics [208], [209], including quantum computing [210], quantum information technology [211], quantum optics [212], coupling to plasmonic nanostructures [213]–[216], fluorescence nanoscopy [217], bioimaging and biosensing [218]. The NV center is a point defect formed in the diamond lattice by substituting a nitrogen atom and adjacent lattice vacancy. NV centers exhibit neutral $NV^0$ and negative $NV^-$ charged states, which have zero-phonon lines (ZPLs) of 575 nm and 637 nm, respectively [219].

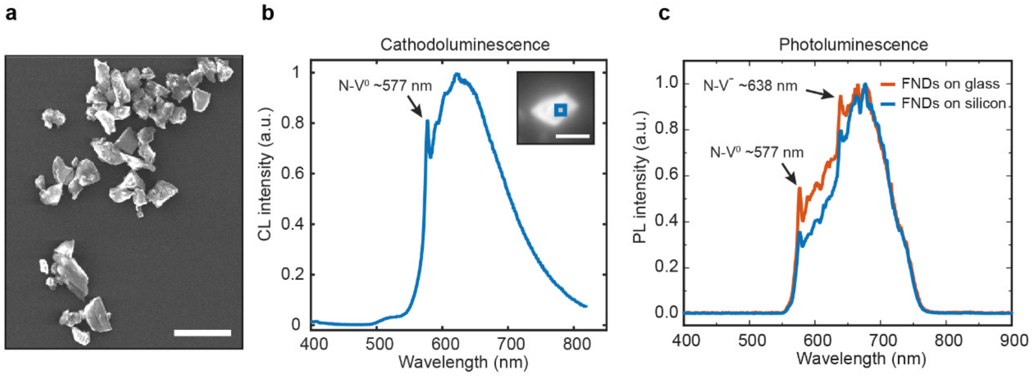

***Figure 5.7 | Characterization of fluorescent nanodiamonds.*** *(a) SEM micrograph of the FNDs. Scale bar, 500 nm. (b) Normalized CL spectrum of a single FND with ZPL for* $NV^0$ *at 577 nm, inset SEM micrograph showing electron beam excitation location by the blue square. Scale bar, 100 nm. (c) Normalized PL emission spectra of FNDs solution on glass (red) and the silicon substrate (blue) with ZPL lines for* $NV^0$ *at 577 nm and for* $NV^-$ *at 638 nm.*

First, the luminescence properties of FNDs were analyzed by CL spectroscopy and photoluminescence (PL) spectroscopy. Figure 5.7 shows CL spectrum of a single FND with a characteristic of ZPL peak at 577 nm for $NV^0$ after electron beam excitation. The same CL result of FNDs was obtained as in previous reports [220], [221]. PL spectra were taken for FNDs solution on silicon and glass substrates after laser excitation. On both substrates, PL spectra show ZPLs at 577 nm and 637 nm for $NV^0$ and $NV^-$, respectively.

Next, SP propagation through a waveguide which couples to a FND and detection of the FND's emission were demonstrated, realizing nanoscale frequency conversion. Here in Figure 5.8, isolated complete and incomplete waveguides were combined with a single FND and CL measurements were performed. CL spectra were taken at electron beam excitation areas indicated by squares in corresponding colors in SEM micrographs. Since the transverse mode is dominant at 550 nm and FND emission is dominant at 600 nm, CL maps at the detection wavelength of 550 nm and 600 nm (± 10 nm) were spatially resolved. In complete waveguide with a FND system, SP propagation couples to $NV^0$ center by exciting any position in the waveguides including particle number 8 (furthest), which is about 350 nm away from FND. Lower CL signal was observed, when the electron beam is directly incident on the silicon.

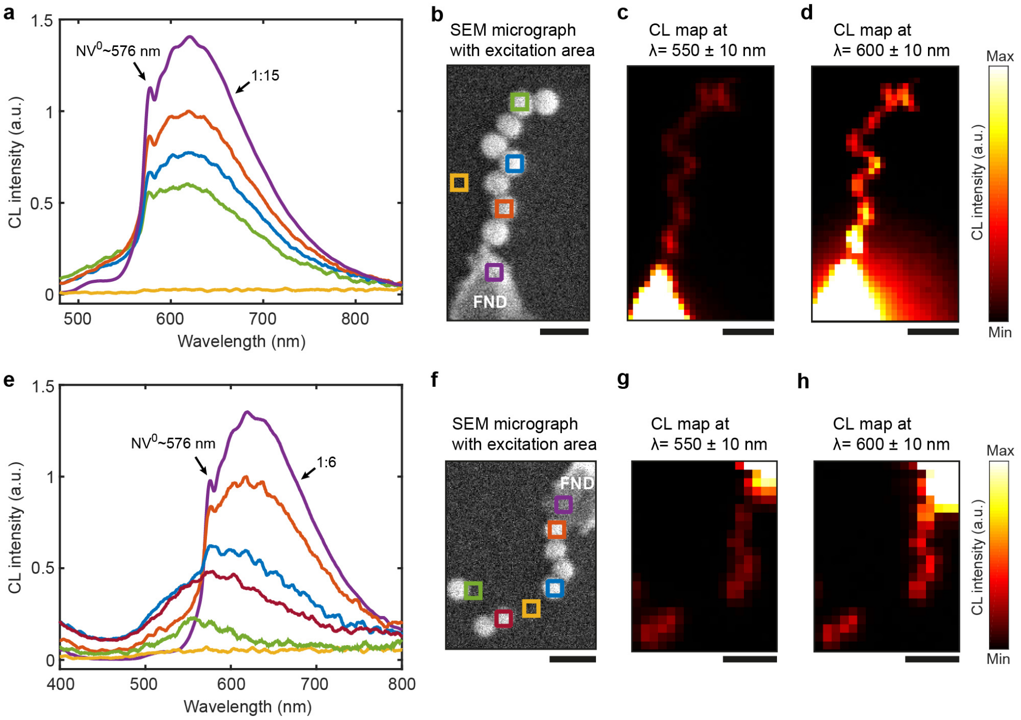

***Figure 5.8 | Energy transfer through plasmonic waveguides.*** *Cathodoluminescence (CL) spectra when illuminating waveguides adjacent to a fluorescent nanodiamond (FND). The CL spectra of the complete (a) and incomplete (e) waveguides taken at electron beam excitation locations indicated by squares in the corresponding colors in the SEM micrographs (b, f). The intensity of the FND emission under direct e-beam illumination (purple) is reduced 15-fold (a) or 6-fold (e) for clarity. Spatially resolved CL maps at the detection wavelengths of 550 nm (± 10 nm) (c, g) and 600 nm (± 10 nm) (d, h), show CL intensity as a function of electron beam excitation positions. Scale bars, 100 nm.*

Since the excitation energy needs to be higher than the emission energy of the $NV^0$ center (shorter than 577 nm), only higher energy sub-modes (bright and dark) or transverse mode are responsible for exciting the $NV^0$ centers. The broad T mode observed by CL spectroscopy (see Figure 5.3) is energetically overlapping with the FND absorption at ~550 nm, which is necessary for an efficient energy transfer from the waveguide to the FND. Importantly, the energy propagation of SP modes is maximized at the transverse mode [100]. The L modes (L: 1, 2, 3…) in principle also allow the energy propagation when the waveguide is excited at one particle [197], but energies of the lower L modes (in the infrared) are too low to excite the FND.

In the CL map at 600 nm, CL intensity variation with the electron beam excitation positions can clearly be seen even within individual particles, and the intensity decay is not proportional to the inverse square of the distance between electron beam excitation position and the FND. This variation pattern in CL map reveals that the high energy dark or bright modes couple to $NV^0$ centers, not T mode alone. For example, particle number 8 has higher CL intensity than particle number 4 or particle number 7 has almost the same intensity with particle number 3, see Figure 5.9.

To confirm that actual SP modes are coupling to the FND and not random scattering effect, the incomplete waveguide with a FND was analyzed as a negative control in Figure 5.8e. In contrast to the complete waveguide, spectral differences between different electron beam excitation locations were observed. The first particle (closest to the FND), red spectrum, excites the FND and exhibits clear ZPL peak, the particle number 4 (blue spectrum) excitation still shows ZPL peak but the spectrum gets broader. This is due to the combination of transverse mode and less intense FND emission. There are possibly two reasons for this. First, the SP modes in 4-AuNP waveguide fragment have different energies than those of the 8-AuNP complete waveguide and these modes couple to the FND with lower efficiency. The second reason, since each FND is not identical, it can also be that the dipole NV center(s) of this FND is not aligned properly to the modes of the 4-AuNP fragment, resulting in lower CL signal.

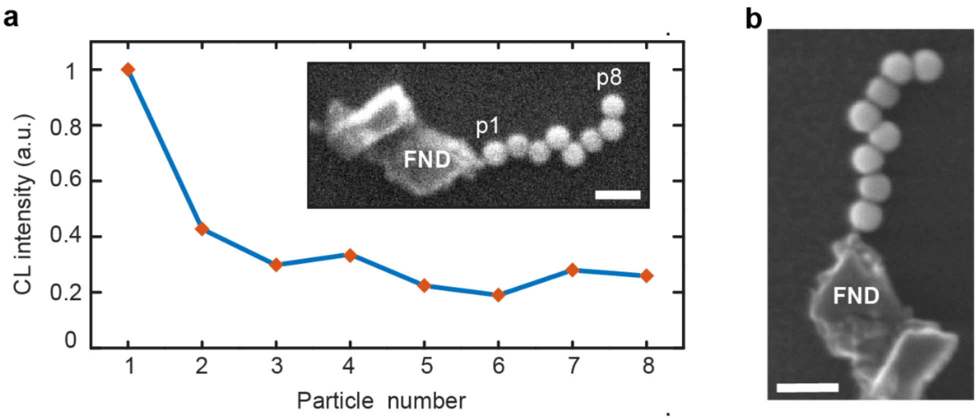

***Figure 5.9 | Cathodoluminescence intensity plot of the fluorescent nanodiamond at the wavelength of 576 nm ($NV^0$) as a function of excitation position in the complete waveguide.*** *CL plot shows the ~ four-fold intensity decay of the FND emission over the length of the waveguide (~350 nm) (a). A high-resolution SEM micrograph of the same waveguide with a FND (b), taken after the CL measurement, which confirms that the waveguide structure is still intact. The data are from Figure 5.8a. Scale bars, 100 nm.*

The ZPL peak in the CL spectrum was not observed anymore when exciting the residual AuNP dimer beyond the ~82 nm gap (Figure 5.8e). This might be due to the excitation of these 2-AuNP and 4-AuNP fragments modes with the electron beam is weaker than excitation of the complete waveguide modes. The broad CL spectrum of the dimer shows a peak maxima at ~570 nm. This can be either super-radiant mode (L1) of the dimer or combination of transverse mode and emission of the weakly coupled FND. The contribution from the FND is not clear here. There is also single isolated AuNP which is believed to have detached from the incomplete waveguide during sample preparation or drying process. This AuNP is ~230 nm away from the FND, and the emission spectrum (green) shows single particle resonance energy at ~560 nm, same energy which was observed for the single particle CL signal, see Figure 5.4a.

Since there was no possibility to measure sequential CL spectra of the same waveguide structures with and without a FND (before and after combining with the FND), it could not be estimated which SP modes are exciting the FND from the experimental results, because FNDs emission dominates the overall spectra. Therefore, the experimental results in Figure 5.8 were modeled to investigate how the CL spectra look like without a FND.

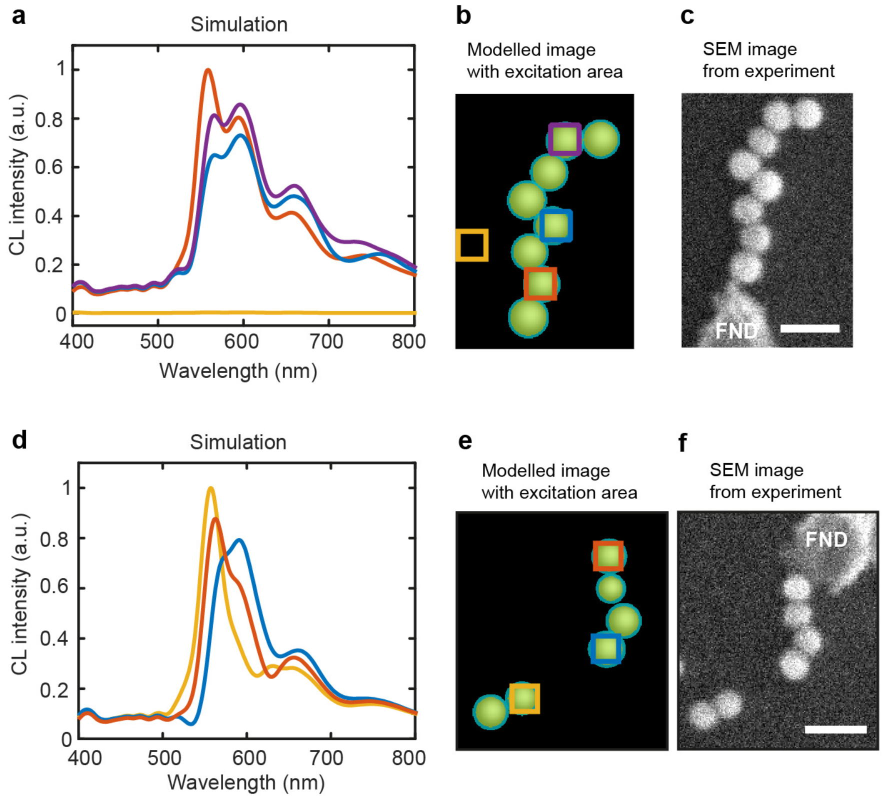

***Figure 5.10 | Finite-difference time-domain simulations of normalized CL spectra of a complete and an incomplete waveguides without a fluorescent nanodiamond.*** *Simulated CL spectra (a, d) are collected from the electron beam excitation locations are indicated by the squares in corresponding colors in modeled images (b, e). Simulated SEM micrographs (c, f) from experiments in Figure 5.8. Scale bars, 100 nm.*

Figure 5.10 depicts the FDTD simulations of complete and incomplete waveguides CL spectra, taken at the electron beam excitation positions indicated in the modeled image. Here it was assumed that there is no FND in the vicinity of the waveguides. For the complete waveguide, the similar results were obtained with slight deviations as it was seen in Figure 5.5. The slight differences come from particle orientation and different electron beam excitation locations. The T mode was observed at the same energy level around 557 nm, and higher order longitudinal sub-modes were observed at the ~750, 659, and 596 nm. Moreover, one small shoulder was detected at ~525 nm (especially when the middle particles were excited, indicated by blue spectrum, same in Figure 5.5), this might be even highest energy sub-mode that could be detected. As expected there is no significant CL signal, when electron beam excitation is on the silicon background, indicated by yellow spectrum.

Since the CL intensity varies for each SP modes depending on electron beam excitation positions, this can explain why FND emission variations were observed at different particle excitations in Figure 5.9. One should also take into account that in CL spectroscopy only the bright modes can be detected. Higher energy dark modes, since they have very low radiative losses, might also be responsible for the FNDs emission and the contribution of the dark modes was indirectly observed from the emission of FNDs.

For the incomplete waveguide simulation (Figure 5.10d), spectral differences compared to complete waveguides were observed. For example, T modes are at different energies for dimer (yellow) and tetramer AuNPs (blue and red) as expected. The bright mode at 596 nm disappears for the dimer. Blue and red spectra vary for T and other sub-modes due to the orientation of particles in the chain. This can explain why blue spectrum gets broader even though it can excite the FND in Figure 5.8e.

Further control experiments were performed with free AuNPs in the vicinity of FNDs. In Figure 5.11, the CL spectra of the single isolated AuNPs with a FND with emitter-to-particle gaps of ~85 nm (a) and ~160 nm (e) shows spectrum (blue) with a maximum at 563 nm and 555 nm, respectively. They show the same spectrum with plasmon resonance of single AuNP without a FND around it (in Figure 5.4a). The CL maps also reveal the same indications, at 550 nm AuNPs have higher CL intensities than FNDs, and at 600 nm FNDs have higher intensities than AuNPs. These results clearly conclude that no coupling to the FND takes place if a AuNP is ≥ ~85 nm away from the FND.

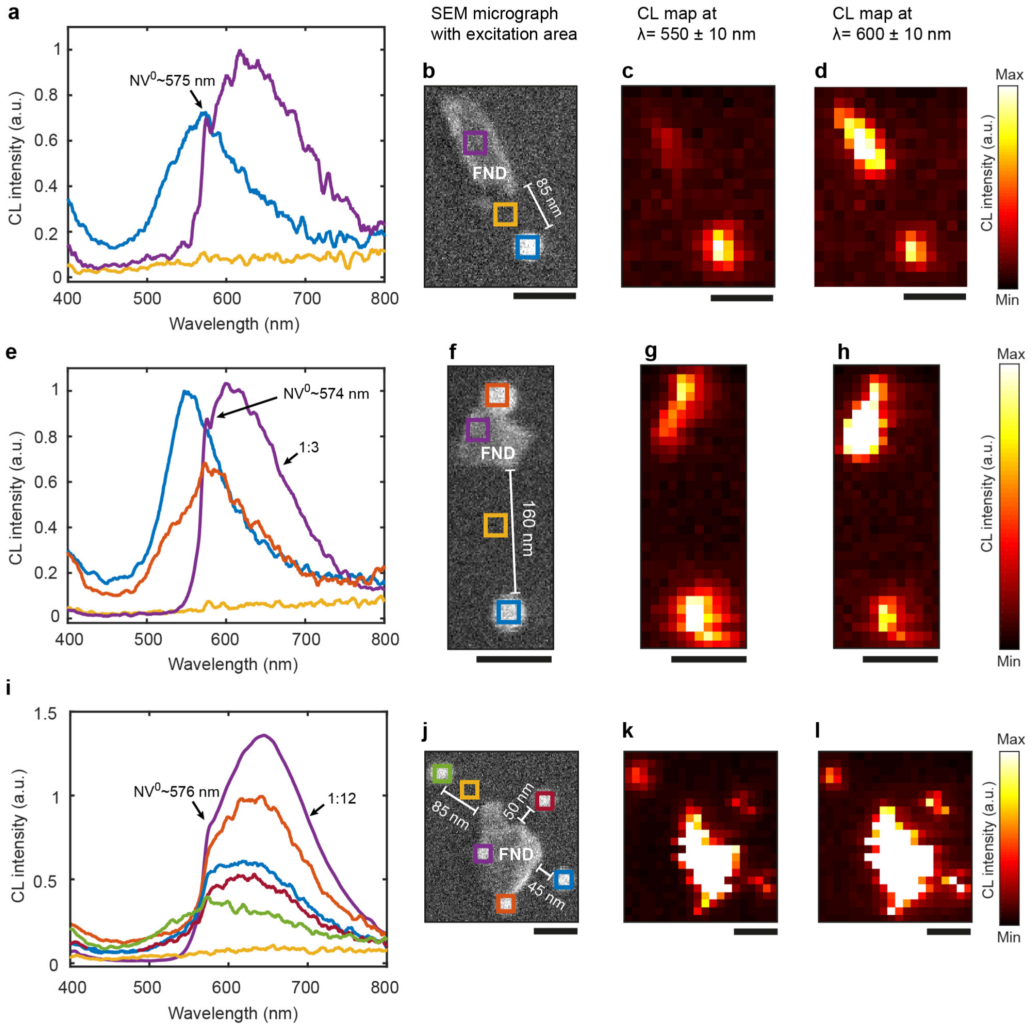

*Figure 5.11 | **Cathodoluminescence imaging spectroscopy measurements of single gold nanoparticles adjacent to a fluorescent nanodiamond.** CL spectra where the emitter-to-particle gaps are ~85 nm (a) and ~160 nm (e), and where five particles are scattered around a FND with distances between 0-85 nm (i). The spectra are taken at electron beam excitation locations indicated by squares in corresponding colors in the SEM micrographs (b, f, and j). The intensity of the FND spectra (purple) is reduced by 3-fold (e) and 12-fold (i) for clarity. Spatially resolved CL maps at the detection wavelength of 550 nm (± 10 nm) (c, g, k) and 600 nm (± 10 nm) (d, h, l), showing CL intensity as a function of electron beam excitation positions (in pixels). Scale bars, 100 nm.*

Figure 5.11c shows CL spectral and spatial analysis of five single particles randomly distributed in the vicinity of a FND with distances between 0-85 nm. The purple spectrum is taken from the AuNP on the FND and shows the highest intensity of FND emission, the red spectrum is taken from the AuNP sitting next to the FND without spacing, the other three AuNPs with the distance of 45, 50 and 85 nm far. The CL intensity of $NV^0$ is gradually decreases when the inter-particle distance is increasing. The spectra are blue shifted when the distance between AuNPs and FND is increasing, hence the spectrum is approaching the single particle resonance energy. The results reveal that single AuNP needs to be close enough (at least a few 10 nm) to the FND for efficient excitation of the FND.

## 5.4 Comparison between CL and EELS results

It is important to understand the differences and similarities between CL and EELS measurements. The EELS measurements deal with the "extinction" properties of a plasmonic structure, i.e. sum of absorption and scattering. However, CL measures radiative losses, thus deals with only scattering properties. In this thesis, the absolute values of CL and EELS in the figures were not compared, since the system responses, currents, integration times, etc. of the two measurements are different. The results presented in figures have been normalized, so one can only compare the spectral shapes. Furthermore, the differences between CL and EELS spectra come from employing different substrates, specifically thick silicon substrate for the CL measurements, which has a refractive index of approximately $n \approx 3.5$ [222] and thin silicon nitride for the EELS measurements, which has a refractive index of approximately $n \approx 2.1$ [223].

## 5.5 Concluding remarks

In this chapter, single AuNPs, complete and incomplete waveguide systems with and without FNDs were investigated both in experiments and simulations. The SPs modes and coupling to the FND were analyzed by cathodoluminescence imaging spectroscopy. The results reveal that the efficient coupling of SPs modes to the FND could be seen in uninterrupted AuNPs chain (complete waveguide) and this is dependent on electron beam excitation location resulting in exciting different sub-modes which are responsible to the FND emission. In contrast, incomplete waveguides and isolated single AuNPs are not able to efficiently excite the FND. Effective coupling from a AuNP to a FND is only possible through gaps smaller than a few 10 nm. The waveguide system presented here can confine different energies at nanoscale volume with SP modes and can be used as a nanoscale light source for the applications from the sensing to energy transport at the nanoscale.

## 5.6 Materials and Methods

**Waveguide assembly.** CTAC capped ~42 nm and ~45 nm AuNPs were synthesized and functionalized as described in chapter 4. The same complete and incomplete 6-HBs designs were used and the waveguides were assembled and purified as in chapter 4.

**CL sample preparation.** Silicon wafer pieces were used as substrates and were plasma treated for 10 min. Next, 20 µL poly-L-ornithine solution (0.01%) was applied and incubated for 30 s. The substrate was then rinsed with ultrapure water. After removing the excess solution with a filter paper, 10 µL of waveguide sample solution was applied and incubated for 2 min. After that, the substrate was dried with a compressed air flow. For the waveguides with FNDs samples, after the waveguide deposition on the substrate, 10 µL of FND solution (FND in DI ultrapure water, high brightness 3.0 ppm NV, 0.1 wt%, 100 nm average particle size, Adámas Nanotechnologies) was applied and incubated for 2 min. Finally, the substrate was dried with a flow of compressed air.

**CL measurements and analysis.** The CL measurements were performed using a Tescan-SEM Delmic-CL setup. A focused 30 keV electron beam was scanned across the samples, which served as a nanoscale broadband source. The energetic electron beam induced an effective dipole that excited the nanostructures, with the resulting far-field emission collected by a parabolic mirror and directed into a spectrometer. The electron beam was scanned across the sample with a ~15 nm pixel size, 1.12 nA current and a 10 µs dwell time. Exposure times ranged between 200 and 300 ms. To remove background CL signal originating from the silicon, reference measurements, taken from the exposed substrate, were subtracted.

The spectra were normalized, taking into account the spectral sensitivity of the system, and averaged over three pixels unless otherwise stated. Spectral filtering was carried out with a Savitzky-Golay function in MATLAB.

**FDTD simulation.** A commercial-grade simulator based on the finite-difference time-domain method was used to perform the calculations (Lumerical Inc., Version 8.16.1022) [224]. For the broadband and single mode excitation, a dipole source was used for the specific wavelength range (short pulse length of 3 fs) and single wavelength (long pulse length between 14 fs and 20 fs), respectively. The electron beam is represented by a series of dipoles with a phase delay that is related to the electron velocity. An electron velocity with 20% of the speed of light and a dipole spacing of 15 nm was used. As boundary conditions, perfectly matched layers were used in all principal directions. Nanoparticle diameters, inter particle distance and materials constants were obtained from experimental studies. For the simulation ($\lambda = 400\ldots1000$ nm), the FDTD software approximates the refractive index indices of the materials by using a polynomial function. All optical constants were estimated by curve-fitting with a root mean square error below 0.21. For gold, the experimental data by Johnson and Christy [202] were used. A silicon layer with refractive index data from Palik [225] was used as a substrate. Zero-conformal-variant mesh refinement and an isotropic mesh overwrite region of 1 nm were used. All simulations reached the auto shut-off level of $10^{-5}$ before reaching 150 fs of simulation time.

**PL measurements.** For photoluminescence studies, the FND solution (Adámas ND-NV-100nm) was diluted in ultrapure water to a concentration of 0.2 mg/mL. A 20 µL of the diluted FND solution was then drop cast onto the glass and silicon substrates. The PL measurements were performed on an inverted microscope equipped with a spectrometer (Ocean Op-tics, QE Pro). A 532 nm excitation wavelength from a Fianium super-continuum laser was chosen. The laser beam was focused onto an FND using an Olympus 100x 0.9NA microscope objective. The photoluminescence signal was then collected via the same objective. Several filters (Thorlabs DMLP 567 and FELH 550) were used in order to prevent any contribution from the excitation light to the collected signal.

# 6 CONCLUSION AND OUTLOOK

In conclusion, this thesis has been concerned with the direct observation of energy transfer through a self-assembled plasmonic waveguide for the use of short-distance high-speed optical communication in the integrated optoelectronics. Experimental techniques EELS and CL have been used to study coupled surface plasmon modes and to detect energy propagation through eight AuNPs over a distance of 350 nm to a FND. With this, nanoscale energy conversion has been realized and the self-assembled waveguide has been used as a nanoscale light source to excite the FND. Sub-50 nm electromagnetic field confinement has been demonstrated which is not achievable with stripe and silicon waveguides. The critical factors for the effective waveguiding are highly monodispersed and monocrystalline metal nanoparticles, close inter-particle spacing down to 1-2 nm. These are not possible by top-down methods and these have been achieved by DNA origami templated self-assembly method. The combination of finely controlled, highly scalable self-assembly method (DNA origami), multi-particle based plasmonic systems with closest inter-particle spacing (1-2 nm) and near-field spectroscopy techniques, for the first time, has been realized in this thesis.

Specifically, in chapter 3 the assembly yield and AuNP binding occupancy have been investigated as a function of parameters including the ionic strength, stoichiometric ratio, oligonucleotide linker chemistry, and the assembly kinetics by analyzing electron micrographs with an automated image analysis tool. A binding occupancy of up to 98.7% has been achieved with the optimized assembly protocol, which the enabled robust and reliable production of the waveguides. An attachment of AuNPs with selectable sizes in the range between 17 and 60 nm has been shown. Furthermore, heterogeneous assemblies have been realized by attaching Qdots to the waveguides and monomer waveguides have been interconnected by designing interfaces on the 6-HB DNA origami nanotubes. The length of the waveguide has been extended up to 1.2 micron.

In chapter 4, the coupled SP modes that support waveguiding have been systematically studied in both complete and incomplete waveguides by EELS. The nature and distribution of the SP modes have been spatially resolved in the experiments and shown to be in excellent agreement with simulated EELS results. The effect of the inter-particle spacing over the SP coupling has been investigated by finely tuning the inter-particle spacing with an increasing particle diameter at a constant distance between binding sites. High-resolution energy mapping of the waveguide assemblies by the spectral and spatial EELS probing have shown multiple coupled bright and dark SP modes which range from the visible to infrared spectral regions.

In chapter 5, the luminescence properties of single AuNPs, complete and incomplete waveguide systems with and without FNDs have been studied by cathodoluminescence imaging spectroscopy. The energy propagation through a waveguide to the FND has been experimentally shown. The results have revealed that the efficient coupling of SPs modes to the FND could be seen in the complete waveguide, while incomplete waveguides and isolated single AuNPs are not able to efficiently excite the FND. The self-assembled waveguide presented in this thesis can confine the energy at different frequencies to nanoscale volume with SP modes and can be used as a nanoscale light source for the applications from sensing to energy transport at the nanoscale.

## 6.1 Outlook

In this thesis, it was not possible to directly attach FNDs to the waveguides. FNDs can be functionalized with orthogonal oligonucleotides and can be attached to the terminal position on the 6-HBs by introducing a specific binding site, as it has been shown for the attachment of Qdots in chapter 3. A principle for the attachment of FNDs to the DNA origami structure is already reported by Zhang *et al.* [80]. Second, the distorted arrangement of particles in the waveguide structure can be straightened into a more linear alignment. For this, a more compact and stiffer DNA origami structure can be designed and monomeric units could be combined to extend for longer waveguides, as the principle of multimerization has already been demonstrated in chapter 3. Other shapes including rods or cubes and other materials including silver or core-shell nanoparticles could be assembled to increase the SP coupling efficiency, and or tune SP modes to different frequencies. Since the FNDs are extremely stable and best option for both electron and optical microscopes, FND-AuNP hybrid structures can be used as a molecular barcode for immunolabeling of cells and tissues by correlative light-electron microscopy (CLEM) method [226]. Finally, potentially self-assembled waveguides presented in this thesis can be precisely positioned and arrayed on silicon wafers [227], [228] and mica surfaces [229] for the integrated optics.

From a theoretical point-of-view, the contribution of different SP modes to the waveguiding can be quantified by electromagnetic modeling. The waveguiding performance and damping factor can be determined by electric field calculations and surface charge calculations. The bright and dark SP modes can be precisely assigned by nature of the SP modes and surface charge distributions. The preliminary results have revealed that the damping factor is around ~3 dB/50 nm, and L2 and L3 sub-modes are the main contributors to the waveguiding. These results shall be included in a manuscript which is currently in preparation, Gür et al. “Self-assembled plasmonic waveguides for nanoscale light propagation”.

# APPENDIX

## A.1 Additional electron micrographs

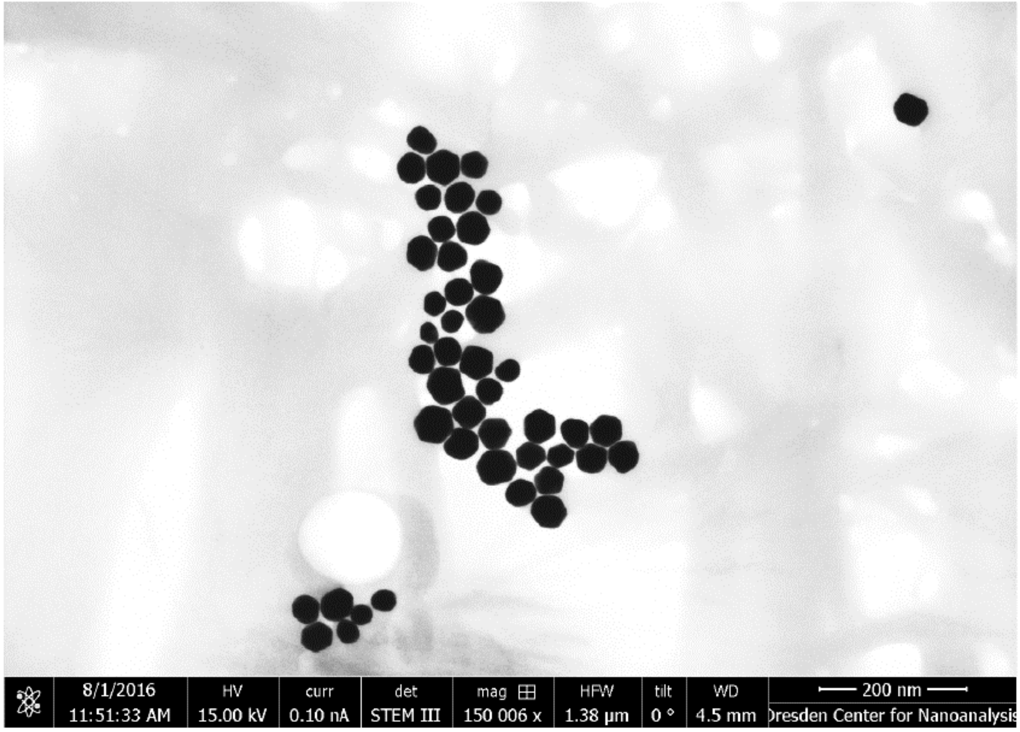

***Figure A.1 | tSEM micrograph of the commercial (from Alfa-Aesar) 40 nm gold nanoparticles with broad size distribution.***

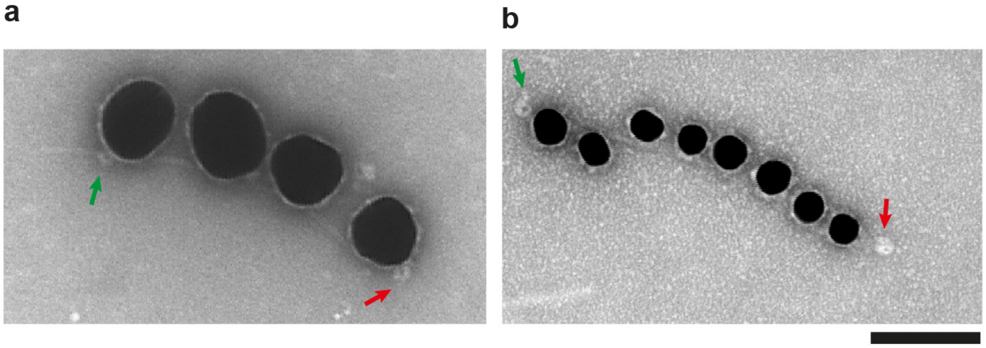

***Figure A.2 | tSEM micrograph of the waveguides with two type of quantum dots attached at the terminal positions.*** *tSEM micrographs of (a) 4 x 56 nm AuNP and (b) 8 x 28 nm AuNP waveguide structures with donor and acceptor Qdots attached at the terminal positions. Green and red arrows indicate donor and acceptor Qdots, respectively. Scale bar, 100 nm.*

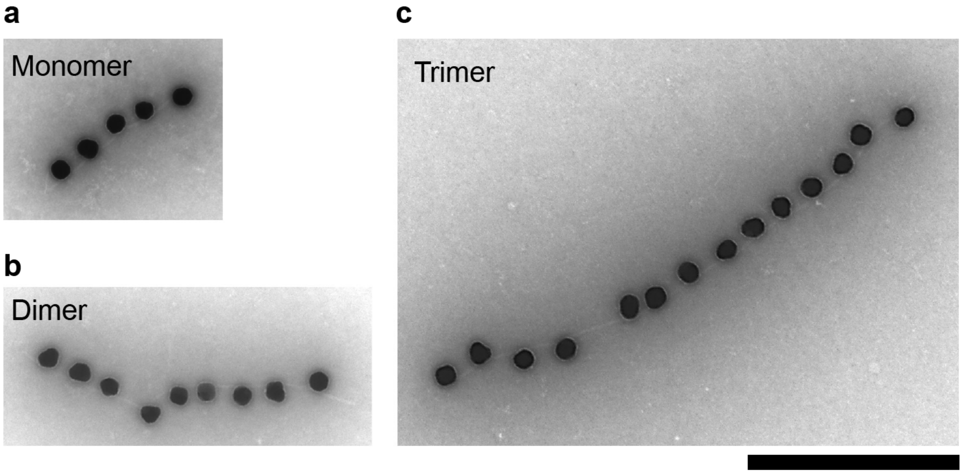

***Figure A.3 | Multimerization of the waveguides with larger AuNPs.*** *tSEM micrograph of the monomer (a), dimer (b) and trimer (c) waveguides with ~45 nm AuNPs. Scale bar 500 nm.*

## A.2 Matlab script for automated image analysis

```matlab
% TEM_ana_v2
%%%%%%%%%%%%%%%%%%%%%%%%%%%%%%%%%%%%%%%%%%%%%%%%%%%%%%%%%%%%%%%%%%%%%%%%%%%
% Copyright 2015/02/26
% Revision: 2
% Written by Friedrich Schwarz
%
% FUNKTION
% Finding end evaluation of Gold particles attached to DNA origami structure
%
% Open a TEM image
%
%
% USING THIS SCRIPT:
% NOTES
%
%
% REQUIRED INPUTS -
% TEM image and setting in put see pop up.
% Last Modified by v2.0 17-March-2015 09:05:05
% Start Script
%%
clear all
close all
% Open images
%
% Add bin path to matlab folder
if ~isdeployed
addpath('bin');
end
disp('Open Image')
% Set path dir via standard GUI interface
[FileName, PathName] = uigetfile2('*.stk;*.zvi;*.tif;*.tiff','Image Stacks');
fullpath = fullfile(PathName,FileName); % Erzeuge full path adress
Gernal_output = [PathName,FileName(1:end-4)];
%Img = StackRead(fullpath);
Img = imread(fullpath);
% Auto determination of Image cut of
if size(Img,1)<2000
cutoffY=1024;
else
cutoffY=2048;
end
% 2.694915254, 1.926, 1.694915254, 1.347
% variables
prompt = {'Pixel size','Event threshold for binary image:', ...
'Cluster filter Area BinRadius (nm)',...
'Object numer min max', 'B(1) or W(0) Imag', 'Img cut off', 'Boundery offset px'};
answer=inputdlg(prompt,'Set variables',1,{'5.412','15000','40', '0 25', '0', num2str(cutoffY), '5'});
data.pixelsize=str2num(answer{1}); % pixel size for 2d histogram binning
data.thresholdValue =str2num(answer{2}); % morphological structuring area for His filter
data.cluthr = ceil(str2num(answer{3})/data.pixelsize);
plotsize=str2num(answer{4});
```

```
data.clust_thr = str2num(answer{4});
data.BW = str2num(answer{5});
data.cutoffY = str2num(answer{6});
data.cutB = str2num(answer{7});
clear cutoffY
radius = data.cluthr*data.pixelsize;
disp([num2str(radius) ' Cluster radius in nm']);
Img = imread(fullpath);
% Auto determination of Image cut of
if size(Img,1)<  2000
data.cutoffY=1024;
else
data.cutoffY=2048;
end
%crope image
data.Img = Img(1:data.cutoffY, 1:end);
%% Start ana
% find Threshold
% create a binary image
if data.BW==1
data.binaryImage = data.Img > data.thresholdValue;
else
%data.Img = abs(data.Img-2^16)
data.binaryImage = data.Img < data.thresholdValue;
end
%data.binaryImage = imfill(data.binaryImage, 'holes');
%data.binaryImage = bwmorph(data.binaryImage,'clean');
%data.binaryImage = bwmorph(data.binaryImage,'majority');
data.labeledImage = bwlabel(data.binaryImage, 8);     % Label each blob so we can make measurements of it
coloredLabels = label2rgb (data.labeledImage, 'hsv', 'k', 'shuffle'); % pseudo random color labels
% Get all the blob properties.  Can only pass in data.Img in version R2008a and later.
data.blobMeasurements = regionprops(data.labeledImage, data.Img, 'all');
data.numberOfBlobs = size(data.blobMeasurements, 1);
% bwboundaries() returns a cell array, where each cell contains the row/column coordinates for an object in the image.
% Plot the borders of all the coins on the original grayscale image using the coordinates returned by bwboundaries.
data.boundaries = bwboundaries(data.binaryImage);
data.numberOfBoundaries = size(data.boundaries);
% fprintf(1,'Blob #      Mean Intensity  Area   Perimeter    Centroid Diameter\n');
% Loop over all blobs printing their measurements to the command window.
for k = 1 : data.numberOfBlobs           % Loop through all blobs.
% Find the mean of each blob.  (R2008a has a better way where you can pass the original image
% directly into regionprops.  The way below works for all versions including earlier versions.)
thisBlobsPixels = data.blobMeasurements(k).PixelIdxList;  % Get list of pixels in current blob.
data.meanInt(k,1) =  mean(data.Img(thisBlobsPixels)); % Find mean intensity (in original image!)
data.meanInt(k,2) =  std(double(data.Img(thisBlobsPixels)));
data.ind(k,1)=k;
data.blobArea(k,1) = data.blobMeasurements(k,1).Area;       % Get area.
data.blobPerimeter(k,1) = data.blobMeasurements(k,1).Perimeter; % Get perimeter.
```

```
data.blobCentroid(k,1:2) = data.blobMeasurements(k,1).Centroid; % Get centroid.
data.blobECD(k,1) = sqrt(4 * data.blobArea(k,1) / pi); % Compute ECD - Equivalent Circular Diameter.
%     fprintf(1,'#%2d %17.1f %11.1f %8.1f %8.1f %8.1f % 8.1f\n', k, data.meanGL, data.blobArea, data.blobPerimeter, data.blobCentroid, data.blobECD(k));
%   % Put the "blob number" labels on the "boundaries" grayscale image.
%   text(blobCentroid(1) + labelShiftX, blobCentroid(2), num2str(k), 'FontSize', fontSize, 'FontWeight', 'Bold');
end
Ana.MeanDotradius(1,1) = mean(data.blobECD)*data.pixelsize;
Ana.MedianDotradius(1,1) = median(data.blobECD);
Ana.MeanDotradius(1,2) = std(data.blobECD)*data.pixelsize;
% filter out to smal objects
data.ndot_trash=zeros(data.numberOfBlobs,1);
data.ndot_trash = (  (data.blobArea > 0) &...
(data.blobArea < 150)) ;
disp([num2str(Ana.MeanDotradius) ' Object radius']);
% Create binary image from particle
x = data.blobCentroid(data.ndot_trash,1);
y = data.blobCentroid(data.ndot_trash,2);
edges{1}=1:1:size(data.Img,1);
edges{2}=1:1:size(data.Img,2);
data.HistogramImage=hist3([y x],'Edges',edges);
data.binaryImage2 = data.HistogramImage > 0;
%% Auto finder
%se=strel('octagon',data.cluthr); %Create morphological structuring element
se=strel('disk',data.cluthr,0);
% clear singel pixel trahole spots
Cluster_bin=imdilate(data.binaryImage2,se); % dilate image
clustmap=bwlabel(Cluster_bin,8); % identify cluster
clustmap_coloredLabels = label2rgb (clustmap, 'hsv', 'k', 'shuffle');
Ana.nclust=max(clustmap(:));
disp([num2str(Ana.nclust) ' cluster found']);
Cluster_boundaries = bwboundaries(Cluster_bin);
Cluster_numberOfBoundaries = size(Cluster_boundaries);
nclust_trash=zeros(Ana.nclust,1);
nclust_trash_Bound=zeros(Ana.nclust,1);
% Filter out boxes with touch bounderies
for k = 1 : Ana.nclust
if (((min(Cluster_boundaries{k}(:,1))>data.cutB) &&...
(min(Cluster_boundaries{k}(:,2))>data.cutB) &&...
(max(Cluster_boundaries{k}(:,1)))<(size(data.Img,1)-data.cutB) &&...
(max(Cluster_boundaries{k}(:,2)))<(size(data.Img,2)-data.cutB) ...
) == 0);
nclust_trash(k,1) = 1;
nclust_trash_Bound(k,1) = 1;
end
end
disp([num2str(sum(nclust_trash_Bound)) 'Trash boundaries']);
%% Determin partical numbers and cluster elements
h1=figure;
%Manuel selection via giput
clf
imagesc(data.Img);
hold on;
```

```
%set(gcf,'units','normalized','outerposition',[0 0 1 1])
title('Outlines, from bwboundaries()'); axis image;
colormap('Gray')
Ana.Clust_ind = cell(Ana.nclust,1);
for k=1:Ana.nclust
if nclust_trash_Bound(k)==1
continue
end
cx = [Cluster_boundaries{k}(:,2)' Cluster_boundaries{k}(1,2)]';
cy = [Cluster_boundaries{k}(:,1)' Cluster_boundaries{k}(1,1)]';
Ana.Clust_ind{k}(:,1) = inpolygon(x, y, cx, cy);
Ana.num_particels(1,k)= sum(Ana.Clust_ind{k}(:,1));
plot(cx, cy, 'r', 'LineWidth', 2);
text(cx(1),cy(1),num2str(k),'Color',[0 0 0])
end
scatter(data.blobCentroid(:,1),data.blobCentroid(:,2),'k.');
scatter(data.blobCentroid(data.ndot_trash,1),data.blobCentroid(data.ndot_trash,2),'b.');
%% Filter for cluster elements
% filter cluster with all three colors
for k=1:Ana.nclust
if nclust_trash_Bound(k)==1
continue
end
if Ana.num_particels(1,k)<=data.clust_thr(1) || Ana.num_particels(1,k)>=data.clust_thr(2)
nclust_trash(k,1)=1;
end
end
disp([num2str(Ana.nclust-sum(nclust_trash)) ' After filter']);
%% Fin eva cluster
for k=1:Ana.nclust
if nclust_trash(k)==1
continue
end
clust_ind = Ana.Clust_ind{k}(:,1);
dx = plotsize;
% Sort data
A=[];
A(:,1)=[1:1:Ana.num_particels(1,k)];
A(:,2)=find(clust_ind);
A(:,3)=(x(clust_ind));
A(:,4)=(y(clust_ind));
% pre sorting
xsum = sum(diff(A(:,3)));
ysum = sum(diff(A(:,4)));
if xsum >= ysum
A= sortrows(A,3);
else
A= sortrows(A,4);
end
%fin sorting
% find start point
loopN = size(A,1);
if find(A(:,3)== min(A(:,3)),1)== find(A(:,4)== min(A(:,4)),1) % min start point
Sort = find(A(:,3)== min(A(:,3)),1);
elseif find(A(:,3)== max(A(:,3)),1)== find(A(:,4)== max(A(:,4)),1)% max start point
Sort = find(A(:,3)== max(A(:,3)),1);% max start point
elseif find(A(:,3)== max(A(:,3)),1)== find(A(:,4)== min(A(:,4)),1)
```

```
Sort = find(A(:,3)== max(A(:,3)),1);% max x miny start point
else
Sort = 1;
end
B(1,:) = A(Sort,:);
xi=A(Sort,3);
yi=A(Sort,4);
A(Sort,:)=[] ;
% sort the rest
for i= 2:loopN
Sort = knnsearch([A(:,3),A(:,4)],[xi,yi],'k',1,'distance', 'euclidean');
B(i,:) = A(Sort,:);
xi=A(Sort,3);
yi=A(Sort,4);
A(Sort,:)=[];
end
A = B;
clear xi yi B loopN
%
A(:,1)=[1:1:Ana.num_particels(1,k)];
Ana.dist{k} = sqrt((A(2:end,3)-A(1:end-1,3)).^2+(A(2:end,4)-A(1:end-1,4)).^2).*data.pixelsize;
Ana.lenght(1,k) = sum(Ana.dist{1,k}(:,1));
Ana.endtwoend(1,k)= sqrt((A(end,3)-A(1,3)).^2+(A(end,4)-A(1,4)).^2).*data.pixelsize;
Ana.meandist(1,k)= mean(Ana.dist{1,k}(:,1));
cx = [Cluster_boundaries{k}(:,2)' Cluster_boundaries{k}(1,2)]';
cy = [Cluster_boundaries{k}(:,1)' Cluster_boundaries{k}(1,1)]';
Ana.Clust_ind{k}(:,1) = inpolygon(x, y, cx, cy);
Ana.num_particels(1,k)= sum(Ana.Clust_ind{k}(:,1));
plot(cx, cy, 'g', 'LineWidth', 2);
end
%% Statistic Value,  percent
Ana.end2endM = mean(Ana.endtwoend(1,Ana.endtwoend>0));
Ana.Meanmeandist= mean(Ana.meandist(1,Ana.endtwoend>0));
Ana.Mlenght = mean(Ana.lenght(1,Ana.endtwoend>0));
Filename_png = [Gernal_output '_Overview_' 'CluAuto' num2str(data.cluthr) '.png'];
print(h1, Filename_png, '-dpng')
clear Img
%% Save stuff
myFileOut = [Gernal_output, '_ANA_auto' answer{3} '.mat'];
save(myFileOut)
```

## A.3 List of staple strands

### A.3.1 The consensus sequence for all common M13-derived clones

```
GCTTGGCACTGGCCGTCGTTTTACAACGTCGTGACTGGGAAAACCCTGGCGTTACCCAACTTAATCGCCTTGCAGCA
CATCCCCCTTTCGCCAGCTGGCGTAATAGCGAAGAGGCCCGCACCGATCGCCCTTCCCAACAGTTGCGCAGCCTGAA
TGGCGAATGGCGCTTTGCCTGGTTTCCGGCACCAGAAGCGGTGCCGGAAAGCTGGCTGGAGTGCGATCTTCCTGAGG
CCGATACTGTCGTCGTCCCCTCAAACTGGCAGATGCACGGTTACGATGCGCCCATCTACACCAACGTGACCTATCCC
ATTACGGTCAATCCGCCGTTTGTTCCCACGGAGAATCCGACGGGTTGTTACTCGCTCACATTTAATGTTGATGAAAG
CTGGCTACAGGAAGGCCAGACGCGAATTATTTTTGATGGCGTTCCTATTGGTTAAAAAATGAGCTGATTTAACAAAA
ATTTAATGCGAATTTTAACAAAATATTAACGTTTACAATTTAAATATTTGCTTATACAATCTTCCTGTTTTTGGGGC
TTTTCTGATTATCAACCGGGGTACATATGATTGACATGCTAGTTTTACGATTACCGTTCATCGATTCTCTTGTTTGC
TCCAGACTCTCAGGCAATGACCTGATAGCCTTTGTAGATCTCTCAAAAATAGCTACCCTCTCCGGCATTAATTTATC
AGCTAGAACGGTTGAATATCATATTGATGGTGATTTGACTGTCTCCGGCCTTTCTCACCCTTTTGAATCTTTACCTA
CACATTACTCAGGCATTGCATTTAAAATATATGAGGGTTCTAAAAATTTTTATCCTTGCGTTGAAATAAAGGCTTCT
CCCGCAAAAGTATTACAGGGTCATAATGTTTTTGGTACAACCGATTTAGCTTTATGCTCTGAGGCTTTATTGCTTAA
TTTTGCTAATTCTTTGCCTTGCCTGTATGATTTATTGGATGTTAATGCTACTACTATTAGTAGAATTGATGCCACCT
TTTCAGCTCGCGCCCCAAATGAAAATATAGCTAAACAGGTTATTGACCATTTGCGAAATGTATCTAATGGTCAAACT
AAATCTACTCGTTCGCAGAATTGGGAATCAACTGTTATATGGAATGAAACTTCCAGACACCGTACTTTAGTTGCATA
TTTAAAACATGTTGAGCTACAGCATTATATTCAGCAATTAAGCTCTAAGCCATCCGCAAAAATGACCTCTTATCAAA
AGGAGCAATTAAAGGTACTCTCTAATCCTGACCTGTTGGAGTTTGCTTCCGGTCTGGTTCGCTTTGAAGCTCGAATT
AAAACGCGATATTTGAAGTCTTTCGGGCTTCCTCTTAATCTTTTTGATGCAATCCGCTTTGCTTCTGACTATAATAG
TCAGGGTAAAGACCTGATTTTTGATTTATGGTCATTCTCGTTTTCTGAACTGTTTAAAGCATTTGAGGGGGATTCAA
TGAATATTTATGACGATTCCGCAGTATTGGACGCTATCCAGTCTAAACATTTTACTATTACCCCCTCTGGCAAAACT
TCTTTTGCAAAAGCCTCTCGCTATTTTGGTTTTTATCGTCGTCTGGTAAACGAGGGTTATGATAGTGTTGCTCTTAC
TATGCCTCGTAATTCCTTTTGGCGTTATGTATCTGCATTAGTTGAATGTGGTATTCCTAAATCTCAACTGATGAATC
TTTCTACCTGTAATAATGTTGTTCCGTTAGTTCGTTTTATTAACGTAGATTTTTCTTCCCAACGTCCTGACTGGTAT
AATGAGCCAGTTCTTAAAATCGCATAAGGTAATTCACAATGATTAAAGTTGAAATTAAACCATCTCAAGCCCAATTT
ACTACTCGTTCTGGTGTTTCTCGTCAGGGCAAGCCTTATTCACTGAATGAGCAGCTTTGTTACGTTGATTTGGGTAA
TGAATATCCGGTTCTTGTCAAGATTACTCTTGATGAAGGTCAGCCAGCCTATGCGCCTGGTCTGTACACCGTTCATC
TGTCCTCTTTCAAAGTTGGTCAGTTCGGTTCCCTTATGATTGACCGTCTGCGCCTCGTTCCGGCTAAGTAACATGGA
GCAGGTCGCGGATTTCGACACAATTTATCAGGCGATGATACAAATCTCCGTTGTACTTTGTTTCGCGCTTGGTATAA
TCGCTGGGGGTCAAAGATGAGTGTTTTAGTGTATTCTTTTGCCTCTTTCGTTTTAGGTTGGTGCCTTCGTAGTGGCA
TTACGTATTTTACCCGTTTAATGGAAACTTCCTCATGAAAAAGTCTTTAGTCCTCAAAGCCTCTGTAGCCGTTGCTA
CCCTCGTTCCGATGCTGTCTTTCGCTGCTGAGGGTGACGATCCCGCAAAAGCGGCCTTTAACTCCCTGCAAGCCTCA
GCGACCGAATATATCGGTTATGCGTGGGCGATGGTTGTTGTCATTGTCGGCGCAACTATCGGTATCAAGCTGTTTAA
GAAATTCACCTCGAAAGCAAGCTGATAAACCGATACAATTAAAGGCTCCTTTTGGAGCCTTTTTTTTGGAGATTTTC
AACGTGAAAAAATTATTATTCGCAATTCCTTTAGTTGTTCCTTTCTATTCTCACTCCGCTGAAACTGTTGAAAGTTG
TTTAGCAAAATCCCATACAGAAAATTCATTTACTAACGTCTGGAAAGACGACAAAACTTTAGATCGTTACGCTAACT
ATGAGGGCTGTCTGTGGAATGCTACAGGCGTTGTAGTTTGTACTGGTGACGAAACTCAGTGTTACGGTACATGGGTT
CCTATTGGGCTTGCTATCCCTGAAAATGAGGGTGGTGGCTCTGAGGGTGGCGGTTCTGAGGGTGGCGGTTCTGAGGG
TGGCGGTACTAAACCTCCTGAGTACGGTGATACACCTATTCCGGGCTATACTTATATCAACCCTCTCGACGGCACTT
ATCCGCCTGGTACTGAGCAAAACCCCGCTAATCCTAATCCTTCTCTTGAGGAGTCTCAGCCTCTTAATACTTTCATG
TTTCAGAATAATAGGTTCCGAAATAGGCAGGGGGCATTAACTGTTTATACGGGCACTGTTACTCAAGGCACTGACCC
CGTTAAAACTTATTACCAGTACACTCCTGTATCATCAAAAGCCATGTATGACGCTTACTGGAACGGTAAATTCAGAG
ACTGCGCTTTCCATTCTGGCTTTAATGAGGATTTATTTGTTTGTGAATATCAAGGCCAATCGTCTGACCTGCCTCAA
CCTCCTGTCAATGCTGGCGGCGGCTCTGGTGGTGGTTCTGGTGGCGGCTCTGAGGGTGGTGGCTCTGAGGGTGGCGG
TTCTGAGGGTGGCGGCTCTGAGGGAGGCGGTTCCGGTGGTGGCTCTGGTTCCGGTGATTTTGATTATGAAAAGATGG
CAAACGCTAATAAGGGGGCTATGACCGAAAATGCCGATGAAAACGCGCTACAGTCTGACGCTAAAGGCAAACTTGAT
TCTGTCGCTACTGATTACGGTGCTGCTATCGATGGTTTCATTGGTGACGTTTCCGGCCTTGCTAATGGTAATGGTGC
TACTGGTGATTTTGCTGGCTCTAATTCCCAAATGGCTCAAGTCGGTGACGGTGATAATTCACCTTTAATGAATAATT
TCCGTCAATATTTACCTTCCCTCCCTCAATCGGTTGAATGTCGCCCTTTTGTCTTTGGCGCTGGTAAACCATATGAA
TTTTCTATTGATTGTGACAAAATAAACTTATTCCGTGGTGTCTTTGCGTTTCTTTTATATGTTGCCACCTTTATGTA
TGTATTTTCTACGTTTGCTAACATACTGCGTAATAAGGAGTCTTAATCATGCCAGTTCTTTTGGGTATTCCGTTATT
ATTGCGTTTCCTCGGTTTCCTTCTGGTAACTTTGTTCGGCTATCTGCTTACTTTTCTTAAAAAGGGCTTCGGTAAGA
TAGCTATTGCTATTTCATTGTTTCTTGCTCTTATTATTGGGCTTAACTCAATTCTTGTGGGTTATCTCTCTGATATT
AGCGCTCAATTACCCTCTGACTTTGTTCAGGGTGTTCAGTTAATTCTCCCGTCTAATGCGCTTCCCTGTTTTTATGT
TATTCTCTCTGTAAAGGCTGCTATTTTCATTTTTGACGTTAAACAAAAAATCGTTTCTTATTTGGATTGGGATAAAT
AATATGGCTGTTTATTTTGTAACTGGCAAATTAGGCTCTGGAAAGACGCTCGTTAGCGTTGGTAAGATTCAGGATAA
```

```
AATTGTAGCTGGGTGCAAAATAGCAACTAATCTTGATTTAAGGCTTCAAAACCTCCCGCAAGTCGGGAGGTTCGCTA
AAACGCCTCGCGTTCTTAGAATACCGGATAAGCCTTCTATATCTGATTTGCTTGCTATTGGGCGCGGTAATGATTCC
TACGATGAAAATAAAAACGGCTTGCTTGTTCTCGATGAGTGCGGTACTTGGTTTAATACCCGTTCTTGGAATGATAA
GGAAAGACAGCCGATTATTGATTGGTTTCTACATGCTCGTAAATTAGGATGGGATATTATTTTTCTTGTTCAGGACT
TATCTATTGTTGATAAACAGGCGCGTTCTGCATTAGCTGAACATGTTGTTTATTGTCGTCGTCTGGACAGAATTACT
TTACCTTTTGTCGGTACTTTATATTCTCTTATTACTGGCTCGAAAATGCCTCTGCCTAAATTACATGTTGGCGTTGT
TAAATATGGCGATTCTCAATTAAGCCCTACTGTTGAGCGTTGGCTTTATACTGGTAAGAATTTGTATAACGCATATG
ATACTAAACAGGCTTTTTCTAGTAATTATGATTCCGGTGTTTATTCTTATTTAACGCCTTATTTATCACACGGTCGG
TATTTCAAACCATTAAATTTAGGTCAGAAGATGAAATTAACTAAAATATATTTGAAAAAGTTTTCTCGCGTTCTTTG
TCTTGCGATTGGATTTGCATCAGCATTTACATATAGTTATATAACCCAACCTAAGCCGGAGGTTAAAAAGGTAGTCT
CTCAGACCTATGATTTTGATAAATTCACTATTGACTCTTCTCAGCGTCTTAATCTAAGCTATCGCTATGTTTTCAAG
GATTCTAAGGGAAAATTAATTAATAGCGACGATTTACAGAAGCAAGGTTATTCACTCACATATATTGATTTATGTAC
TGTTTCCATTAAAAAAGGTAATTCAAATGAAATTGTTAAATGTAATTAATTTTGTTTTCTTGATGTTTGTTTCATCA
TCTTCTTTTGCTCAGGTAATTGAAATGAATAATTCGCCTCTGCGCGATTTTGTAACTTGGTATTCAAAGCAATCAGG
CGAATCCGTTATTGTTTCTCCCGATGTAAAAGGTACTGTTACTGTATATTCATCTGACGTTAAACCTGAAAATCTAC
GCAATTTCTTTATTTCTGTTTTACGTGCAAATAATTTTGATATGGTAGGTTCTAACCCTTCCATTATTCAGAAGTAT
AATCCAAACAATCAGGATTATATTGATGAATTGCCATCATCTGATAATCAGGAATATGATGATAATTCCGCTCCTTC
TGGTGGTTTCTTTGTTCCGCAAAATGATAATGTTACTCAAACTTTTAAAATTAATAACGTTCGGGCAAAGGATTTAA
TACGAGTTGTCGAATTGTTTGTAAAGTCTAATACTTCTAAATCCTCAAATGTATTATCTATTGACGGCTCTAATCTA
TTAGTTGTTAGTGCTCCTAAAGATATTTTAGATAACCTTCCTCAATTCCTTTCAACTGTTGATTTGCCAACTGACCA
GATATTGATTGAGGGTTTGATATTTGAGGTTCAGCAAGGTGATGCTTTAGATTTTTCATTTGCTGCTGGCTCTCAGC
GTGGCACTGTTGCAGGCGGTGTTAATACTGACCGCCTCACCTCTGTTTTATCTTCTGCTGGTGGTTCGTTCGGTATT
TTTAATGGCGATGTTTTAGGGCTATCAGTTCGCGCATTAAAGACTAATAGCCATTCAAAAATATTGTCTGTGCCACG
TATTCTTACGCTTTCAGGTCAGAAGGGTTCTATCTCTGTTGGCCAGAATGTCCCTTTTATTACTGGTCGTGTGACTG
GTGAATCTGCCAATGTAAATAATCCATTTCAGACGATTGAGCGTCAAAATGTAGGTATTTCCATGAGCGTTTTTCCT
GTTGCAATGGCTGGCGGTAATATTGTTCTGGATATTACCAGCAAGGCCGATAGTTTGAGTTCTTCTACTCAGGCAAG
TGATGTTATTACTAATCAAAGAAGTATTGCTACAACGGTTAATTTGCGTGATGGACAGACTCTTTTACTCGGTGGCC
TCACTGATTATAAAAACACTTCTCAGGATTCTGGCGTACCGTTCCTGTCTAAAATCCCTTTAATCGGCCTCCTGTTT
AGCTCCCGCTCTGATTCTAACGAGGAAAGCACGTTATACGTGCTCGTCAAAGCAACCATAGTACGCGCCCTGTAGCG
GCGCATTAAGCGCGGCGGGTGTGGTGGTTACGCGCAGCGTGACCGCTACACTTGCCAGCGCCCTAGCGCCCGCTCCT
TTCGCTTTCTTCCCTTCCTTTCTCGCCACGTTCGCCGGCTTTCCCCGTCAAGCTCTAAATCGGGGGCTCCCTTTAGG
GTTCCGATTTAGTGCTTTACGGCACCTCGACCCCAAAAAACTTGATTTGGGTGATGGTTCACGTAGTGGGCCATCGC
CCTGATAGACGGTTTTTCGCCCTTTGACGTTGGAGTCCACGTTCTTTAATAGTGGACTCTTGTTCCAAACTGGAACA
ACACTCAACCCTATCTCGGGCTATTCTTTTGATTTATAAGGGATTTTGCCGATTTCGGAACCACCATCAAACAGGAT
TTTCGCCTGCTGGGGCAAACCAGCGTGGACCGCTTGCTGCAACTCTCTCAGGGCCAGGCGGTGAAGGGCAATCAGCT
GTTGCCCGTCTCACTGGTGAAAAGAAAAACCACCCTGGCGCCCAATACGCAAACCGCCTCTCCCCGCGCGTTGGCCG
ATTCATTAATGCAGCTGGCACGACAGGTTTCCCGACTGGAAAGCGGGCAGTGAGCGCAACGCAATTAATGTGAGTTA
GCTCACTCATTAGGCACCCCAGGCTTTACACTTTATGCTTCCGGCTCGTATGTTGTGTGGAATTGTGAGCGGATAAC
AATTTCACACAGGAAACAGCTATGACCATGATTACGAATTCGAGCTCGGTACCCGGGGATCC
```

### A.3.2 Core staple strands

It should be noted that the number of core staple strands here is slightly less than the number of core staple strands in the paper [D] Gür *et al.,* Toward Self-Assembled Plasmonic Devices: High-Yield Arrangement of Gold Nanoparticles on DNA Origami Templates. ACS Nano 2016, 10, 5374–5382. The difference is binding sites from 0 to 9 were introduced in this thesis, while in the paper binding sites from 1 to 8 were used.

| | |
|---|---|
| Oligonucleotide 1 | TTAAATCAGCTCATGTGGCATCAATTCTATCAGTTGAGATTT |
| Oligonucleotide 2 | CCCGATTTAGAGCTCCGAGATAGGGTTGAACGGTAATCGTAA |
| Oligonucleotide 3 | ACAAACGGCGGATTTCATTCCATATAACTAGCGAGAGGCTTT |

| | |
|---|---|
| Oligonucleotide 4 | GCAAAGACACCACGCTAAATTTAATGGTGGGTTATATAACTA |
| Oligonucleotide 5 | AACAACATGTTCAGCAGAGGGTAATTGAATCACCGGAACCAG |
| Oligonucleotide 6 | CGGGAGCTAAACAGGCCAACGCGCGGGGAGCTTTCATCAACA |
| Oligonucleotide 7 | AGGTTTTGAAGCCTGAACGCGAGGCGTTTTCCTGATTATCAG |
| Oligonucleotide 8 | GACCAGTCAGGAAAAACGCTC |
| Oligonucleotide 9 | GCAGCAAGCGGTCCGTCACGCTGCGCGTATCTAAAATATCTT |
| Oligonucleotide 10 | TGGCAGATTCACCAAGCGGATTGCATCAATATCGCGTTTTAA |
| Oligonucleotide 11 | AGGCCACCGAGTAATGAGCTAACTCACAAGGTCACGTTGGTG |
| Oligonucleotide 12 | GCAACAGCTGATTGCCGCTACAGGGCGCGTCAGTTGGCAAAT |
| Oligonucleotide 13 | GCTGACCTTCATCATCAATATAATCCTGGATATAGAAGGCTT |
| Oligonucleotide 14 | TCTGGCCAACAGAGCAAAAATCAGGTCTAGCAAACTCCAACA |
| Oligonucleotide 15 | TTTGCTCAGTACCAGGGAGCCACCACCCTCACAGAGAGAATAAC |
| Oligonucleotide 16 | GTACGGTGTCTGGAAGTTGACCGTAATGGGATTTAATTGCGTTGCG |
| Oligonucleotide 17 | TGCCTTGAGTAACAGTGAATGGAAAGCGCACAACGCTAACGAGC |
| Oligonucleotide 18 | GCAGACGGTCAATCACAGAAATAAAGAACAAGTACCGCACTC |
| Oligonucleotide 19 | GAGATAACCCACAAAAGTAATTCTGTCCAAACATCAAGAAAA |
| Oligonucleotide 20 | GCATTAATGAATCGGAGGCCGATTAAAGGCCACGCTGAGAGC |
| Oligonucleotide 21 | GAAACCGAGGAAACTATAAAGCCAACGCTTAATTTTCCCTTA |
| Oligonucleotide 22 | TCACCCTCAGCAGCATCGTCGCTATTAATCAACAGTAGGGCT |
| Oligonucleotide 23 | GATATAAGTATAGCCCGGCCGCCTCCCTCAGAAGAATTAACTGAAC |
| Oligonucleotide 24 | AACAACATTATTACAATTGAGGAAGGTTAACCACCACACCCG |
| Oligonucleotide 25 | CGACAACTCGTATTTTAATTTCAACTTTTACTTTTGCGGGAG |
| Oligonucleotide 26 | CAATAGATAATACATTTGAGGATTAAGAACTGGCTCATAAAGCTAAA |
| Oligonucleotide 27 | TTGGAACAAGAGTCGCACTAAATCGGAAAACGTTATTAATTT |
| Oligonucleotide 28 | CCTTGCTTCTGTAAGAAAGACAGCATCGTTTCGTCACCAGTA |
| Oligonucleotide 29 | CATTGAATCCCCCTGACAATATTTTTGATAACATCACTTGCC |
| Oligonucleotide 30 | TCGGTTGTACCAAAAACATCATATGTACCCCGAAAATCCCTTATAA |
| Oligonucleotide 31 | ATGATGGCAATTCAAGAGTAATCTTGACAGTCAAATCACCAT |
| Oligonucleotide 32 | ATCGAGAACAAGCATAATTTGCCAGTTAACAAACAAATAAAT |
| Oligonucleotide 33 | ATGGAAATACCTACCTGCAAGGCGATTAGGGAAGGGCGATCG |
| Oligonucleotide 34 | CTCATATATTTTAAATCTACAAAGGCTATCGTGGACTCCAACGT |
| Oligonucleotide 35 | GCTGAACCTCAAATATCAAACCCCAACTAATGCAGATATTTTCATTT |
| Oligonucleotide 36 | CCAATCGTATATTTTAGTTAA |
| Oligonucleotide 37 | AAGTTTCCATTAAATTTAACAATTTCATAGAGAATATAAAGT |
| Oligonucleotide 38 | TGAGTAGAAGAACTCTGTGTGAAATTGTCGCACTCCAGCCAG |
| Oligonucleotide 39 | GTTTACCAGACGACCCGCCTGCAACAGTGGATTTTAGACAGG |
| Oligonucleotide 40 | GGCCGGAAACGTCATGTAGCATTCCACACTTTTGCGGGATCG |
| Oligonucleotide 41 | ACCGACAAAAGGTAGAATTGAGTTAAGCCATAGCCCCCTTAT |

| | |
|---|---|
| Oligonucleotide 42 | AAGCCTTTATTTCACAAGAGAATCGATGAGTGTTGTTCCAGT |
| Oligonucleotide 43 | AATAGATAAGTCCTGCGCATTAGACGGGGCCGCCACCCTCAG |
| Oligonucleotide 44 | ACAGTTTCAGCGGAGGTAAATATTGACGCATATAAAAGAAAC |
| Oligonucleotide 45 | TATCAAAATTATTTGCACGTAAAATAAGGGAACCGAATTAATGCCCC |
| Oligonucleotide 46 | ATAATTACTAGAAACTCCTTATTACGCAAGCCATTTGGGAAT |
| Oligonucleotide 47 | AGACGCTGAGAAGAGTCAATAGTCGCCCACGCATAACCTTTCCAGAC |
| Oligonucleotide 48 | CAAGCAGCTGTTTCCAAACTATCGGCCTACCTGAAAGCGTAA |
| Oligonucleotide 49 | GGGCTTGAGATGGTAAATCCTTTGCCCGCCCTAAAGGGAGCC |
| Oligonucleotide 50 | AGTTAGCGTAACGATCTCACCAGTAGCACCATACCCAAAAGAAC |
| Oligonucleotide 51 | CGTTCCAGTAAGCGCTGGTAATAAGTTTAGGCGCATAGGCTG |
| Oligonucleotide 52 | CAAACTACAACGCCCCAATGAAACCATCAAAGTTACCAGAAG |
| Oligonucleotide 53 | GGGGCGCGAGCTGAAAAGTTTTTAACCAATAGCACCAGTGAGACGG |
| Oligonucleotide 54 | GGCTGAGACTCCTCCCGCCGCCAGCATTACGATTTTTTGTTT |
| Oligonucleotide 55 | GTGTGATAAATAAGCATAAAGGTGGCAAGAAATTATTCATTA |
| Oligonucleotide 56 | AGAACAATATTACCCACGACGTTGTAAAACCAGGCAAAGCGC |
| Oligonucleotide 57 | ACCTTATGCGATTTTTAGAAGTATTAGAGGCGAACGTGGCGA |
| Oligonucleotide 58 | GTTAGTAAATGAATTTTCCCGTCACCGACTTGGTATGTTAGCAAAC |
| Oligonucleotide 59 | AGGAATACCACATTTCAATCAATATCTGGTACTATGGTTGCT |
| Oligonucleotide 60 | TTTCATCTTCTGACGAATAAGTTTATTTGCGACATTCAACCG |
| Oligonucleotide 61 | AAGGTGAATTATCATGTATGGGATTTTGTAGTTGCGCCGACA |
| Oligonucleotide 62 | ATTACCGCGCCCAAATCCTGAATCTTACGTCTCTGAATTTAC |
| Oligonucleotide 63 | CATTAACATCCAATTTTTGTTAAAATTCGCCCTGAGAGAGTT |
| Oligonucleotide 64 | GAATACGTGGCACACAAATGCTTTAAACCTCCTTTTGATAAG |
| Oligonucleotide 65 | CAAATTCTTACCAGGCAATAATAACGGAATTACCATTAGCAA |
| Oligonucleotide 66 | GCCCACTACGTGAACCGTCTATCAGGGCCCGGAGAGGGTAGC |
| Oligonucleotide 67 | AGGCAGAGGCATTTTAGCAATAGCTATCTTTAGCGTCAGACT |
| Oligonucleotide 68 | ACGGCTACAGAGGCACATAAATCAATATCCAACATGTAATTT |
| Oligonucleotide 69 | AGGGTTTTCCCAGTGCCAGCCATTGCAAAATAAAAGGGACAT |
| Oligonucleotide 70 | ACCCTGAACAAAGTCTAATGCAGAACGCATTATTCATTTCAA |
| Oligonucleotide 71 | ATTGCGAATAATAACCAAAGACAAAAGGTGTCACAATCAATA |
| Oligonucleotide 72 | CAGGTTTAACGTCAGCTCCATGTTACTTTGAAAGTATTAAGA |
| Oligonucleotide 73 | GCTTTGAATACCAAGTTACAAAACCCCAGCGATTATACGAGAGGGTT |
| Oligonucleotide 74 | TCGCAAATGGTCAATAGCCTTCCTGTAGCCAGAGGCGGTTTGCG |
| Oligonucleotide 75 | GTTGTAGCAATACTGAGCCGGAAGCATAGCCAGTTTGAGGGG |
| Oligonucleotide 76 | TTACCTGAGCAAAAACGAAAGAGGCAAACGTACTCAGGAGGT |
| Oligonucleotide 77 | ATAATGCTGTAGCTCAGTAACCGTGCATCTAAGTGTAAAGCCTG |
| Oligonucleotide 78 | AAGGCTTGCCCTGAACATTATCATTTTGAAGTTTTTTGGGGT |
| Oligonucleotide 79 | AATCAGTAGCGACAACCGTAACACTGAGGAACGAGGGTAGCA |

| | |
|---|---|
| Oligonucleotide 80 | AAGTACAACGGAGAATAACGGATTCGCCATATCCCATCCTAA |
| Oligonucleotide 81 | TCCACACAACATACTCTTTGATTAGTAAATGGCTATTAGTCT |
| Oligonucleotide 82 | CCGCGCTTAATGCGCCCTTCACCGCCTGGCATTAAATTTTTG |
| Oligonucleotide 83 | GTGAATTTCTTAAACTCCGGCTTAGGTTTTGAAATACCGACC |
| Oligonucleotide 84 | ATATTATTTATCCCAACGGGTATTAAACATTGCGTAGATTTT |
| Oligonucleotide 85 | CACCCTCAGAGCCACCTCGGCATTTTCGGTCCAATAATAAGAGC |
| Oligonucleotide 86 | CTTATCATTCCAAGAATCCAAATAAGAAGACAGGAGGTTGAG |
| Oligonucleotide 87 | AGCCACCACCGGAAAATAGGTGTATCACAGAATACACTAAAA |
| Oligonucleotide 88 | TTCGAGCTTCAAAGGCTGCGCAACTGTTAGTTGGGTAACGCC |
| Oligonucleotide 89 | AGACTGGATAGCGTGATAGCCCTAAAACCACGCAAATTAACC |
| Oligonucleotide 90 | CTCACTGCCCGCTTATCCTGAGAAGTGTAACAGAGGTGAGGC |
| Oligonucleotide 91 | GGTCAGGATTAGAGTTCTGGTGCCGGAAACGACGGCCAGTGC |
| Oligonucleotide 92 | GAGTCTGGAGCAAAACGCAAGGATAAAAACGAGTAGTAAATT |
| Oligonucleotide 93 | AACGGTACGCCAGATCCAGTCGGGAAACGATTCTCCGTGGGA |
| Oligonucleotide 94 | ATCAAAAGAATAGCTGACGGGGAAAGCCCTTTACAAACAATT |
| Oligonucleotide 95 | TTAAATGTGAGCGAGATTTAGTTTGACCCTATCATAACCCTC |
| Oligonucleotide 96 | AGCAAAATTAAGCAATGGAAGATTGTATAACAGCAGGCGAAAAT |
| Oligonucleotide 97 | GATACAGGAGTGTATCATACATGGCTTTTTGCTATTTTGCAC |
| Oligonucleotide 98 | TTAGTACCGCCACCTTTTCATAATCAAAGCGCTAATATCAGA |
| Oligonucleotide 99 | CAACAGTTGAAAGGAGGTAGAAAGATTCACTAATAGTAGTAG |
| Oligonucleotide 100 | GCAGGTCAGACGATATTATTCTGAAACAAGCCGGAACGAGGC |
| Oligonucleotide 101 | CTTTCCGGCACCGCAGTACCTTTAATTGAGTTCAGAAAACGA |
| Oligonucleotide 102 | TTCAACCGTTCTAGGAAAGGCCGGAGACAAGAACCGGATATT |
| Oligonucleotide 103 | TTACCTTTTTTAATGGAAACAGTTTTGAGGACTAAAGGGATAGCAAG |
| Oligonucleotide 104 | TAATTGAGAATCGCGCAGATAGCCGAACGATAGCAGCACCGT |
| Oligonucleotide 105 | CACTCATCTTTGACTCGCGCAGAGGCGAGCCTGTTTATCAAC |
| Oligonucleotide 106 | TAGCGTTTGCCATCCTCAGAACCGCCACAATGCCACTACGAA |
| Oligonucleotide 107 | AACCACCACCAGAGAAGAGAAGGATTAGTGATAAATTGTGTC |
| Oligonucleotide 108 | AAGAGGACAGATGAGAAGGGTTAGAACCTCATCGTAGGAATC |
| Oligonucleotide 109 | AAAGATTCAAAAGGGTGACTGATAAATTAATGGACCGACTTGCGGG |
| Oligonucleotide 110 | ACGACGACAGTATCGATGGCTTAGAGCTTCGTCATAAATATT |
| Oligonucleotide 111 | ATCCGGTATTCTAATAAATCAAGATTAGTGATCAATATGATA |
| Oligonucleotide 112 | CATTACCCAAATCAGAATTATCATCATATTAGCGAACCTCTG |
| Oligonucleotide 113 | GGAATTACGAGGCAAAATCTAAAGCATCCGTTAGAATCAGAG |
| Oligonucleotide 114 | CGAGGTGCCGTAAACACTATTAAAGAACAGGTCATTGCCTGA |
| Oligonucleotide 115 | CCCAATAGGAACCCATGTGAATCAAGTTTGCCTTACCGAAGCCCTT |
| Oligonucleotide 116 | TTGACGAGCACGTAGTGGTTTTTCTTTTGAACGCCATCAAAA |
| Oligonucleotide 117 | GCTGAGGCTTGCAGATAGCGATAGCTTATCATATGCGTTATA |

| | |
|---|---|
| Oligonucleotide 118 | GGCACCAACCTAAAGAAGATGATGAAACAGACGACGACAATA |
| Oligonucleotide 119 | CTGCCTATTTCGGAACCTTGGCCTTGATATTCCAAAATAAACAGCC |
| Oligonucleotide 120 | CATTAAAAATACCGAACGAACCATGCCAGAGGGGGTATGCAACTAAA |
| Oligonucleotide 121 | AACGTCAAAAATGAGAAACCAATCAATAAACAGTACCTTTTA |
| Oligonucleotide 122 | TGGCAAGTGTAGCGACGCTGGTTTGCCCGCAAATATTTAAAT |
| Oligonucleotide 123 | GAAAGGAAGGGAAGGTTCCGAAATCGGCGTTGATAATCAGAA |
| Oligonucleotide 124 | AGGTCATTTTTGCGGGCCTCAGGAAGATTATCCGCTCACAAT |
| Oligonucleotide 125 | CCAGCTACAATTTTTAGCAAGCAAATCAATTGTTTGGATTAT |
| Oligonucleotide 126 | ACGTTGGGAAGAAAACTAATAGATTAGAGGGCGCTAGGGCGC |
| Oligonucleotide 127 | TGTAAACGTTAATAAAATCATACAGGCAAAACGAACTAACGG |
| Oligonucleotide 128 | CAAAGAAACCACCAGAAGGAGCGACGTAACAAAGCTGATGTGTAGGT |
| Oligonucleotide 129 | GAATGACCATAAATATAGAACCCTTCTGTGCTGGTAATATCC |
| Oligonucleotide 130 | GTAGAAAATACATAGCGTTAAATAAGAACATAGGTCTGAGAG |
| Oligonucleotide 131 | ACTACCTTTTTAACCAGCTTGATACCGACTAAACAACTTTCA |
| Oligonucleotide 132 | GAAATCCGCGACCTGATGAATATACAGTATCGGCTGTCTTTC |
| Oligonucleotide 133 | GGTCAGTATTAACAGATAAAAACCAAAAAGTTGATTCCCAAT |
| Oligonucleotide 134 | ATGACAACAACCATGAATTTATCAAAATTAAACACCGGAATC |
| Oligonucleotide 135 | AACTAGCATGTCAATTATGACCCTGTAAAATCATTGTGAATT |
| Oligonucleotide 136 | TCTGCGAACGAGTAGTAACAACCCGTCGCTGTCGTGCCAGCT |
| Oligonucleotide 137 | TGCAAAAGAAGTTTCCAGCAGAAGATAATTTTATAATCAGTG |
| Oligonucleotide 138 | TTTACGAGCATGTAAAATAGCAGCCTTTAGAGCCGCCACCAG |
| Oligonucleotide 139 | ATTGAGGGAGGGAAGTGAGAATAGAAAGAGCTTGCTTTCGAG |
| Oligonucleotide 140 | TTTAAGAAAAGTAACATATTTAACAACGATGTGAGTGAATAA |

## A.3.3 Binding site staple strands

It should be noted that binding sites from 0 to 9 should be included to the assembly reaction with/out extension (colored extension) depending on the desired binding sites for the attachment of AuNPs or/and Qdots. For example, for the alternating binding sites for the attachment of AuNPs, binding sites 0, 2, 4, and 8 are picked, and staple strands lacking poly-A extensions for binding sites 1, 3, 5, 7 and 9 are used.

### A.3.3.1 Binding sites for the attachment of AuNPs

| | |
|---|---|
| BS 0 | ATAGTCAGAAGCAAGTCACACAAAAAAAAAAAAAAA |
| BS 0 | GACCGGATTACCCTGACTATTAAAAAAAAAAAAAAA |

| | |
|---|---|
| BS 0 | CATTCGCCATTCAGCGAACCAAAAAAAAAAAAAAAA |
| | |
| BS 1 | TAGATGGGCGCATCACATGTTTTAAATAATAGTAAAATGTTTAAAAAAAAAAAAAAA |
| BS 1 | GGGTGCCTAATGAGAAGAGTCTGTCCATATCGCAAAAAAAAAAAAAAA |
| BS 1 | TTAATGCGCGAACTCCAATACTGCGGAATAATTGCTGAATAAAAAAAAAAAAAAA |
| | |
| BS 2 | ATAATTCGCGTCTGACCTGTTTAGCTATACATAACGCCAAAAAAAAAAAAAAAAAAA |
| BS 2 | TATTGGGCGCCAGGTAACGTGCTTTCCTACCTTAAAAAAAAAAAAAAA |
| BS 2 | CAGCAGCAAATGAATAGTAAGAGCAACAATTAGATACATTAAAAAAAAAAAAAAA |
| | |
| BS 3 | AAGCCCCAAAAACAAAAGCCTCAGAGCATTATACCAGTCAGGAAAAAAAAAAAAAAA |
| BS 3 | CCTGTTTGATGGTGAAAGCGAAAGGAGCGCCGTAAAAAAAAAAAAAAA |
| BS 3 | TAGGAGCACTAACAAATCTACGTTAATAAGGCAAAGAATTAAAAAAAAAAAAAAA |
| | |
| BS 4 | TATTTTTGAGAGATGCAATGCCTGAGTACTCATTCAGTGAATAAAAAAAAAAAAAAA |
| BS 4 | CAAAGGGCGAAAAACCATCACCCAAATCCGGAAAAAAAAAAAAAAAAA |
| BS 4 | TAAAAGTTTGAGTACGAGAAACACCAGAATTTTTAGAACCAAAAAAAAAAAAAAA |
| | |
| BS 5 | CCTCATTAAAGCCAGCCCGTATAAACAGCTGACCAACTTTGAAAAAAAAAAAAAAAA |
| BS 5 | GTCTTTCCAGAGCCAGCCGTTTTTATTTTACCAAAAAAAAAAAAAAAA |
| BS 5 | ACTTCTGAATAATGACGGTGTACAGACCTAACGGGGTCAGAAAAAAAAAAAAAAA |
| | |
| BS 6 | AACCGCCACCCTCACGGATAAGTGCCGTCCAAGCGCGAAACAAAAAAAAAAAAAAAA |
| BS 6 | ATAAAAACAGGGAAGAACAAGAAAAATATGATTAAAAAAAAAAAAAAA |
| BS 6 | CATCGGGAGAAACATTTGTATCATCGCCGATTAGCGGGGTAAAAAAAAAAAAAAA |
| | |
| BS 7 | GTAGCGCGTTTTCAACCCTCATTTTCAGACTTTTTCATGAGGAAAAAAAAAAAAAAA |
| BS 7 | AAGAAACAATGAAATCGAGCCAGTAATATTGAAAAAAAAAAAAAAAAA |
| BS 7 | CAAAATTAATTACACGGGTAAAATACGTCCTCAGAACCGCAAAAAAAAAAAAAAA |
| | |
| BS 8 | TAGAGCCAGCAAAATAAAGTTTTGTCGTCGATATATTCGGTCAAAAAAAAAAAAAAA |
| BS 8 | TGGCATGATTAAGAAAGCCTGTTTAGTAGATTAAAAAAAAAAAAAAAA |
| BS 8 | GAATCCTTGAAAACGGAGTTAAAGGCCGGACAGCCCTCATAAAAAAAAAAAAAAA |
| | |
| BS 9 | TATGTAAATGCTGATGTATCGAAAAAAAAAAAAAAA |
| BS 9 | GTTTATCGAACAACTAAAGGAAAAAAAAAAAAAAAA |
| BS 9 | AAGGAGCCTTTAATTGCAAATAAAAAAAAAAAAAAA |

### A.3.3.2 Thiol modified oligonucleotides for the functionalization of AuNPs

| | |
|---|---|
| Monothiol | 5'-ThioMC6-D/TTTTTTTTTTTTTTTTTTT |
| Dithiol | 5'-DTPA/TTTTTTTTTTTTTTTTTTT |

### A.3.3.3 Binding sites for the attachment of Qdots

| | |
|---|---|
| BS 0 | ATAGTCAGAAGCAAGTCACACGAAGAAGAAGAAGAAGAA |
| BS 0 | GACCGGATTACCCTGACTATTGAAGAAGAAGAAGAAGAA |
| BS 0 | CATTCGCCATTCAGCGAACCAGAAGAAGAAGAAGAAGAA |
| | |
| BS 9 | TATGTAAATGCTGATGTATCGGTGTGTGTGTGTGTGTGT |
| BS 9 | GTTTATCGAACAACTAAAGGAGTGTGTGTGTGTGTGTGT |
| BS 9 | AAGGAGCCTTTAATTGCAAATGTGTGTGTGTGTGTGTGT |

### A.3.3.4 Biotin modified oligonucleotides for the functionalization of Qdots

| | |
|---|---|
| For donor Qdot-BS 0 | 5'-BIO TTCTTCTTCTTCTTCTTC |
| For acceptor Qdot-BS 9 | 5'-BIO ACACACACACACACACAC |

## A.3.4 Staple strands for multimerization of 6-HBs

It should be noted that these are additional staple strands in the ss loops of the 6-HB for interconnecting monomer A, B, C 6-HBs. These staple strands were added only for the multimerization experiments.

| | |
|---|---|
| A Left 1 | GTGCGGGCCTCTTCGCTATTACG |
| A Left 2 | CCAGCTGGCGAAAGGGGGATGTGATTTTGACGCTCAATCGTC |
| A Left 3 | TGAAATGGATTATTTACAT |
| | |
| A Right 1 | GAAAATTACCAGCGTTTTTTCACGTTGAAAAAAAGGCTCCAA |
| A Right 2 | ACTTTTTCAAACAAGACAAAGA |
| | |
| B Left 1 | AAAAGATTAAGAGGAATCCAA |
| B Left 2 | AAATCGCCCGAAAGACTTCAA |
| B Left 3 | GTGCGGGCCTCTTCGCTATTACGGGTTT |
| B Left 4 | CATATCCAGCTGGCGAAAGGGGGATGTG |

| | |
|---|---|
| B Left 5 | ATTTTGACGCTCAATCGTCAGAAA |
| B Left 6 | ACGCGTGAAATGGATTATTTACAT |
| | |
| B Right 1 | AGGAATCCAAAAAAAAGGCTCCAA |
| B Right 2 | TTTTTTCACGTTGAAAATCGCCCG |
| B Right 3 | TTACGGGTTTACCAGCG |
| B Right 4 | GAAAATTCATATCCAGC |
| B Right 5 | TCGTCAGAAAACTTTTTCAAA |
| B Right 6 | CAAGACAAAGAACGCGTGAAA |
| | |
| C Left 1 | AAAGACTTCAAAAAAGATTTTACAT |
| C Left 2 | GTGCGGGCCTCTTCGCTA |
| C Left 3 | TGGCGAAAGGGGGATGTGATTTTGACGCTCAATGGATTATAAG |
| | |
| C Right 1 | TCCAAAAAAAAGGCTCCAA |
| C Right 2 | GGTTTACCAGCGTTTTTTCACGTTGAAAATC |
| C Right 3 | GAAAATTCATAT |
| C Right 4 | AGAAAACTTTTTCAAACAAGACAAAGAACGCG |

# REFERENCES

[1] S. A. Maier, *Plasmonics: fundamentals and applications*. New York: Springer, 2007.

[2] J. A. Schuller, E. S. Barnard, W. Cai, Y. C. Jun, J. S. White, and M. L. Brongersma, “Plasmonics for extreme light concentration and manipulation,” *Nat. Mater.*, vol. 9, no. 3, pp. 193–204, Mar. 2010.

[3] N. J. Halas, S. Lal, W.-S. Chang, S. Link, and P. Nordlander, “Plasmons in Strongly Coupled Metallic Nanostructures,” *Chem. Rev.*, vol. 111, no. 6, pp. 3913–3961, Jun. 2011.

[4] H. Xu, J. Aizpurua, M. Käll, and P. Apell, “Electromagnetic contributions to single-molecule sensitivity in surface-enhanced Raman scattering,” *Phys. Rev. E*, vol. 62, no. 3, p. 4318, 2000.

[5] F. Tam, G. P. Goodrich, B. R. Johnson, and N. J. Halas, “Plasmonic Enhancement of Molecular Fluorescence,” *Nano Lett.*, vol. 7, no. 2, pp. 496–501, Feb. 2007.

[6] T. Kalkbrenner, U. Håkanson, A. Schädle, S. Burger, C. Henkel, and V. Sandoghdar, “Optical Microscopy via Spectral Modifications of a Nanoantenna,” *Phys. Rev. Lett.*, vol. 95, no. 20, Nov. 2005.

[7] R. Hillenbrand, F. Keilmann, P. Hanarp, D. S. Sutherland, and J. Aizpurua, “Coherent imaging of nanoscale plasmon patterns with a carbon nanotube optical probe,” *Appl. Phys. Lett.*, vol. 83, no. 2, pp. 368–370, Jul. 2003.

[8] M. L. Brongersma, J. W. Hartman, and H. A. Atwater, “Electromagnetic energy transfer and switching in nanoparticle chain arrays below the diffraction limit,” *Phys. Rev. B*, vol. 62, no. 24, p. R16356, Dec. 2000.

[9] S. A. Maier, M. L. Brongersma, P. G. Kik, S. Meltzer, A. a. G. Requicha, and H. A. Atwater, “Plasmonics—A Route to Nanoscale Optical Devices,” *Adv. Mater.*, vol. 13, no. 19, pp. 1501–1505, Oct. 2001.

[10] L. A. Sweatlock, S. A. Maier, H. A. Atwater, J. J. Penninkhof, and A. Polman, “Highly confined electromagnetic fields in arrays of strongly coupled Ag nanoparticles,” *Phys. Rev. B*, vol. 71, no. 23, p. 235408, Jun. 2005.

[11] J. B. Pendry, “Negative Refraction Makes a Perfect Lens,” *Phys. Rev. Lett.*, vol. 85, no. 18, pp. 3966–3969, Oct. 2000.

[12] V. M. Shalaev, “Optical negative-index metamaterials,” *Nat. Photonics*, vol. 1, no. 1, p. 41, Jan. 2007.

[13] A. Yildiz, J. N. Forkey, S. A. McKinney, T. Ha, Y. E. Goldman, and P. R. Selvin, “Myosin V Walks Hand-Over-Hand: Single Fluorophore Imaging with 1.5-nm Localization,” *Science*, vol. 300, no. 5628, pp. 2061–2065, Jun. 2003.

[14] A. G. Skirtach *et al.*, “The Role of Metal Nanoparticles in Remote Release of Encapsulated Materials,” *Nano Lett.*, vol. 5, no. 7, pp. 1371–1377, Jul. 2005.

[15] L. R. Hirsch *et al.*, “Nanoshell-mediated near-infrared thermal therapy of tumors under magnetic resonance guidance,” *Proc. Natl. Acad. Sci.*, vol. 100, no. 23, pp. 13549–13554, Nov. 2003.

[16] D. P. N. Gonçalves *et al.*, “Enhanced targeting of invasive glioblastoma cells by peptide-functionalized gold nanorods in hydrogel-based 3D cultures,” *Acta Biomater.*, vol. 58, pp. 12–25, Aug. 2017.

[17] P. Drude, “Zur Elektronentheorie der Metalle,” *Ann. Phys.*, vol. 306, no. 3, pp. 566–613, Jan. 1900.

[18] X. Lu, M. Rycenga, S. E. Skrabalak, B. Wiley, and Y. Xia, “Chemical Synthesis of Novel Plasmonic Nanoparticles,” *Annu. Rev. Phys. Chem.*, vol. 60, no. 1, pp. 167–192, 2009.

[19] K. A. Willets and R. P. Van Duyne, “Localized Surface Plasmon Resonance Spectroscopy and Sensing,” *Annu. Rev. Phys. Chem.*, vol. 58, no. 1, pp. 267–297, Apr. 2007.

[20] W. Knoll, “Interfaces and thin films as seen by bound electromagnetic waves,” *Annu. Rev. Phys. Chem.*, vol. 49, no. 1, pp. 569–638, Oct. 1998.

[21] M. Piliarik, H. Vaisocherová, and J. Homola, “Surface Plasmon Resonance Biosensing,” in *Biosensors and Biodetection*, Humana Press, 2009, pp. 65–88.

[22] J. Homola, S. S. Yee, and G. Gauglitz, “Surface plasmon resonance sensors: review,” *Sens. Actuators B Chem.*, vol. 54, no. 1, pp. 3–15, Jan. 1999.

[23] “The British Museum.” [Online]. Available: http://www.britishmuseum.org/. [Accessed: 12-Dec-2017].

[24] S. A. Maier and H. A. Atwater, “Plasmonics: Localization and guiding of electromagnetic energy in metal/dielectric structures,” *J. Appl. Phys.*, vol. 98, no. 1, p. 011101, Jul. 2005.

[25] W. A. Murray and W. L. Barnes, “Plasmonic Materials,” *Adv. Mater.*, vol. 19, no. 22, pp. 3771–3782, Nov. 2007.

[26] G. Mie, “Beiträge zur Optik trüber Medien, speziell kolloidaler Metallösungen,” *Ann. Phys.*, vol. 330, no. 3, pp. 377–445, Jan. 1908.

[27] H. F. Sleiman and N. C. Seeman, “DNA nanotechnology,” *Nat. Rev. Mater.*, vol. 3, p. 17068, Nov. 2017.

[28] F. Hong, F. Zhang, Y. Liu, and H. Yan, “DNA Origami: Scaffolds for Creating Higher Order Structures,” *Chem. Rev.*, Jun. 2017.

[29] L. L. Ong *et al.*, “Programmable self-assembly of three-dimensional nanostructures from 10,000 unique components,” *Nature*, vol. 552, no. 7683, p. 72, Dec. 2017.

[30] G. Tikhomirov, P. Petersen, and L. Qian, “Fractal assembly of micrometre-scale DNA origami arrays with arbitrary patterns,” *Nature*, vol. 552, no. 7683, p. 67, Dec. 2017.

[31] K. F. Wagenbauer, C. Sigl, and H. Dietz, “Gigadalton-scale shape-programmable DNA assemblies,” *Nature*, vol. 552, no. 7683, p. 78, Dec. 2017.

[32] T. L. Schmidt *et al.*, “Scalable amplification of strand subsets from chip-synthesized oligonucleotide libraries,” *Nat. Commun.*, vol. 6, p. 8634, Nov. 2015.

[33] F. Praetorius, B. Kick, K. L. Behler, M. N. Honemann, D. Weuster-Botz, and H. Dietz, “Biotechnological mass production of DNA origami,” *Nature*, vol. 552, no. 7683, p. 84, Dec. 2017.

[34] R. M. Zadegan and M. L. Norton, “Structural DNA Nanotechnology: From Design to Applications,” *Int. J. Mol. Sci.*, vol. 13, no. 6, pp. 7149–7162, Jun. 2012.

[35] A. V. Pinheiro, D. Han, W. M. Shih, and H. Yan, “Challenges and opportunities for structural DNA nanotechnology,” *Nat. Nanotechnol.*, vol. 6, no. 12, p. 763, Dec. 2011.

[36] R. Dahm, “Discovering DNA: Friedrich Miescher and the early years of nucleic acid research,” *Hum. Genet.*, vol. 122, no. 6, pp. 565–581, Jan. 2008.

[37] F. H. C. Crick and J. D. Watson, “Molecular Structure of Nucleic Acids: A Structure for Deoxyribose Nucleic Acid,” *Nature*, vol. 171, no. 4356, p. 737, Apr. 1953.

[38] R. E. Franklin and R. G. Gosling, “Molecular Configuration in Sodium Thymonucleate,” *Nature*, vol. 171, no. 4356, pp. 740–741, Apr. 1953.

[39] M. Mandelkern, J. G. Elias, D. Eden, and D. M. Crothers, “The dimensions of DNA in solution,” *J. Mol. Biol.*, vol. 152, no. 1, pp. 153–161, Oct. 1981.

[40] L. Pray, “Discovery of DNA structure and function: Watson and Crick,” *Nat. Educ.*, vol. 1, no. 1, p. 100, 2008.

[41] C. Broka *et al.*, “Crystal structure analysis of a complete turn of B-DNA,” *Nature*, vol. 287, no. 5784, p. 755, Oct. 1980.

[42] C. O. Pabo and R. T. Sauer, “Protein-DNA Recognition,” *Annu. Rev. Biochem.*, vol. 53, no. 1, pp. 293–321, Jun. 1984.

[43] A. Ghosh and M. Bansal, “A glossary of DNA structures from A to Z,” *Acta Crystallogr. D Biol. Crystallogr.*, vol. 59, no. 4, pp. 620–626, Apr. 2003.

[44] H. S. Basu, B. G. Feuerstein, D. A. Zarling, R. H. Shaffer, and L. J. Marton, “Recognition of Z-RNA and Z-DNA Determinants by Polyamines in Solution: Experimental and Theoretical Studies,” *J. Biomol. Struct. Dyn.*, vol. 6, no. 2, pp. 299–309, Oct. 1988.

[45] F. H. C. Crick and J. D. Watson, “The complementary structure of deoxyribonucleic acid,” *Proc R Soc Lond A*, vol. 223, no. 1152, pp. 80–96, Apr. 1954.

[46] A. Klug, “The Discovery of the DNA Double Helix,” *J. Mol. Biol.*, vol. 335, no. 1, pp. 3–26, Jan. 2004.

[47] J. Šponer, J. Leszczynski, and P. Hobza, “Hydrogen Bonding and Stacking of DNA Bases: A Review of Quantum-chemical ab initio Studies,” *J. Biomol. Struct. Dyn.*, vol. 14, no. 1, pp. 117–135, Aug. 1996.

[48] George A. Jeffrey and W. Saenger, *Hydrogen Bonding in Biological Structures*. Springer Berlin Heidelberg, 1991.

[49] E. T. Kool, “Hydrogen Bonding, Base Stacking, and Steric Effects in DNA Replication,” *Annu. Rev. Biophys. Biomol. Struct.*, vol. 30, no. 1, pp. 1–22, 2001.

[50] J. John SantaLucia and D. Hicks, “The Thermodynamics of DNA Structural Motifs,” *Annu. Rev. Biophys. Biomol. Struct.*, vol. 33, no. 1, pp. 415–440, 2004.

[51] P. Yakovchuk, E. Protozanova, and M. D. Frank-Kamenetskii, “Base-stacking and base-pairing contributions into thermal stability of the DNA double helix,” *Nucleic Acids Res.*, vol. 34, no. 2, pp. 564–574, 2006.

[52] N. C. Seeman, “Nucleic acid junctions and lattices,” *J. Theor. Biol.*, vol. 99, no. 2, pp. 237–247, Nov. 1982.

[53] N. C. Seeman, “DNA in a material world,” *Nature*, vol. 421, no. 6921, pp. 427–431, Jan. 2003.

[54] J. Chen and N. C. Seeman, “Synthesis from DNA of a molecule with the connectivity of a cube,” *Nature*, vol. 350, no. 6319, p. 631, Apr. 1991.

[55] T. J. Fu and N. C. Seeman, “DNA double-crossover molecules,” *Biochemistry (Mosc.)*, vol. 32, no. 13, pp. 3211–3220, Apr. 1993.

[56] C. Mao, J. H. Reif, N. C. Seeman, and T. H. LaBean, “Logical computation using algorithmic self-assembly of DNA triple-crossover molecules,” *Nature*, vol. 407, no. 6803, p. 493, Sep. 2000.

[57] T. H. LaBean *et al.*, “Construction, Analysis, Ligation, and Self-Assembly of DNA Triple Crossover Complexes,” *J. Am. Chem. Soc.*, vol. 122, no. 9, pp. 1848–1860, Mar. 2000.

[58] E. Winfree, F. Liu, L. A. Wenzler, and N. C. Seeman, “Design and self-assembly of two-dimensional DNA crystals,” *Nature*, vol. 394, no. 6693, p. 539, Aug. 1998.

[59] C. Lin, Y. Liu, S. Rinker, and H. Yan, “DNA Tile Based Self-Assembly: Building Complex Nanoarchitectures,” *ChemPhysChem*, vol. 7, no. 8, pp. 1641–1647, Aug. 2006.

[60] B. Wei, M. Dai, and P. Yin, “Complex shapes self-assembled from single-stranded DNA tiles,” *Nature*, vol. 485, no. 7400, p. 623, May 2012.

[61] W. M. Shih, J. D. Quispe, and G. F. Joyce, “A 1.7-kilobase single-stranded DNA that folds into a nanoscale octahedron,” *Nature*, vol. 427, no. 6975, pp. 618–621, Feb. 2004.

[62] P. W. K. Rothemund, “Folding DNA to create nanoscale shapes and patterns,” *Nature*, vol. 440, no. 7082, pp. 297–302, Mar. 2006.

[63] S. M. Douglas, H. Dietz, T. Liedl, B. Hogberg, F. Graf, and W. M. Shih, “Self-assembly of DNA into nanoscale three-dimensional shapes,” *Nature*, vol. 459, no. 7245, pp. 414–418, May 2009.

[64] Y. Ke *et al.*, “Multilayer DNA Origami Packed on a Square Lattice,” *J. Am. Chem. Soc.*, vol. 131, no. 43, p. 15903, Nov. 2009.

[65] S. M. Douglas, A. H. Marblestone, S. Teerapittayanon, A. Vazquez, G. M. Church, and W. M. Shih, “Rapid prototyping of 3D DNA-origami shapes with caDNAno,” *Nucleic Acids Res.*, vol. 37, no. 15, pp. 5001–5006, Aug. 2009.

[66] H. Dietz, S. M. Douglas, and W. M. Shih, “Folding DNA into Twisted and Curved Nanoscale Shapes,” *Science*, vol. 325, no. 5941, pp. 725–730, Aug. 2009.

[67] T. Gerling, K. F. Wagenbauer, A. M. Neuner, and H. Dietz, “Dynamic DNA devices and assemblies formed by shape-complementary, non–base pairing 3D components,” *Science*, vol. 347, no. 6229, pp. 1446–1452, Mar. 2015.

[68] E. Benson *et al.*, “DNA rendering of polyhedral meshes at the nanoscale,” *Nature*, vol. 523, no. 7561, pp. 441–444, Jul. 2015.

[69] T. Liedl, B. Högberg, J. Tytell, D. E. Ingber, and W. M. Shih, “Self-assembly of 3D prestressed tensegrity structures from DNA,” *Nat. Nanotechnol.*, vol. 5, no. 7, pp. 520–524, Jul. 2010.

[70] D. Han *et al.*, “DNA Gridiron Nanostructures Based on Four-Arm Junctions,” *Science*, vol. 339, no. 6126, pp. 1412–1415, Mar. 2013.

[71] E. S. Andersen *et al.*, “Self-assembly of a nanoscale DNA box with a controllable lid,” *Nature*, vol. 459, no. 7243, p. 73, May 2009.

[72] M. Matthies, N. P. Agarwal, and T. L. Schmidt, “Design and Synthesis of Triangulated DNA Origami Trusses,” *Nano Lett.*, vol. 16, no. 3, pp. 2108–2113, Mar. 2016.

[73] F. Zhang *et al.*, “Complex wireframe DNA origami nanostructures with multi-arm junction vertices,” *Nat. Nanotechnol.*, vol. 10, no. 9, p. 779, Sep. 2015.

[74] B. Ding, Z. Deng, H. Yan, S. Cabrini, R. N. Zuckermann, and J. Bokor, “Gold Nanoparticle Self-Similar Chain Structure Organized by DNA Origami,” *J. Am. Chem. Soc.*, vol. 132, no. 10, pp. 3248–3249, Mar. 2010.

[75] A. Kuzyk *et al.*, “DNA-based self-assembly of chiral plasmonic nanostructures with tailored optical response,” *Nature*, vol. 483, no. 7389, pp. 311–314, Mar. 2012.

[76] Q. Liu, C. Song, Z.-G. Wang, N. Li, and B. Ding, “Precise organization of metal nanoparticles on DNA origami template,” *Methods*, vol. 67, no. 2, pp. 205–214, May 2014.

[77] D. Huang, M. Freeley, and M. Palma, “DNA-Mediated Patterning of Single Quantum Dot Nanoarrays: A Reusable Platform for Single-Molecule Control,” *Sci. Rep.*, vol. 7, p. 45591, Mar. 2017.

[78] H. Bui *et al.*, “Programmable Periodicity of Quantum Dot Arrays with DNA Origami Nanotubes,” *Nano Lett.*, vol. 10, no. 9, pp. 3367–3372, Sep. 2010.

[79] C. Steinhauer, R. Jungmann, T. L. Sobey, F. C. Simmel, and P. Tinnefeld, “DNA Origami as a Nanoscopic Ruler for Super-Resolution Microscopy,” *Angew. Chem. Int. Ed.*, vol. 48, no. 47, pp. 8870–8873, Nov. 2009.

[80] T. Zhang *et al.*, “DNA-Based Self-Assembly of Fluorescent Nanodiamonds,” *J. Am. Chem. Soc.*, vol. 137, no. 31, pp. 9776–9779, Aug. 2015.

[81] P. K. Dutta *et al.*, “A DNA-Directed Light-Harvesting/Reaction Center System,” *J. Am. Chem. Soc.*, vol. 136, no. 47, pp. 16618–16625, Nov. 2014.

[82] A. Kuzyk, K. T. Laitinen, and P. Törmä, “DNA origami as a nanoscale template for protein assembly,” *Nanotechnology*, vol. 20, no. 23, p. 235305, May 2009.

[83] H. T. Maune *et al.*, “Self-assembly of carbon nanotubes into two-dimensional geometries using DNA origami templates,” *Nat. Nanotechnol.*, vol. 5, no. 1, pp. 61–66, Jan. 2010.

[84] J. Zessin *et al.*, “Tunable Fluorescence of a Semiconducting Polythiophene Positioned on DNA Origami,” *Nano Lett.*, vol. 17, no. 8, pp. 5163–5170, Aug. 2017.

[85] R. Schreiber *et al.*, “Hierarchical assembly of metal nanoparticles, quantum dots and organic dyes using DNA origami scaffolds,” *Nat. Nanotechnol.*, vol. 9, no. 1, pp. 74–78, Dec. 2013.

[86] S. Pal, Z. Deng, H. Wang, S. Zou, Y. Liu, and H. Yan, “DNA Directed Self-Assembly of Anisotropic Plasmonic Nanostructures,” *J. Am. Chem. Soc.*, vol. 133, no. 44, pp. 17606–17609, Nov. 2011.

[87] S. Pal, Z. Deng, B. Ding, H. Yan, and Y. Liu, “DNA-Origami-Directed Self-Assembly of Discrete Silver-Nanoparticle Architectures,” *Angew. Chem. Int. Ed.*, vol. 49, no. 15, pp. 2700–2704, Apr. 2010.

[88] C. Heck *et al.*, “Gold Nanolenses Self-Assembled by DNA Origami,” *ACS Photonics*, vol. 4, no. 5, pp. 1123–1130, May 2017.

[89] V. V. Thacker *et al.*, “DNA origami based assembly of gold nanoparticle dimers for surface-enhanced Raman scattering,” *Nat. Commun.*, vol. 5, Mar. 2014.

[90] G. P. Acuna, F. M. Moller, P. Holzmeister, S. Beater, B. Lalkens, and P. Tinnefeld, "Fluorescence Enhancement at Docking Sites of DNA-Directed Self-Assembled Nanoantennas," *Science*, vol. 338, no. 6106, pp. 506–510, Oct. 2012.

[91] E.-M. Roller, L. K. Khorashad, M. Fedoruk, R. Schreiber, A. O. Govorov, and T. Liedl, "DNA-Assembled Nanoparticle Rings Exhibit Electric and Magnetic Resonances at Visible Frequencies," *Nano Lett.*, vol. 15, no. 2, pp. 1368–1373, Feb. 2015.

[92] A. Kuzyk, R. Schreiber, H. Zhang, A. O. Govorov, T. Liedl, and N. Liu, "Reconfigurable 3D plasmonic metamolecules," *Nat. Mater.*, vol. 13, no. 9, p. 862, Sep. 2014.

[93] P. Kühler, E.-M. Roller, R. Schreiber, T. Liedl, T. Lohmüller, and J. Feldmann, "Plasmonic DNA-Origami Nanoantennas for Surface-Enhanced Raman Spectroscopy," *Nano Lett.*, vol. 14, no. 5, pp. 2914–2919, May 2014.

[94] X. Shen *et al.*, "Rolling Up Gold Nanoparticle-Dressed DNA Origami into Three-Dimensional Plasmonic Chiral Nanostructures," *J. Am. Chem. Soc.*, vol. 134, no. 1, pp. 146–149, Jan. 2012.

[95] M. Hentschel, M. Schäferling, X. Duan, H. Giessen, and N. Liu, "Chiral plasmonics," *Sci. Adv.*, vol. 3, no. 5, p. e1602735, May 2017.

[96] C. Zhou, X. Duan, and N. Liu, "DNA-Nanotechnology-Enabled Chiral Plasmonics: From Static to Dynamic," *Acc. Chem. Res.*, Sep. 2017.

[97] X. Shen *et al.*, "Three-Dimensional Plasmonic Chiral Tetramers Assembled by DNA Origami," *Nano Lett.*, vol. 13, no. 5, pp. 2128–2133, May 2013.

[98] X. Lan, X. Lu, C. Shen, Y. Ke, W. Ni, and Q. Wang, "Au Nanorod Helical Superstructures with Designed Chirality," *J. Am. Chem. Soc.*, vol. 137, no. 1, pp. 457–462, Jan. 2015.

[99] C. Shen, X. Lan, C. Zhu, W. Zhang, L. Wang, and Q. Wang, "Spiral Patterning of Au Nanoparticles on Au Nanorod Surface to Form Chiral AuNR@AuNP Helical Superstructures Templated by DNA Origami," *Adv. Mater.*, vol. 29, no. 16, Apr. 2017.

[100] M. Quinten, A. Leitner, J. R. Krenn, and F. R. Aussenegg, "Electromagnetic energy transport via linear chains of silver nanoparticles," *Opt. Lett.*, vol. 23, no. 17, p. 1331, Sep. 1998.

[101] S. A. Maier *et al.*, "Local detection of electromagnetic energy transport below the diffraction limit in metal nanoparticle plasmon waveguides," *Nat. Mater.*, vol. 2, no. 4, pp. 229–232, Apr. 2003.

[102] C. Girard and R. Quidant, "Near–field optical transmittance of metal particle chain waveguides," *Opt. Express*, vol. 12, no. 25, pp. 6141–6146, Dec. 2004.

[103] W. Nomura, M. Ohtsu, and T. Yatsui, "Nanodot coupler with a surface plasmon polariton condenser for optical far/near-field conversion," *Appl. Phys. Lett.*, vol. 86, no. 18, p. 181108, May 2005.

[104] K. Li, M. I. Stockman, and D. J. Bergman, "Self-Similar Chain of Metal Nanospheres as an Efficient Nanolens," *Phys. Rev. Lett.*, vol. 91, no. 22, Nov. 2003.

[105] W.-S. Chang, L. S. Slaughter, B. P. Khanal, P. Manna, E. R. Zubarev, and S. Link, "One-Dimensional Coupling of Gold Nanoparticle Plasmons in Self-Assembled Ring Superstructures," *Nano Lett.*, vol. 9, no. 3, pp. 1152–1157, Mar. 2009.

[106] D. Solis *et al.*, "Electromagnetic Energy Transport in Nanoparticle Chains via Dark Plasmon Modes," *Nano Lett.*, vol. 12, no. 3, pp. 1349–1353, Mar. 2012.

[107] D. Solis *et al.*, "Turning the Corner: Efficient Energy Transfer in Bent Plasmonic Nanoparticle Chain Waveguides," *Nano Lett.*, vol. 13, no. 10, pp. 4779–4784, Oct. 2013.

[108] S. J. Barrow, A. M. Funston, D. E. Gómez, T. J. Davis, and P. Mulvaney, "Surface Plasmon Resonances in Strongly Coupled Gold Nanosphere Chains from Monomer to Hexamer," *Nano Lett.*, vol. 11, no. 10, pp. 4180–4187, Oct. 2011.

[109] W. P. Klein *et al.*, "Multiscaffold DNA Origami Nanoparticle Waveguides," *Nano Lett.*, vol. 13, no. 8, pp. 3850–3856, Aug. 2013.

[110] K. Vogele, J. List, G. Pardatscher, N. B. Holland, F. C. Simmel, and T. Pirzer, "Self-Assembled Active Plasmonic Waveguide with a Peptide-Based Thermomechanical Switch," *ACS Nano*, vol. 10, no. 12, pp. 11377–11384, Dec. 2016.

[111] E.-M. Roller, L. V. Besteiro, C. Pupp, L. K. Khorashad, A. O. Govorov, and T. Liedl, "Hotspot-mediated non-dissipative and ultrafast plasmon passage," *Nat. Phys.*, vol. 13, no. 8, pp. 761–765, May 2017.

[112] W.-S. Chang, B. Willingham, L. S. Slaughter, S. Dominguez-Medina, P. Swanglap, and S. Link, "Radiative and Nonradiative Properties of Single Plasmonic Nanoparticles and Their Assemblies," *Acc. Chem. Res.*, vol. 45, no. 11, pp. 1936–1945, Nov. 2012.

[113] C. Hanske *et al.*, "Strongly Coupled Plasmonic Modes on Macroscopic Areas via Template-Assisted Colloidal Self-Assembly," *Nano Lett.*, vol. 14, no. 12, pp. 6863–6871, Dec. 2014.

[114] S. J. Barrow, D. Rossouw, A. M. Funston, G. A. Botton, and P. Mulvaney, "Mapping Bright and Dark Modes in Gold Nanoparticle Chains using Electron Energy Loss Spectroscopy.," *Nano Lett.*, vol. 14, no. 7, pp. 3799–3808, Jul. 2014.

[115] F. J. García de Abajo, "Optical excitations in electron microscopy," *Rev. Mod. Phys.*, vol. 82, no. 1, pp. 209–275, Feb. 2010.

[116] S. W. Hell, "Far-Field Optical Nanoscopy," *Science*, vol. 316, no. 5828, pp. 1153–1158, May 2007.

[117] W. Chao, B. D. Harteneck, J. A. Liddle, E. H. Anderson, and D. T. Attwood, "Soft X-ray microscopy at a spatial resolution better than 15 nm," *Nature*, vol. 435, no. 7046, pp. 1210–1213, Jun. 2005.

[118] N. Mauser and A. Hartschuh, "Tip-enhanced near-field optical microscopy," *Chem Soc Rev*, vol. 43, no. 4, pp. 1248–1262, Feb. 2014.

[119] G. Hörmandinger, "Imaging of the Cu (111) surface state in scanning tunneling microscopy," *Phys. Rev. B*, vol. 49, no. 19, p. 13897, May 1994.

[120] S. Lazar, G. A. Botton, and H. W. Zandbergen, "Enhancement of resolution in core-loss and low-loss spectroscopy in a monochromated microscope," *Ultramicroscopy*, vol. 106, no. 11, pp. 1091–1103, Oct. 2006.

[121] M. Aeschlimann *et al.*, "Adaptive subwavelength control of nano-optical fields," *Nature*, vol. 446, no. 7133, pp. 301–304, Mar. 2007.

[122] L. Douillard *et al.*, "Short Range Plasmon Resonators Probed by Photoemission Electron Microscopy," *Nano Lett.*, vol. 8, no. 3, pp. 935–940, Mar. 2008.

[123] B. E. A. Saleh and M. C. Teich, *Fundamentals of Photonics.* New York: Wiley, 1991.

[124] R. Zia, J. A. Schuller, A. Chandran, and M. L. Brongersma, “Plasmonics: the next chip-scale technology,” *Mater. Today*, vol. 9, no. 7, pp. 20–27, Aug. 2006.

[125] D. K. Gramotnev and S. I. Bozhevolnyi, “Plasmonics beyond the diffraction limit,” *Nat. Photonics*, vol. 4, no. 2, pp. 83–91, Feb. 2010.

[126] W. L. Barnes, A. Dereux, and T. W. Ebbesen, “Surface plasmon subwavelength optics,” *nature*, vol. 424, no. 6950, p. 824, 2003.

[127] E. Ozbay, “Plasmonics: merging photonics and electronics at nanoscale dimensions,” *science*, vol. 311, no. 5758, pp. 189–193, 2006.

[128] A. V. Zayats and I. I. Smolyaninov, “Near-field photonics: surface plasmon polaritons and localized surface plasmons,” *J. Opt. Pure Appl. Opt.*, vol. 5, no. 4, p. S16, 2003.

[129] S. A. Maier, P. G. Kik, and H. A. Atwater, “Optical pulse propagation in metal nanoparticle chain waveguides,” *Phys. Rev. B*, vol. 67, no. 20, p. 205402, May 2003.

[130] S. A. Maier, P. G. Kik, and H. A. Atwater, “Observation of coupled plasmon-polariton modes in Au nanoparticle chain waveguides of different lengths: Estimation of waveguide loss,” *Appl. Phys. Lett.*, vol. 81, no. 9, pp. 1714–1716, Aug. 2002.

[131] M. Pelton, J. Aizpurua, and G. Bryant, “Metal-nanoparticle plasmonics,” *Laser Photonics Rev.*, vol. 2, no. 3, pp. 136–159, Jul. 2008.

[132] S. Eustis and M. A. El-Sayed, “Why gold nanoparticles are more precious than pretty gold: Noble metal surface plasmon resonance and its enhancement of the radiative and nonradiative properties of nanocrystals of different shapes,” *Chem Soc Rev*, vol. 35, no. 3, pp. 209–217, 2006.

[133] N. C. Seeman, “Nanomaterials Based on DNA,” *Annu. Rev. Biochem.*, vol. 79, no. 1, pp. 65–87, Jun. 2010.

[134] C. A. Mirkin, R. L. Letsinger, R. C. Mucic, and J. J. Storhoff, “A DNA-based method for rationally assembling nanoparticles into macroscopic materials,” *Nature*, vol. 382, no. 6592, pp. 607–609, Aug. 1996.

[135] D. Nykypanchuk, M. M. Maye, D. van der Lelie, and O. Gang, “DNA-guided crystallization of colloidal nanoparticles,” *Nature*, vol. 451, no. 7178, pp. 549–552, Jan. 2008.

[136] S. J. Tan, M. J. Campolongo, D. Luo, and W. Cheng, “Building plasmonic nanostructures with DNA,” *Nat. Nanotechnol.*, vol. 6, no. 5, pp. 268–276, May 2011.

[137] J. Chao, Y. Lin, H. Liu, L. Wang, and C. Fan, “DNA-based plasmonic nanostructures,” *Mater. Today*, 2015.

[138] F. N. Gür, F. W. Schwarz, J. Ye, S. Diez, and T. L. Schmidt, “Toward Self-Assembled Plasmonic Devices: High-Yield Arrangement of Gold Nanoparticles on DNA Origami Templates,” *ACS Nano*, vol. 10, no. 5, pp. 5374–5382, May 2016.

[139] M. Kociak and O. Stéphan, “Mapping plasmons at the nanometer scale in an electron microscope,” *Chem. Soc. Rev.*, vol. 43, no. 11, p. 3865, 2014.

[140] Z. Yang, H. Liu, and D. Liu, “Spatial regulation of synthetic and biological nanoparticles by DNA nanotechnology,” *NPG Asia Mater.*, vol. 7, no. 2, p. e161, Feb. 2015.

[141] Y. R. Yang, Y. Liu, and H. Yan, “DNA Nanostructures as Programmable Biomolecular Scaffolds,” *Bioconjug. Chem.*, vol. 26, no. 8, pp. 1381–1395, Aug. 2015.

[142] A. P. Alivisatos *et al.*, “Organization of ‘nanocrystal molecules’ using DNA,” *Nature*, vol. 382, no. 6592, pp. 609–611, Aug. 1996.

[143] S. Takabayashi *et al.*, “High precision and high yield fabrication of dense nanoparticle arrays onto DNA origami at statistically independent binding sites,” *Nanoscale*, vol. 6, no. 22, pp. 13928–13938, Oct. 2014.

[144] J. Prinz *et al.*, “DNA Origami Substrates for Highly Sensitive Surface-Enhanced Raman Scattering,” *J. Phys. Chem. Lett.*, vol. 4, no. 23, pp. 4140–4145, Dec. 2013.

[145] S. M. Douglas, J. J. Chou, and W. M. Shih, “DNA-nanotube-induced alignment of membrane proteins for NMR structure determination,” *Proc. Natl. Acad. Sci.*, vol. 104, no. 16, pp. 6644–6648, Apr. 2007.

[146] F. Mathieu, S. Liao, J. Kopatsch, T. Wang, C. Mao, and N. C. Seeman, “Six-Helix Bundles Designed from DNA,” *Nano Lett.*, vol. 5, no. 4, pp. 661–665, Apr. 2005.

[147] C. E. Castro, H.-J. Su, A. E. Marras, L. Zhou, and J. Johnson, “Mechanical design of DNA nanostructures,” *Nanoscale*, vol. 7, no. 14, pp. 5913–5921, 2015.

[148] J. Turkevich, P. C. Stevenson, and J. Hillier, “A study of the nucleation and growth processes in the synthesis of colloidal gold,” *Discuss. Faraday Soc.*, vol. 11, pp. 55–75, 1951.

[149] S. J. Hurst, A. K. R. Lytton-Jean, and C. A. Mirkin, “Maximizing DNA Loading on a Range of Gold Nanoparticle Sizes,” *Anal. Chem.*, vol. 78, no. 24, pp. 8313–8318, 2006.

[150] A. Aghebat Rafat, T. Pirzer, M. B. Scheible, A. Kostina, and F. C. Simmel, “Surface-Assisted Large-Scale Ordering of DNA Origami Tiles,” *Angew. Chem. Int. Ed.*, vol. 53, no. 29, pp. 7665–7668, Jul. 2014.

[151] J. Hahn, S. F. J. Wickham, W. M. Shih, and S. D. Perrault, “Addressing the Instability of DNA Nanostructures in Tissue Culture,” *ACS Nano*, vol. 8, no. 9, pp. 8765–8775, Sep. 2014.

[152] B. Teschome, S. Facsko, K. V. Gothelf, and A. Keller, “Alignment of Gold Nanoparticle-Decorated DNA Origami Nanotubes: Substrate Prepatterning versus Molecular Combing,” *Langmuir*, vol. 31, no. 46, pp. 12823–12829, Nov. 2015.

[153] J. Sharma, R. Chhabra, C. S. Andersen, K. V. Gothelf, H. Yan, and Y. Liu, “Toward Reliable Gold Nanoparticle Patterning On Self-Assembled DNA Nanoscaffold,” *J. Am. Chem. Soc.*, vol. 130, no. 25, pp. 7820–7821, Jun. 2008.

[154] E. P. Gates, J. K. Jensen, J. N. Harb, and A. T. Woolley, “Optimizing gold nanoparticle seeding density on DNA origami,” *RSC Adv*, vol. 5, no. 11, pp. 8134–8141, 2015.

[155] S. D. Perrault and W. C. W. Chan, “Synthesis and Surface Modification of Highly Monodispersed, Spherical Gold Nanoparticles of 50−200 nm,” *J. Am. Chem. Soc.*, vol. 131, no. 47, pp. 17042–17043, Dec. 2009.

[156] N. P. Agarwal, M. Matthies, F. N. Gür, K. Osada, and T. L. Schmidt, “Block Copolymer Micellization as a Protection Strategy for DNA Origami,” *Angew. Chem. Int. Ed.*, vol. 56, no. 20, pp. 5460–5464, May 2017.

[157] R. Schneider, T. Glaser, M. Berndt, and S. Diez, “Using a quartz paraboloid for versatile wide-field TIR microscopy with sub-nanometer localization accuracy,” *Opt. Express*, vol. 21, no. 3, pp. 3523–3539, Feb. 2013.

[158] *MATLAB 8.0 and Statistics Toolbox 8.1. The MathWorks Inc.* Natick, Massachusetts, 2014.

[159] F. N. Gür *et al.*, “Self-assembled plasmonic waveguides for excitation of fluorescent nanodiamonds,” *arXiv:1712.09141*, Dec. 2017.

[160] P. E. Batson, “Simultaneous STEM imaging and electron energy-loss spectroscopy with atomic-column sensitivity,” *Nature*, vol. 366, no. 6457, pp. 727–728, Dec. 1993.

[161] R.F. Egerton, *Electron Energy-Loss Spectroscopy in the Electron Microscope*. Springer, 2011.

[162] N. D. Browning, D. J. Wallis, P. D. Nellist, and S. J. Pennycook, “EELS in the STEM: Determination of materials properties on the atomic scale,” *Micron*, vol. 28, no. 5, pp. 333–348, 1997.

[163] K. Suenaga *et al.*, “Element-Selective Single Atom Imaging,” *Science*, vol. 290, no. 5500, pp. 2280–2282, Dec. 2000.

[164] K. Kimoto, T. Asaka, T. Nagai, M. Saito, Y. Matsui, and K. Ishizuka, “Element-selective imaging of atomic columns in a crystal using STEM and EELS,” *Nature*, vol. 450, no. 7170, pp. 702–704, Nov. 2007.

[165] M. Varela *et al.*, “Spectroscopic Imaging of Single Atoms Within a Bulk Solid,” *Phys. Rev. Lett.*, vol. 92, no. 9, p. 095502, Mar. 2004.

[166] K. Suenaga *et al.*, “Visualizing and identifying single atoms using electron energy-loss spectroscopy with low accelerating voltage,” *Nat. Chem.*, vol. 1, no. 5, pp. 415–418, Aug. 2009.

[167] R. F. Egerton, “New techniques in electron energy-loss spectroscopy and energy-filtered imaging,” *Micron*, vol. 34, no. 3–5, pp. 127–139, Apr. 2003.

[168] V. J. Keast, “Application of EELS in Materials Science,” *Mater. Charact.*, vol. 73, pp. 1–7, Nov. 2012.

[169] B. Schaffer, W. Grogger, G. Kothleitner, and F. Hofer, “Comparison of EFTEM and STEM EELS plasmon imaging of gold nanoparticles in a monochromated TEM,” *Ultramicroscopy*, vol. 110, no. 8, pp. 1087–1093, Jul. 2010.

[170] B. Schaffer, U. Hohenester, A. Trügler, and F. Hofer, “High-resolution surface plasmon imaging of gold nanoparticles by energy-filtered transmission electron microscopy,” *Phys. Rev. B*, vol. 79, no. 4, Jan. 2009.

[171] D. Shindo and T. Oikawa, “Energy Dispersive X-ray Spectroscopy,” *SpringerLink*, pp. 81–102, 2002.

[172] E. J. R. Vesseur, R. de Waele, M. Kuttge, and A. Polman, “Direct Observation of Plasmonic Modes in Au Nanowires Using High-Resolution Cathodoluminescence Spectroscopy,” *Nano Lett.*, vol. 7, no. 9, pp. 2843–2846, Sep. 2007.

[173] R. Gómez-Medina, N. Yamamoto, M. Nakano, and F. J. García de Abajo, “Mapping plasmons in nanoantennas via cathodoluminescence,” *New J. Phys.*, vol. 10, no. 10, p. 105009, Oct. 2008.

[174] “EELS.info.” [Online]. Available: http://www.eels.info/. [Accessed: 12-Dec-2017].

[175] M. Bosman, V. J. Keast, J. L. García-Muñoz, A. J. D'Alfonso, S. D. Findlay, and L. J. Allen, "Two-Dimensional Mapping of Chemical Information at Atomic Resolution," *Phys. Rev. Lett.*, vol. 99, no. 8, Aug. 2007.

[176] M. Bosman, V. J. Keast, M. Watanabe, A. I. Maaroof, and M. B. Cortie, "Mapping surface plasmons at the nanometre scale with an electron beam," *Nanotechnology*, vol. 18, no. 16, p. 165505, Mar. 2007.

[177] J. Nelayah *et al.*, "Mapping surface plasmons on a single metallic nanoparticle," *Nat. Phys.*, vol. 3, no. 5, pp. 348–353, May 2007.

[178] C. Colliex, M. Kociak, and O. Stéphan, "Electron Energy Loss Spectroscopy imaging of surface plasmons at the nanometer scale," *Ultramicroscopy*, vol. 162, pp. A1–A24, Mar. 2016.

[179] S. Raza, "Probing plasmonic nanostructures with electron energy-loss spectroscopy," Technical University of Denmark, 2014.

[180] S. Raza *et al.*, "Multipole plasmons and their disappearance in few-nanometre silver nanoparticles," *Nat. Commun.*, vol. 6, p. 8788, Nov. 2015.

[181] S. M. Collins and P. A. Midgley, "Surface plasmon excitations in metal spheres: Direct comparison of light scattering and electron energy-loss spectroscopy by modal decomposition," *Phys. Rev. B*, vol. 87, no. 23, Jun. 2013.

[182] B. S. Guiton *et al.*, "Correlated Optical Measurements and Plasmon Mapping of Silver Nanorods," *Nano Lett.*, vol. 11, no. 8, pp. 3482–3488, Aug. 2011.

[183] F.-P. Schmidt, H. Ditlbacher, U. Hohenester, A. Hohenau, F. Hofer, and J. R. Krenn, "Universal dispersion of surface plasmons in flat nanostructures," *Nat. Commun.*, vol. 5, Apr. 2014.

[184] S. Raza, M. Esfandyarpour, A. L. Koh, N. A. Mortensen, M. L. Brongersma, and S. I. Bozhevolnyi, "Electron energy-loss spectroscopy of branched gap plasmon resonators," *Nat. Commun.*, vol. 7, p. 13790, Dec. 2016.

[185] F. von Cube, J. Niegemann, S. Irsen, D. C. Bell, and S. Linden, "Angular-resolved electron energy loss spectroscopy on a split-ring resonator," *Phys. Rev. B*, vol. 89, no. 11, Mar. 2014.

[186] J. Martin, M. Kociak, Z. Mahfoud, J. Proust, D. Gérard, and J. Plain, "High-Resolution Imaging and Spectroscopy of Multipolar Plasmonic Resonances in Aluminum Nanoantennas," *Nano Lett.*, vol. 14, no. 10, pp. 5517–5523, Oct. 2014.

[187] M. Zhang *et al.*, "High-Density 2D Homo- and Hetero- Plasmonic Dimers with Universal Sub-10-nm Gaps," *ACS Nano*, vol. 9, no. 9, pp. 9331–9339, Sep. 2015.

[188] A. L. Koh, A. I. Fernández-Domínguez, D. W. McComb, S. A. Maier, and J. K. W. Yang, "High-Resolution Mapping of Electron-Beam-Excited Plasmon Modes in Lithographically Defined Gold Nanostructures," *Nano Lett.*, vol. 11, no. 3, pp. 1323–1330, Mar. 2011.

[189] J. A. Scholl *et al.*, "Evolution of Plasmonic Metamolecule Modes in the Quantum Tunneling Regime," *ACS Nano*, vol. 10, no. 1, pp. 1346–1354, Jan. 2016.

[190] H. Duan, A. I. Fernández-Domínguez, M. Bosman, S. A. Maier, and J. K. W. Yang, "Nanoplasmonics: Classical down to the Nanometer Scale," *Nano Lett.*, vol. 12, no. 3, pp. 1683–1689, Mar. 2012.

[191] A. L. Koh *et al.*, "Electron Energy-Loss Spectroscopy (EELS) of Surface Plasmons in Single Silver Nanoparticles and Dimers: Influence of Beam Damage and Mapping of Dark Modes," *ACS Nano*, vol. 3, no. 10, pp. 3015–3022, Oct. 2009.

[192] S. Kadkhodazadeh, J. R. de Lasson, M. Beleggia, H. Kneipp, J. B. Wagner, and K. Kneipp, "Scaling of the Surface Plasmon Resonance in Gold and Silver Dimers Probed by EELS," *J. Phys. Chem. C*, vol. 118, no. 10, pp. 5478–5485, Mar. 2014.

[193] P. Nordlander, C. Oubre, E. Prodan, K. Li, and M. I. Stockman, "Plasmon Hybridization in Nanoparticle Dimers," *Nano Lett.*, vol. 4, no. 5, pp. 899–903, May 2004.

[194] F. Song *et al.*, "Visualizing Plasmon Coupling in Closely Spaced Chains of Ag Nanoparticles by Electron Energy-Loss Spectroscopy," *Small*, vol. 6, no. 3, pp. 446–451, Feb. 2010.

[195] M.-W. Chu, V. Myroshnychenko, C. H. Chen, J.-P. Deng, C.-Y. Mou, and F. J. García de Abajo, "Probing Bright and Dark Surface-Plasmon Modes in Individual and Coupled Noble Metal Nanoparticles Using an Electron Beam," *Nano Lett.*, vol. 9, no. 1, pp. 399–404, Jan. 2009.

[196] A. M. Steiner *et al.*, "Macroscopic Strain-Induced Transition from Quasi-infinite Gold Nanoparticle Chains to Defined Plasmonic Oligomers," *ACS Nano*, vol. 11, no. 9, pp. 8871–8880, Sep. 2017.

[197] B. Willingham and S. Link, "Energy transport in metal nanoparticle chains via sub-radiant plasmon modes," *Opt. Express*, vol. 19, no. 7, pp. 6450–6461, 2011.

[198] S. Raza and N. A. Mortensen, "Interplay of nonlocal response, damping, and low group velocity in surface-plasmon polaritons," presented at the Slow Light, Fast Light, and Opto-Atomic Precision Metrology IX, 2016, vol. 9763, p. 97630Y.

[199] A. Teulle *et al.*, "Multimodal plasmonics in fused colloidal networks," *Nat. Mater.*, vol. 14, no. 1, p. nmat4114, Oct. 2014.

[200] U. Hohenester, "Simulating electron energy loss spectroscopy with the MNPBEM toolbox," *Comput. Phys. Commun.*, vol. 185, no. 3, pp. 1177–1187, Mar. 2014.

[201] F. J. García de Abajo and A. Howie, "Retarded field calculation of electron energy loss in inhomogeneous dielectrics," *Phys. Rev. B*, vol. 65, no. 11, Mar. 2002.

[202] P. B. Johnson and R.-W. Christy, "Optical constants of the noble metals," *Phys. Rev. B*, vol. 6, no. 12, p. 4370, 1972.

[203] T. Coenen, E. J. R. Vesseur, A. Polman, and A. F. Koenderink, "Directional Emission from Plasmonic Yagi–Uda Antennas Probed by Angle-Resolved Cathodoluminescence Spectroscopy," *Nano Lett.*, vol. 11, no. 9, pp. 3779–3784, Sep. 2011.

[204] T. Coenen, D. T. Schoen, B. J. M. Brenny, A. Polman, and M. L. Brongersma, "Combined electron energy-loss and cathodoluminescence spectroscopy on individual and composite plasmonic nanostructures," *Phys. Rev. B*, vol. 93, no. 19, May 2016.

[205] V. Myroshnychenko *et al.*, "Plasmon Spectroscopy and Imaging of Individual Gold Nanodecahedra: A Combined Optical Microscopy, Cathodoluminescence, and Electron Energy-Loss Spectroscopy Study," *Nano Lett.*, vol. 12, no. 8, pp. 4172–4180, Aug. 2012.

[206] M. Kuttge *et al.*, "Local density of states, spectrum, and far-field interference of surface plasmon polaritons probed by cathodoluminescence," *Phys. Rev. B*, vol. 79, no. 11, Mar. 2009.

[207] E. J. R. Vesseur, J. Aizpurua, T. Coenen, A. Reyes-Coronado, P. E. Batson, and A. Polman, "Plasmonic excitation and manipulation with an electron beam," *MRS Bull.*, vol. 37, no. 08, pp. 752–760, Aug. 2012.

[208] I. Aharonovich, A. D. Greentree, and S. Prawer, "Diamond photonics," *Nat. Photonics*, vol. 5, no. 7, pp. 397–405, Jun. 2011.

[209] K. Beha *et al.*, "Diamond nanophotonics," *Beilstein J. Nanotechnol.*, vol. 3, pp. 895–908, Dec. 2012.

[210] S. Prawer and A. D. Greentree, "APPLIED PHYSICS: Diamond for Quantum Computing," *Science*, vol. 320, no. 5883, pp. 1601–1602, Jun. 2008.

[211] J. Wrachtrup and F. Jelezko, "Processing quantum information in diamond," *J. Phys. Condens. Matter*, vol. 18, no. 21, pp. S807–S824, May 2006.

[212] C. Santori, P. E. Barclay, K.-M. C. Fu, R. G. Beausoleil, S. Spillane, and M. Fisch, "Nanophotonics for quantum optics using nitrogen-vacancy centers in diamond," *Nanotechnology*, vol. 21, no. 27, p. 274008, Jul. 2010.

[213] A. Huck, S. Kumar, A. Shakoor, and U. L. Andersen, "Controlled Coupling of a Single Nitrogen-Vacancy Center to a Silver Nanowire," *Phys. Rev. Lett.*, vol. 106, no. 9, Feb. 2011.

[214] S. Schietinger, M. Barth, T. Aichele, and O. Benson, "Plasmon-Enhanced Single Photon Emission from a Nanoassembled Metal−Diamond Hybrid Structure at Room Temperature," *Nano Lett.*, vol. 9, no. 4, pp. 1694–1698, Apr. 2009.

[215] M. Barth, S. Schietinger, T. Schröder, T. Aichele, and O. Benson, "Controlled coupling of NV defect centers to plasmonic and photonic nanostructures," *J. Lumin.*, vol. 130, no. 9, pp. 1628–1634, Sep. 2010.

[216] M. Geiselmann, R. Marty, J. Renger, F. J. García de Abajo, and R. Quidant, "Deterministic Optical-Near-Field-Assisted Positioning of Nitrogen-Vacancy Centers," *Nano Lett.*, vol. 14, no. 3, pp. 1520–1525, Mar. 2014.

[217] E. Rittweger, D. Wildanger, and S. W. Hell, "Far-field fluorescence nanoscopy of diamond color centers by ground state depletion," *EPL Europhys. Lett.*, vol. 86, no. 1, p. 14001, Apr. 2009.

[218] G. Balasubramanian, A. Lazariev, S. R. Arumugam, and D. Duan, "Nitrogen-Vacancy color center in diamond—emerging nanoscale applications in bioimaging and biosensing," *Curr. Opin. Chem. Biol.*, vol. 20, pp. 69–77, Jun. 2014.

[219] M. W. Doherty, N. B. Manson, P. Delaney, F. Jelezko, J. Wrachtrup, and L. C. L. Hollenberg, "The nitrogen-vacancy colour centre in diamond," *Phys. Rep.*, vol. 528, no. 1, pp. 1–45, Jul. 2013.

[220] L. H. G. Tizei and M. Kociak, "Spectrally and spatially resolved cathodoluminescence of nanodiamonds: local variations of the NV $^0$ emission properties," *Nanotechnology*, vol. 23, no. 17, p. 175702, May 2012.

[221] H. Zhang, D. R. Glenn, R. Schalek, J. W. Lichtman, and R. L. Walsworth, "Efficiency of Cathodoluminescence Emission by Nitrogen-Vacancy Color Centers in Nanodiamonds," *Small*, vol. 13, no. 22, p. 1700543, Jun. 2017.

[222] W. Primak, "Refractive index of silicon," *Appl. Opt.*, vol. 10, no. 4, pp. 759–763, 1971.

[223] T. Bååk, “Silicon oxynitride; a material for GRIN optics,” *Appl. Opt.*, vol. 21, no. 6, pp. 1069–1072, 1982.

[224] “FDTD Solutions | Lumerical’s Nanophotonic FDTD Simulation Software.” [Online]. Available: https://www.lumerical.com/tcad-products/fdtd/. [Accessed: 12-Dec-2017].

[225] E. D. Palik, *Handbook of Optical Constants of Solids*. Academic Press, 1998.

[226] W. Liu *et al.*, “Fluorescent Nanodiamond–Gold Hybrid Particles for Multimodal Optical and Electron Microscopy Cellular Imaging,” *Nano Lett.*, vol. 16, no. 10, pp. 6236–6244, Oct. 2016.

[227] A. Gopinath, E. Miyazono, A. Faraon, and P. W. K. Rothemund, “Engineering and mapping nanocavity emission via precision placement of DNA origami,” *Nature*, vol. 535, no. 7612, pp. 401–405, Jul. 2016.

[228] A. Gopinath and P. W. K. Rothemund, “Optimized Assembly and Covalent Coupling of Single-Molecule DNA Origami Nanoarrays,” *ACS Nano*, vol. 8, no. 12, pp. 12030–12040, Dec. 2014.

[229] J. Hann *et al.*, “Selective immobilization of 6HB and Tablet DNA origami Templates on microstructured surfaces by DLC and CF-polymer contrasting suitable for microfluidic integration,” *Mater. Today Proc.*, vol. 4, no. 7, pp. 7114–7121, 2017.

# ACKNOWLEDGMENTS

This work would not be complete without the contribution and support of many people.

I wish to foremost thank an outstanding woman in my life that I want to make the most proud of me. To my mother Fatma who I always look forward to. Who taught me what life means, respect myself and the others. Mom as you dreamed since I was a child, one day I will become a doctor, this day is approaching to realize your wish. I know you are up there always with me, rest in peace Annem.

I would like to thank my supervisor Dr. Thorsten Schmidt for providing me an exciting and challenging PhD project, helping me to explore my limits, developing my scientific skills, allowing me to work independently and always having time for me to discuss and talk about non/scientific topics. The last four years were truly a great experience.

I would like to express my gratitude to my thesis advisory committee: Prof. Lukas Eng, Prof. Michael Mertig, Prof. Stefan Diez and Dr. Thorsten Schmidt for their guidance, support, and advice throughout my PhD study. All have been an invaluable asset. I once more would like to thank Prof. Michael Mertig for being my Doktorvater and always encouraging and motivating me.

I am truly grateful to Prof. Anatoly Zayats for kindly hosting my stay at King's College London. In particular, Dr. Cillian McPolin and Diane Roth for the great assistance with the experiments in King's. I would like to thank Dr. Tobias König for a fruitful collaboration on the theoretical aspects of this work. I am very grateful to Assist. Prof. Dr. Søren Raza and Dr. Friedrich Schwarz for being not only the excellent collaborators but also sharing precious insights and friendships. I am thankful to Prof. Mark Brongersma for taking his time to discuss my PhD project. I would like to thank people in the Fery group, especially Martin, Yannic, and Anja who I worked with. I thank Dr. Markus Löffler for the training of electron microscope. I was definitely lucky to work with all of these excellent researchers.

I am very grateful to Dr. Thorsten Schmidt, Dr. Jasmina Dikić, and Dr. Søren Raza for proofreading this thesis. I would also like to thank Richard Weichelt for the German

translation of the abstract. I thank to Kayla Friedman and Malcolm Morgan for providing this thesis template.

I would like to thank all the former and current Schmidt lab members, Diana, Simon, Shikhar, Bastian, Olga, Jingjing, Erik, Hafees, for creating a nice working environment, for fun lunch, coffee breaks, and cakes. Many thanks particularly to Katarina, Michael, Yavuz, and Nayan for standing by me when I had bad times. Special thanks to Anne, our secretary, for her generous help and support whenever I needed. I also would like to thank all the Mertig lab members, particularly Franzi, Matthias, Johanna, Andreas and Kathrine for sharing lab and any kind of help that they provided. I want to thank all the students who I supervised, especially DNAmic biomod team 2014, I learned a lot from all of you. I am grateful to the cfaed HR team, Matthias, Susann, Sandra, Anett and Patricia for their support and help.

I want to thank all my friends back in the home, Ali, Sevgi, Ibrahim, Bekir, Emrah, Tarık and Müşerref for believing in me and for their endless support. I thank my friends, Janna, Michelle and Stephanie my flat mates in London, Judith my former flat mate in Dresden, Franci, Matthias, Lisa my dance mates and Anna my dance teacher, Varsha and Ilke my classmates in my Master study. I am glad that I met you and had great times with all of you.

I am very much thankful to the Turkish gang in Dresden, who mentally supported me, shared the joys and sadness, and made me feel at home. Many thanks to Çağdaş, Zeliha, Can, Güneş, Aylin, Erdinç, Müge, Çiğdem, Edis, Zeynep, Türkan, Gözde, Nehir, Dilce, Ilke, and Onur. Teşekkür ederim gençler.

Finally, my biggest thanks go to my family who always cares about me, always believes in me, always there to fully supports me, always ready to gives me unconditionally, generously all the things that I need. To my father Süleyman, my second mother Ayşe, my sisters Yaşar, Meryem, Türkan, Umut, Derya and my brother Ozan, my nephews Deniz, Batuhan, Ufuk and Baran, and my lovely niece Buglen. In the end, I would like to thank Jingjing for her continuous support.

# ABOUT THE AUTHOR

## Personal information

**Fatih Nadi Gür**

Address: Förstereistr.10, 01099,
Dresden, Germany
E-mail address: fatihnadigur@gmail.com
Date of birth: 20 March 1987
Place of birth: Karaman, Turkey

## Education

| | |
|---|---|
| Since 01/2014 | PhD in Physical Chemistry<br>Thesis title: Plasmonic waveguides self-assembled on DNA origami templates: from synthesis to near-field characterizations<br>Supervisors: Prof. Michael Mertig and Dr. Thorsten-Lars Schmidt<br>Technische Universität Dresden, Germany |
| 11/2016 -01/2017 | Research stay in King's College London<br>Supervisor: Prof. Anatoly Zayats |
| 04/2013 -11/2013 | Research assistant in BCUBE Center for Molecular Bioengineering<br>Supervisor: Prof. Yixing Zhang |
| 2010– 2012 | Master of Science in Nanoscience and Nanotechnology specialization in Biophysics, joint degree Erasmus Mundus master program.<br>Thesis title: Impedimetric detection of microorganisms using platinum nanowires<br>Supervisor: Prof. Gianaurelio Cuniberti<br>Katholieke Universiteit Leuven, Belgium and Technische Universität Dresden, Germany |
| 2005-2010 | Bachelor of Science in Physics<br>Izmir Institute of Technology, Turkey |

## Conferences & workshops

| | |
|---|---|
| 12/2017 | DNA nanotechnology Mitteldeutschland workshop, Leipzig (talk) |
| 06/2017 | Future Trends in DNA-based Nanotechnology workshop, Dresden |
| 07/2016 | Plasmonics & Nanophotonics, Gordon Research Conference, Sunday River Newry, ME, the USA (poster) |
| 12/2015 | DNA nanotechnology meets plasmonics conference, Bad Honnef (poster) |
| 05/2015 | Molecular Plasmonics conference, Jena, (poster) |
| 05/2015 | DNA nanotechnology Mitteldeutschland workshop, Jena (talk) |
| 09/2014 | Pico Quant 20th international workshop, Berlin |
| 09/2014 | DNA nanotechnology Mitteldeutschland workshop, Dresden (talk) |
| 05/2014 | DNA-Based Nanotechnology: Digital Chemistry workshop, Dresden (poster) |
| 02/2014 | DNA nanotechnology Mitteldeutschland workshop, Leipzig (talk) |

## Awards

| | |
|---|---|
| 12/2016 | TUD graduate academy travel award for FNANO17 conference (declined due to the health issues) |
| 10/2016 | cfaed inspire grant for research stay in King's College London |
| 12/2015 | The best student poster prize in "DNA nanotechnology meets plasmonics" conference, Bad Honnef |
| 11/2014 | Dresden DNAmic – TU Dresden, BIOMOD competition 2014 in Harvard University, 2nd place and best wiki award (http://biomod.net), I was a PhD mentor for the team |
| 2010-2012 | Awarded Erasmus Mundus full scholarship for studying master of nanoscience and nanotechnology by the European commission |
| 2010 | Honor and top 3rd graduate student in Physics department at Izmir Institute of Technology, Turkey |

## Languages

| | |
|---|---|
| Turkish | Mother language |
| English | Proficient |
| German | Basic |

# ERKLÄRUNG

Hiermit versichere ich, dass ich die vorliegende Arbeit ohne unzulässige Hilfe Dritter und ohne Benutzung anderer als der angegebenen Hilfsmittel angefertigt habe; die aus fremden Quellen direkt oder indirekt übernommenen Gedanken sind als solche kenntlich gemacht. Die Arbeit wurde bisher weder im Inland noch im Ausland in gleicher oder ähnlicher Form einer anderen Prüfungsbehörde vorgelegt.

Diese Dissertation wurde im Zeitraum vom Januar 2014 bis Dezember 2017 unter der Betreuung von Prof. Michael Mertig (Physikalische Chemie, TU Dresden) und Dr. Thorsten Lars Schmidt (cfaed, TU Dresden) im cfaed - Center for Advancing Electronics Dresden, Technische Universität Dresden.

Es haben keine früheren erfolglosen Promotionsverfahren stattgefunden.

Hiermit erkenne ich die Promotionsordnung der Fakultät Mathematik und Naturwissenschaften der Technischen Universität Dresden in der Fassung vom 23.02.2011 inklusive der Änderungen vom 15.06.2011 und 18.06.2014 an.

Fatih Nadi Gür

Dresden, 15. Dezember 2017